TAMPEREEN TEKNILLINEN YLIOPISTO
TAMPERE UNIVERSITY OF TECHNOLOGY

Juuso Terva

The effect of compression and sliding movement on the wear resistance of steels and crushing work in mineral crushing

Julkaisu 1458 • Publication 1458

Tampere 2017

Tampereen teknillinen yliopisto. Julkaisu 1458
Tampere University of Technology. Publication 1458

Juuso Terva

The effect of compression and sliding movement on the wear resistance of steels and crushing work in mineral crushing

Thesis for the degree of Doctor of Science in Technology to be presented with due permission for public examination and criticism in Konetalo Building, Auditorium K1702, at Tampere University of Technology, on the 24th of February 2017, at 12 noon.

Tampereen teknillinen yliopisto - Tampere University of Technology
Tampere 2017

Doctoral candidate: Juuso Terva
Laboratory of Materials Science
Tampere University of Technology, Finland

Supervisor: Professor Veli-Tapani Kuokkala
Laboratory of Materials Science
Tampere University of Technology, Finland

Pre-examiners: Professor Staffan Jacobson
Department of Engineering Sciences, Applied Materials Science
Uppsala University, Sweden

Associate Professor Esa Vuorinen
Department of Engineering Sciences and Mathematics
Luleå University of Technology, Sweden

Opponents: Professor Staffan Jacobson
Department of Engineering Sciences, Applied Materials Science
Uppsala University, Sweden

Docent Jari Liimatainen
Picodeon Oy Ltd., Finland

Suomen Yliopistopaino Oy
Juvenes Print TTY
Tampere 2017

ISBN 978-952-15-3910-7 (printed)
ISBN 978-952-15-3917-6 (PDF)
ISSN 1459-2045

ABSTRACT

The purpose of crushing equipment is to reduce the size of aggregates. Minerals have good compressive strength, but they are relatively weak in tension. Most of the equipment crushes the rock by compression, which produces also tensile stresses high enough to fracture the rock. A single-toggle jaw crusher utilizes two plates, one stationary and another moved by an eccentric axle, to crush the aggregate between the jaw plates. The interaction of the aggregate with the jaw plates causes high contact forces, which are high enough to cause plastic deformation in the jaw plates. Some of the contacts remove material from the jaw plates. Wear changes the shape of the jaw plates, which affects the crushing capacity of the jaw crusher and eventually leads to the replacement of the jaw plates.

The movement pattern of the jaws is an important factor in the efficiency of crushing. Compressive motion is needed to crush the rock, whereas lateral motion is desired as it helps the flow of the aggregate through the crusher and increases the capacity. In a jaw crusher, a flywheel is used to store kinetic energy to turn the eccentric axle, which applies the motion to the jaw. The amount of work consumed in each compression cycle depends on the movement pattern of the jaw as well as on the mechanical properties of the crushed mineral. Part of the work is also consumed by the friction of the crushing mechanism, by the plastic deformation of the crushing contacts, and by the crushing of the aggregates.

This thesis concentrates on studying how the movement pattern of the jaw crusher affects the wear of the jaw plates and the work consumed in the crushing and wear processes. A new test equipment, the dual pivoted jaw crusher (DPJC), was designed and manufactured to make the study possible. The DPJC is a laboratory sized jaw crusher, which allows changes in the relation between the compressive and lateral movements of the jaw. It also has a modular jaw structure, which enables changing of the geometry of the crushing cavity. The thesis concentrates on determining how the parameters of the crushing equipment affect the wear and work done in the tests with high manganese and tool steel specimens.

The results of the tests show that there is a linear relationship between the wear of the specimens and the work done in the test. Also, when the movement pattern of the jaws is changed, the increase of the lateral motion increases the wear of the specimens and the total work done in the test. The DPJC was shown to be a versatile tool for wear research, causing extensive deformation and wear in the jaw plate materials, and having the ability to work harden also austenitic manganese steels. Carbide reinforced tool steels are known for their good wear resistance under compression, but with increasing lateral motion of the jaw plates they were observed to be susceptible to shear localization, which can decrease their wear performance. In addition to wear testing, the DPJC equipment can be used for comminution testing of minerals.

PREFACE

This work was carried out at Tampere Wear Center (TWC) in the Laboratory of Materials Science of Tampere University of Technology (TUT). Part of the work was also carried out at Mining Materials Wear and Corrosion Consortium at the National Research Council, Vancouver, Canada, between September and December 2010.

The experimental research of this work was conducted as a part of the Demanding applications (DEMAPP) research program of the Finnish Metals and Engineering Competence Cluster (FIMECC). The thesis was completed in the Breakthrough Steels and Applications (BSA) research program of the Digital, Internet, Materials & Engineering Co-Creation (DIMECC). These programs were funded by the Finnish Funding Agency for Technology and Innovations (TEKES), and the participating companies and research institutions. Materials for the testing were provided by Metso Minerals Oy, SSAB Europe Oy (formerly Ruukki Metals Oy), and National Research Council, Vancouver, Canada.

My work was supervised by Professor Veli-Tapani Kuokkala, to whom I wish to express my gratitude for the open-minded support, easily approachable attitude, as well as for the enthusiasm to approach the various questions I presented. The excellent working spirit of the Laboratory of Materials Science (formerly Department of Materials Science) has been very helpful to provide a good foundation for the research work, for which I am grateful to all the former and present staff members. I give special thanks to Lic Tech Kati Valtonen, who initiated me to the working habits of the laboratory, and to Dr. Matti Isakov, M.Sc. Ilari Jönkkäri, M.Sc. Jari Kokkonen, and M.Sc. Kauko Östman for the multidimensional discussions during the lunch and coffee breaks. I also wish to thank Dr. Matti Lindroos, Dr. Vilma Ratia, M.Sc. Vuokko Heino and M.Sc. Niko Ojala for the team spirit of TWC. Special thanks goes also to Dr. Juha-Pekka Nikkanen for his dedication to lyrics, and Ari Varttila for constructing the DPJC equipment.

I want to thank Dr. Jiaren Jiang and the personnel at the National Research Council, Vancouver, Canada, for giving me a chance to gain experience in the jaw crusher testing. I also want to thank Dr. Marke Kallio, Lich Tech. Pekka Siitonen, and M.Sc. Keijo Viilo from Metso Minerals Oy for their support and comments.

Last, but not least, I want to thank my family, Outi, Veera and Valtteri for their patience for my late working hours, as well as my parents Tarja and Tapani, and my siblings Johanna and Jyrki, for their invaluable support and encouragement.

Tampere, 26.1 2017

Juuso Terva

AUTHOR'S CONTRIBUTION

Juuso Terva was the principal researcher in this work, who planned and performed most of the experiments and characterizations, analyzed the test results and prepared the manuscript. The ASTM G81-97a standard wear tests were conducted at the National Research Council, Vancouver, Canada, by Dr. Jiaren Jiang and Mr. Kidus Tufa.

LIST OF SYMBOLS AND ABBREVIATIONS

Greek symbols

α	Swing angle of the dual pivoted jaw crusher
α_a	Attack angle
α_c	Critical attack angle
α_s	Slope of the asperity
α_{sa}	Semi-angle of the wedge
β	Tilt angle of the jaw frame axles
β_c	Fraction of contacts with attack angles above a critical value
β_d	Factor describing the decay of deformation with increasing depth
Δd	Displacement of the jaws
Δl	Linear wear
ΔS	Friction path
ΔW	Sum wear
ΔY	Displacement in the Y direction of the force sensors
ΔY_2	Displacement in the Y direction parallel to the Jaw2 specimen surface
ΔY_3	Actual sliding displacement parallel to the Jaw2 specimen surface
ΔZ	Displacement in the Z direction of the force sensors
ΔZ_2	Displacement in the Z direction normal to the Jaw2 specimen surface
ΔZ_3	Actual compressive displacement normal to the Jaw2 specimen surface
ϵ_t	True fracture strain
ε	Relative wear resistance
ε_0	Relative wear resistance of the material in annealed condition
ε_i	Relative wear resistance of the test material
ε_{ph}	Wear resistance of a phase
ε_T	Total wear resistance of a multiphase material
θ	Opening angle of the abrasive cone
θ_i	Apex angle of the peaks in a profile
$\mu, \mu_1, \mu_2 ...$	Friction coefficient
μ_0	Friction coefficient at zero wear
μ_{adh}	Adhesive friction coefficient
μ_{def}	Friction coefficient of deformation
μ_f	Interfacial coefficient of friction between soft material and hard asperity
μ_g	Friction coefficient in grooving wear
ρ	Density
ρ(y)	Density function
σ	Stress
σ_{st}	Standard deviation
σ_y	Yield strength
σ_f	Strength of the interfacial film

τ	Shear stress
τ_f	Shear flow stress
τ_s	Shear strength
τ_y	Shear yield strength
τ_k	Average shear flow stress
Φ_1	Geometrical factor describing the shape of the abrasive particles
φ_{lim}	Capability of deformation of a material before cracking occurs
φ_s	Effective deformation on the wearing surface
Ψ	Factor of the change of volume loss caused by reinforcing particles

Latin symbols

A, A_1, A_2, ...	True area of contact
a	Radius of the contact circle
A_{ap}	Apparent area of contact
A_c	Parameter related to the flow stress
A_d	Definition area
A_j	Area of junction
A_n	Area of contact normal to the specimen surface
A_p	Area of contact perpendicular to the specimen surface
A_V	Cross-sectional area of a groove
A_{w1}, A_{w2}	Cross-sections of the side wedges of a groove
C	Temperature coefficient of flow stress
C_{min}	Minimum temperature coefficient of flow stress
$C_{wt.}$	Carbon content in weight percent
c, c_2,c_3	Coefficient
D	Distance between the axles
d_{min}	Minimum distance between the jaws (gap)
d_{max}	Maximum distance between the jaws (gap)
d_Z...	Position of the jaw frames in the compressive direction
d_Y...	Position of the jaw frames in the sliding direction
E	Modulus of elasticity
e	Allowable error
e_c	Critical strain for the localization of deformation
e_s^*	Energy density transferred to a wearing body
E	Energy
E_0	Minimum energy needed for comminution
F_{80}	Feed size with 80 % passing the sieve
F_τ	Shear force
F_{adh}	Friction force of adhesion
F_c	Total contact force calculated from the force vector components
F_N	Normal force
F_T	Tangential force
F_z	Compressive force in the Z direction of the sensors
F_{z2}	Compressive force in the direction normal to the Jaw2 specimen surface
F_y	Tangential force in the Y direction of the sensors
F_{y2}	Tangential force in the direction parallel to the Jaw2 specimen surface

f	Fraction of a groove ploughed to either side
f_{ab}	Ratio of the volumes removed by cutting and ploughing
H	Hardness
H_0	Hardness of the material in annealed condition
H_{def}	Hardness of deformed surface
H_{eq}	Equivalent hardness of a multiphase material
H_{hp}	Hardness of the hard phase
H_i	Hardness of the test material
H_m	Hardness of the matrix
H_r	Hardness of the reference material
H_U	Maximum hardness of the test
h	Depth of penetration
h_s	Height of the ridges of previous grooves
K	Abrasive wear coefficient
k_{ad}	Adhesive wear coefficient
K_c	Comminution work coefficient
K_{CA}	Factor of crystal anisotropy
K_s	Parameter scaling the effect of shear pressure when no slip occurs
L	Sliding distance
L_p	Length of profile
l	Overlap parameter of successive scratches
m	Mass of the crushed material
N	Number of traverses
n	Strain hardening exponent
n_e	Order of the comminution process
n_o	Number of observations or tests
n_p	Number of spikes analyzed
n_s	Amount of required samples
p	Surface pressure
P_{80}	Product size with 80 % passing the sieve
p_0	Yield pressure under normal force
p_1	Reduced yield pressure under normal force
p_{normal}	Normal pressure
p_{shear}	Shear pressure
R	Tip radius
R_a	Average roughness of the surface profile
R_{ku}	Kurtosis of the surface profile
R_m	Volume wear of the reference specimen in the moving jaw
R_q	Root mean square profile roughness parameter
R_s	Volume wear of the reference specimen in the stationary jaw
R_{sk}	Skewness of the surface profile
r	Radius of a sphere
r_{def}	Proportion of total work going to plastic deformation
RR	Reduction ratio

S	Flow stress
S_0	Constant related to flow stress
S_a	Arithmetic mean height of the scale limited surface
S_{ar}	Rock surface area change
S_k	Kurtosis of the scale limited surface
S_{sk}	Skewness of the scale limited surface
S_q	Root mean square height of the scale limited surface
T	Temperature
T_c	Average temperature of a chip
T_m	Melting temperature of the material
t	Time
UTS	Ultimate tensile strength
V	Removed volume
v	Velocity
v_{ph}	Volume fraction of the phases
v_m	Volume fraction of the matrix
v_{hp}	Volume fraction of the hard phase
V_0'	Coefficient of variation
W	Wear
W_K	Specific wear rate
W_V	Wear as volume loss
W_c	Wear by compression
$W_{l/s}$	Linear wear intensity
W_m	Wear as mass loss
W_{mat}	Wear of the test material
W_{ref}	Wear of the reference material
W_R	Wear ratio
WR_{factor}	Relation of wear resistances in the tests with $\beta = 0°$ and $\beta = 90°$ tilts
W_{RS}	Sum wear ratio
W_s	Wear by sliding
W_{work}	Work in sliding
W_{wr}	Average wear rate
x	Position coordinate from the origin
x_f	Size of the comminuting feed
x_{fin}	Fineness of the product
X_m	Volume wear of the test specimen in the moving jaw
x_p	Size of the comminution product
X_s	Volume wear of the test specimen in the stationary jaw
y	Position coordinate from the origin
Y	Y direction of the force sensor coordinates
Y_2	Y direction parallel to the Jaw2 specimen surface
Z	Z direction of the force sensor coordinates
z	Height of the surface or profile
Z_2	Z direction normal to the Jaw2 specimen surface

AC	Alternating current
Al_2O_3	Alumina
AISI	American Iron and Steel Institute
ASTM	American Society for Testing and Materials
B	Boron
$Bond_{wi}$	Bond work index
BSE	Backscatter Electron
L. A. index	Los Angeles index
C	Carbon
Cr	Chromium
DPJC	Dual Pivoted Jaw Crusher
EDS	Energy Dispersive Spectroscopy
EBSD	Electron Backscatter Diffraction
FEG-SEM	Field Emission Gun Scanning Electron Microscope
FFT	Fast Fourier Transform
G81	ASTM G81-97 gouging abrasion test
HB	Brinell hardness
HIP	Hot Isostatic Pressing
HV, HV1, HV5	Vickers hardness with 1 kg load or 5 kg load
Jaw1	Left hand side jaw in the test configuration
Jaw2	Right hand side jaw in the test configuration
M_7C_3	Metallic carbide
MMC	Metal Matrix Composite
Mn	Manganese
Mo	Molybdenum
Nb	Niobium
Ni	Nickel
OP-S	Colloidal Silica Polishing Suspension
P	Phosphorus
P_{cr}	Product size in the DPJC tests with 3.15 mm - 6 mm min-max gap
P80 .. P4000	Grit size of the grinding paper
RWAT	Rubber Wheel Abrasion Test
rpm	Revolutions per minute
S	Sulphur
SEM	Scanning Electron Microscope
SF	Spray Forming
Si	Silicon
SiC	Silicon Carbide
SPQ	Quadratic Spike Parameter
TEM	Transmission Electron Microscope
UCS	Ultimate Compressive Strength
V	Vanadium
VC	Vanadium Carbide
W	Tungsten
WC	Tungsten Carbide
TUT	Tampere University of Technology
NRC	National Reseach Council Canada
TWC	Tampere Wear Center

Contents

ABSTRACT i

PREFACE iii

AUTHOR'S CONTRIBUTION v

LIST OF SYMBOLS AND ABBREVIATIONS vii

1 Introduction 1
1.1 Aim of the work 1

2 Theory 3
2.1 Quarrying 3
2.1.1 Comminution work . . . 3
2.2 Jaw crushers 5
2.2.1 Description of the jaw movement in a common single toggle jaw crusher 7
2.2.2 Wear tests with a jaw crusher . . . 8
2.3 Tribology and contact forces 10
2.3.1 Surface profile . . . 10
2.3.2 Surface texturing . . . 12
2.3.3 Contact between surfaces . . . 12
2.3.4 Friction during sliding . . . 13
2.4 Wear of metals 14
2.4.1 Abrasive and adhesive wear . . . 14
2.4.2 Classification by the wear environment . . . 15
2.4.3 Contact geometry: ploughing, prow formation, or cutting . . . 17
2.4.4 Surface deformation and fatigue . . . 19
2.4.5 Material properties . . . 20
2.4.6 Abrasive particle properties . . . 25
2.4.7 Friction in abrasion . . . 27
2.4.8 Abrasion work . . . 28
2.4.9 Comparison of the high stress and gouging abrasion test . . . 29

3 Design of the dual pivoted jaw crusher 31
3.1 Operational systems 31
3.1.1 Jaw frame assembly . . . 32
3.1.2 Feeding system . . . 34
3.1.3 Collection system . . . 34
3.1.4 Electric motor with gearbox and flywheel . . . 35
3.1.5 Measurement system . . . 35
3.2 Movement of the dual pivoted jaw crusher 35
3.2.1 Movement of the Jaw1 and Jaw2 specimen surfaces . . . 36

4 Materials and methods 40

4.1 Materials 40
4.1.1 Microstructure of the tool steels . . . 40
4.1.2 Abrasives and their properties . . . 42
4.2 Test methods 43
4.2.1 ASTM G 81-97a Jaw Crusher test . . . 44
4.2.2 Tests with the dual pivoted jaw crusher . . . 46
4.3 Wear surface and material characterization 51
4.3.1 Measurement of wear . . . 51
4.3.2 Microscopy . . . 51
4.3.3 Hardness testing . . . 51
4.3.4 Specimen preparation . . . 52
4.3.5 Profilometry . . . 53
4.3.6 Rock size analysis . . . 53

5 Results 54
5.1 Jaw crusher tests 54
5.1.1 Tests on S355 specimens . . . 55
5.1.2 Tests on manganese steels . . . 58
5.1.3 Tests on tool steel specimens . . . 66
5.2 Wear surface analysis 73
5.2.1 S355 steel . . . 73
5.2.2 Manganese steels . . . 77
5.2.3 Tool steels . . . 82
5.3 Reliability of data 99

6 Discussion 103
6.1 Comparison of jaw crusher wear test methods 103
6.1.1 The size and mechanical properties of the feed in the jaw crusher wear test . . . 103
6.1.2 Comparison of the wear ratio with different jaw crusher test methods 104
6.1.3 Summary of the discussion on wear testing . . . 107
6.2 Relationship between wear, comminution and crushing work 107
6.2.1 Relationship between wear and work . . . 109
6.2.2 Effect of jaw geometry and rock properties on the relationship between wear, comminution, and work . . . 117
6.2.3 Summary of the discussion on the relationship between wear and work 118

7 Conclusions 119

Bibliography 122

1 Introduction

From the start of civilization people have had the need to break rocks either to make a defined shaped product or tool, or for being able to process the minerals within the rock. The techniques to break a rock have developed through the time from chisels and hammers or breaking with fire, ice or water, to explosive mining and heavy duty equipment capable of drilling or crushing the rock in large quantities. Major improvements were made in the 19th century due to the steam engine, electricity, and the technological advances in manufacturing. Most of the modern crushing equipment, such as the jaw crusher, originates from the 19th century or from the beginning of the 20th century. The concept of optimizing the crushing process has since been under development. In addition to the crushing efficiency, the wear of the equipment has been under vast research.
The relatively hard and brittle natural rocks need high compressive or impact forces before fracturing, causing a very harsh wear environment for the counterfaces that often contain phases with lower hardness than the mineral phases of the rocks. Austenitic high manganese steels, also known as Hadfield steels, have been the dominating material for most of the crushing applications due to their toughness and high capability to work harden. These properties give an excellent wear resistance against impacts and abrasion. Also other materials find use in the crushing applications: rubber is used in sieves and conveyor belts, and carbide reinforced steels and hard metals of high hardness in parts where their lower ductility and lower impact resistance are not a problem.
The development of new wear resistant materials suitable for a specific application needs a testing method that is reliable, repeatable and can closely replicate the wear environment of the crushing application.

1.1 Aim of the work

The aim of this work was to increase understanding of the effects of sliding and compressive movements of the jaws on the consumed energy and wear of the jaw plates in a jaw crusher. A new jaw crusher design was constructed for this purpose, as the previous test methods did not permit such tests without considerable changes in the test equipment. The new jaw crusher was designed for separate changing of the individual variables in the jaw crusher environment, thus allowing for better understanding of the rock crushing process and the wear of the materials in the crushing conditions.
A jaw crusher is designed to crush the rocks into smaller sizes. The main outcomes of the jaw crusher in operation are the comminution of the rock, the wear of the jaw plates and the amount of work needed to operate the jaw crusher. The basic assumption of this thesis was that although the outcomes of the crushing operation are a result of several single events, the work done in the test could be separated into two different classes:

- Work done to comminute the rock.
- Work done to move the rock by sliding or rolling against the jaw plates, resulting in deformation and wear of the jaw plates.

The above hypothesis was made based on the brittle nature of rock fracture. Therefore, the amount of energy needed for the size reduction of the rock from one size fraction to another

should be fairly constant with the same mineral. The increase in the sliding movement should therefore mainly affect the deformation and the wear of the jaw plates. The research questions of the thesis were formulated based on this assumption:

1. Are the wear of the jaw plates, the comminution of the rock, and the crushing work related?
2. Do the jaw geometry and the rock properties affect the relationship between wear, comminution, and work?
3. Does the increase in the sliding movement of the rock particles on the jaw plates affect the relative wear resistance of the selected materials?

Three test series were prepared to answer each of the research questions. The first test series concentrated on the relation of wear and work, and the statistical reliability of the test method. The second test series was used to study the effect of jaw angles and the size of the rock particles on the relation of wear and work. The third test series compared the wear and work relation of several carbide reinforced steels. The effect of the sliding movement on the wear of the test materials was examined also by investigating the wear surface deformation and wear debris of the materials. The materials of the third test series were also tested with the existing standard test ASTM G81-97 [1] as a comparative study between the test methods. The jaw crusher test results were also compared to the results of scratch tests and crushing pin-on disk tests.

The thesis brings forth the following scientific contributions:

- A new laboratory size test equipment was designed to examine high stress and gouging abrasion. The main benefits of the test equipment are the simple working mechanism to apply crushing forces, the ability to monitor the experiment visually or by the use of sensors, and the ease to separately adjust the crushing geometry and the movement of the jaws.
- The relation between comminution and work was found to be constant, while the relation between wear and work was found to follow a linear relationship with increasing sliding movement of the jaws. As the work is separable, the amount of work can be used more reliably to compare the comminution and wear of different materials.
- The relation between wear and the hardness of the wear surface of materials has been previously determined to be linear with tests using smaller rock or grinding paper as abrasive [2]. The tests with the new jaw crusher showed that this relation continues to be linear also in the crushing environment with larger rock size.
- The increasing speed of the sliding movement leads to increasingly dynamic wear behavior in the jaw plates in the jaw crushing environment. The strain rate of cutting abrasion was found to be in the limit of localized shear banding due to adiabatic heating. The propability of chip formation by adiabatic shear banding was found to be lower with softer materials due to the increased cutting depth.

In addition to the scientific contribution, the new jaw crusher can benefit also the industry. The ability to measure wear with a set sliding movement of the jaw can be useful for the modeling and development of the jaw and cone crusher equipment. Moreover, the system is able to determine the crushing and abrasion properties of the minerals that are important process parameters in mineral processing.

2 Theory

This chapter examines the theory related to the topic of the thesis. The first section describes the functioning of the jaw crusher used in quarries, the operating principle of the jaw crusher, and an overview how the jaw crusher wear testing has been developing. The second section gives an overview of the surface profiling and what happens in the contact between surfaces. The third section defines how the contacts cause wear, concentrating on the wear of metallic materials, and which properties affect the outcome of the wear processes.

2.1 Quarrying

Quarrying contains several activities to obtain the desired product. The size reduction of the rock material is an important part of the process, where the end product size requirement can be from stone or gravel sized aggregates to very fine powders. For example, mineral processing requires fine product size in order to separate ore from the rock. Drilling and blasting are used to break the bedrock to boulders and smaller rocks, which are hauled to a mobile or stationary plant to be crushed [3]. The process of comminution involves several stages of crushing and screening. The size of the rock particles, which enter the first primary crushing stage can be up to 1.5 meters in diameter [4]. The reduction ratio (RR) of the crushing equipment defines the size reduction of the feed to the crushed product as:

$$RR = \frac{F_{80}}{P_{80}} \tag{2.1}$$

where F_{80} and P_{80} are the sieve sizes that 80 % of the feed and the product size passes, respectively [4]. The RR of the primary crushing stage is typically 3:1 [3]. The reduced size of the product after the primary crusher allows transportation on a conveyor belt. The selection of the crusher for primary crushing depends on the process, but the most used ones are larger jaw crushers for smaller capacity plants, primary gyratory crushers for higher capacity when quarry capacity is over 1000 tonnes/hour [5], and impact crushers when the materials are easily crushable [3]. After the primary crushing stage, the primary crusher product is screened from oversized rocks and fed to the secondary crushing stage. The purpose of the secondary stage is to produce coarse sized products, such as aggregates. Cone crushers are the most used equipment for the secondary stage due to their high capacity and low operating costs. Ball mills or rod mills are also used as secondary stage impact crushers [4]. Additionally, tertiary and quaternary stages can be used for the fine crushing and to determine the quality of the final product, if required. The reduction process can be either an open circuit or a closed circuit [6]. In the open circuit all the products of the crushing stage are transported to the next stage. In the closed circuit, the screeners return the oversized product to be crushed again in the same stage, and the crusher can be operated with a wider setting, allowing higher capacity.

2.1.1 Comminution work

The comminution process requires vast amount of energy, where the energy efficiency of the crushing is about 1 % - 2 % [7]. For example in South Africa the energy consumed by the mining sector is 15 % of the total electricity consumption of the country [8]. Therefore,

the energy consumption of comminution has been under vast research, beginning from the research of Rittinger (1867), Kick (1885), and Walker (1937) [9]. Most of the research has been concentrating on the grinding phase of producing fine particles. Several comminution test methods have been developed, but there is still need to develop a more convenient test procedure [10]. Equations 2.2 and 2.3 show two approaches to determine how size reduction is related to energy consumption [9]. Equation 2.2 from Rittinger is based on the energy of size reduction being proportional to the generation of new surface area, which is inversely proportional to the size of the particles. Kick, in turn, proposed Equation 2.3, where the relative size reduction requires similar energy independent of the sizes of the particles [9].

$$E = K_c(\frac{1}{x_p} - \frac{1}{x_f}) \tag{2.2}$$

$$E = K_c ln(\frac{x_f}{x_p}) \tag{2.3}$$

where E is the specific energy, K_c is the comminution work coefficient, x_f the size of the feed, and x_p the size of the product. Bond [11] used an impeller tumbler and a ball mill to obtain the work index w_i values of minerals in Equation 2.4

$$W_{work} = w_i(\frac{10}{\sqrt{P_{80}}} - \frac{10}{\sqrt{F_{80}}}) \tag{2.4}$$

where W_{work} is the amount of work in the test. A more general form of comminution energy was postulated by Walker as

$$dE = -c(\frac{dx_{fin}}{{x_{fin}}^{n_e}}) = -c(\frac{dx_{fin}}{{x_{fin}}^{f(x_{fin})}}) \tag{2.5}$$

where dE is the net energy required per unit weight in a comminution process, n_e is an order of the process, x_{fin} the factor of product fineness, and c is the material and unit related constant [9]. Replacing the n_e with values 2, 1 and 1.5, and integrating the equation leads to the theories of Rittinger, Kick and Bond. Hukki [9] also commented that the exponent n_e in Equation 2.5 was not constant but rather a function of the fineness of the product, and stated that the equations of Rittinger, Kick and Bond could be applicable for different particle size ranges. Equation 2.3 from Kick was applicable to larger particles, as in the crushing process. Equation 2.2 from Rittinger fitted better for the grinding process, whereas the Bond's Equation 2.4 was unifying the two older suggestions and was suitable especially for ball milling [9].

Hukki [9] classified the reduction steps and presented an example for the energy consumption of each step, as shown in Table 2.1 In all these steps the reduction ratio RR is 10:1.

The required work for crushing depends on the compressive and tensile strength of the mineral [12]. Minerals in general have good compressive strength and poor tensile strength. The elastic modulus of the minerals, e.g., ∼70 GPa for quartz, is also much lower than the 210 GPa of steels, which causes more elastic dimensional changes in minerals compared to the steel surfaces. The difference in the elastic properties of the contact between steel and quartz can cause crack propagation in the unloading phase of the minerals even when the loading phase shows no crack formation [13, 14]. The crack formation from the previous stages can lower the required crushing work, e.g., efficient blasting can decrease the energy consumption of the primary and secondary crushing stages [15].

The size of the feed also affects the energy consumption of the crushing process, where the fracture of larger particles requires less energy than finer particle breakage [16,17]. Workman and Eloranta [18] measured the energy consumption of several crushing stages, which are

Table 2.1: *Reduction steps and the energy consumption of each step [9]. The RR value of 2:1 is presented to ease the comparison to other energy consumption values presented in this thesis, and is obtained from the RR 10:1 values.*

Reduction step	Size range	Energy consumption, RR 10:1 kWh/t	E, RR 2:1 kJ/kg
Explosive shattering	Infinite - ∼1 m	Unknown	Unknown
Primary crushing	∼1 m - ∼100 mm	0.35	0.252
Secondary crushing	∼100 mm - ∼10 mm	0.6	0.432
Coarse Grinding	∼10 mm - ∼1 mm	1.6	1.152
Fine Grinding	∼1 mm - ∼100 μm	10	7.2

listed in Table 2.2. The grinding process consumes around 95 % of the total energy of the comminution process. However, the size reduction ratio RR was also the largest in the grinding process. When primary, secondary and grinding stage energy consumptions are compared by normalizing the size reduction ratio RR to 2:1, the secondary crushing stage stands out by requiring about twice the work of the other two stages. This comparison makes the secondary stage the least efficient crushing stage, which is controversial with the theory of increasing energy needed for crushing finer particles.

Table 2.2: *Calculated energy and expenditure of crushing stages according to pile size distribution [18].*

	Blasting	Primary crusher	Secondary crusher	Grinding	Total
Feed size (mm)		400	102	19.1	
Product size (mm)	400	102	19.1	0.053	
Performed work (kWh/ton)	0.24	0.23	0.61	19.35	20.43
Energy expenditure (USD/ton)	0.087	0.016	0.043	1.35	1.50
Feed / Product size (mm/mm)		3.92	5.34	360.4	
Size reduction work (RR 2:1) (kJ/kg)		0.432	0.792	0.396	

2.2 Jaw crushers

The first jaw crusher was patented by W.E. Blake in 1858 [19]. The Blake type jaw crusher had a fixed jaw and a moving jaw, which was pivoted from the top or feed end of the jaw [4]. The swing of the jaw, or throw, was produced by a rotating flywheel on an eccentric shaft. A pitman and a single or a double toggle mechanism connect the eccentric shaft to the moving jaw. Figure 2.1 a) shows the functional diagram of the Blake double toggle crusher. Other types of crushers are the Dodge type crushers, where the swing jaw pivot point is at the bottom or release end of the jaw, and a universal crusher, where the swing jaw pivot point is at the center point of the jaw [4]. The throw of the swing is different in each of the configurations. The Blake crusher has the largest motion of the jaw close to the release end, causing efficient crushing of fines. The ability to crush larger rocks is limited by the

smaller jaw motion near the pivot point. In the Dodge type crushers, the release end has smaller movement and the larger swing is at the feed end of the crusher. This causes efficient crushing of larger rocks, but the crusher is easier to choke as the fixed setting of the release end lowers the crushing efficiency. The Dodge type crusher is only suitable for laboratory testing to acquire close sized product. The central pivoted universal crusher has variable feed and release ends [4].

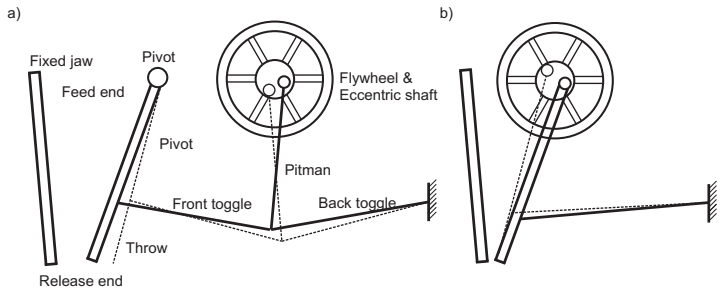

Figure 2.1: *Schematics of a) double toggle Blake jaw crusher b) single toggle crusher where the eccentric shaft is connected directly to the swing jaw.*

Figure 2.1 b) illustrates the single toggle jaw crusher, where the moving jaw is directly connected to an eccentric shaft. The movement of the eccentric shaft is transferred to the jaw, resulting in an elliptical jaw motion that assists the rock movement through the crushing chamber [4]. The faster the rock can pass through the crusher, the higher the capacity of the crusher and the higher the productivity of the crushing process. The gained higher capacity also increases the wear rate of the jaw plates, as the elliptical movement increases sliding of the rock against the plates. The single toggle jaw crusher is widely used in Europe due to its higher capacity, simpler design and lower costs [4]. Figure 2.2 shows the commercial single toggle jaw crusher from Metso Minerals.

The most important parameters in a jaw crusher are the width of the crusher, the angle between the jaws, the throw or maximum amplitude of the jaw, and the minimum gap between the jaws at the release end. The width of the crusher together with the angle between the jaws define how large rock particles can be fitted between the jaws. The rock is compressed and crushed at a certain vertical level of the jaw depending on the size of the rock. After the rock is crushed to smaller pieces, the particles fall to a lower level and are crushed again until they fit through the release end. The capacity of the jaw crusher can be improved by selecting a correct opening angle of the jaws, which depends on the mechanical and frictional properties of the rock. Typically the used jaw opening angles are less than 26°, as larger angles can cause slipping of the rock that reduces the capacity and increases wear [4]. The throw of the jaw, or the extent of the movement of the jaw, determines the compressive displacement or compaction of the rock. A large throw causes more crushing events in a cycle and decreases the possibility of chokage. The feed opening and the minimum gap between the jaws together with the throw determine the size limits of the feed and the product. The reduction ratio of the jaw crusher can vary from 4:1 up to 9:1 [6].

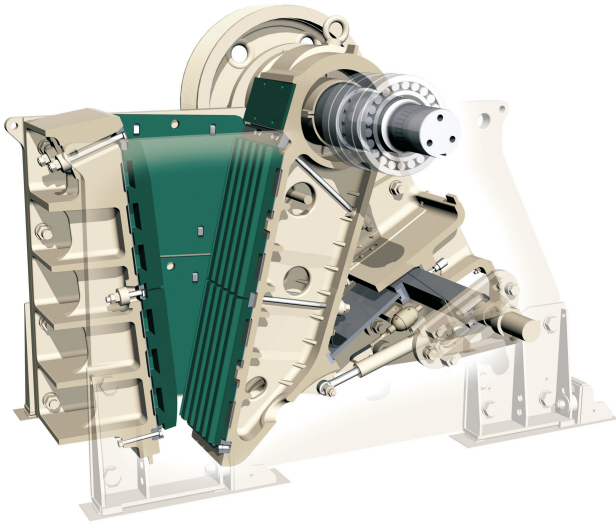

Figure 2.2: *Single toggle jaw crusher design. Image courtesy of Metso Minerals.*

2.2.1 Description of the jaw movement in a common single toggle jaw crusher

A common single toggle jaw crusher's crushing cavity consists of a stationary jaw, two side plates, and a moving jaw with a total of four pivoting points. Figure 2.3 shows a schematic of the single toggle jaw crusher with pivot points numbered from one to four. The movement of the jaw crusher is exaggerated and the dimensions of the parts may not be correct to the real applications. The external force is rotating a flywheel on an axle at the pivot point (1). The rotation of the eccentric axle moves the pivot point (2) of the moving jaw, and causes horizontal and vertical movement of the jaw. In this work the vertical movement is called the lateral or sliding movement of the jaw, and the horizontal movement the compressive movement of the jaw. The moving jaw is connected to a pitman with a pivot point at the lower end of the moving jaw (3). The other end of the pitman is connected to the support frame with the fourth pivot point (4). The stationary jaw is fixed to the support frame.

The flywheel rotation of the single toggle jaw crusher causes spherical movement of the upper end of the moving jaw. The throw of the crusher depends on the eccentricity or the distance between the pivot points (1) and (2). Figure 2.3 illustrates the rotation of the jaw crusher in three positions. In a) the upper end of the jaw is almost fully open and the rotation of the axle (1) from position a) to b)causes the initiation of the compressive movement. The lower end of the jaw at a) is closing at the same time the upper end is opening. In position b) the lower end of the jaw is close to the closed site setting (CSS) with a minimum gap between the jaws, and the moving jaw is lifted to its highest position. The upper end of the jaw is in the crushing part of the cycle when the crusher is rotated from position b) to c). The moving jaw moves downwards and compresses the larger rock particles. At the same time the lower end of the moving jaw is opening towards the open side setting (OSS). The configuration of the pivot points defines the movement of the jaw crusher. The benefit of the single toggle crusher is that there are two crushing events in one rotation cycle. One half of the cycle crushes the smaller sized rocks at the lower part of the jaw, while the opening of the upper part at the same time allows new rocks to fall lower into the jaw crusher. The

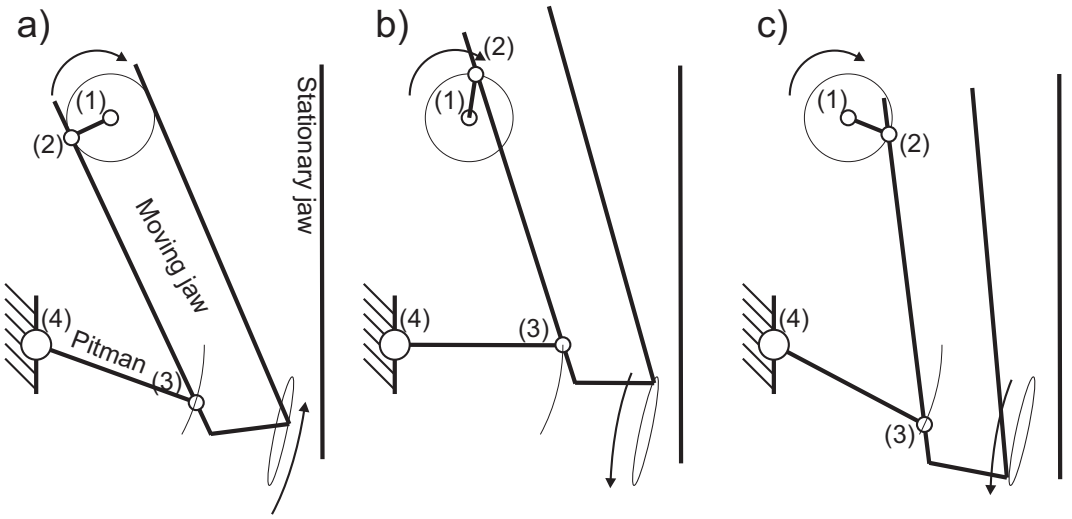

Figure 2.3: *Schematic of a single toggle jaw crusher at three positions of the crushing cycle. The elliptical circle shows the movement of the end of the moving jaw, and the arrows point the direction of the movement. The four pivot points are numbered from (1) to (4). In a) the lower end is moving towards CSS, in b) the lower end is opening from CSS and moving towards position c) close to OSS.*

second part of the cycle crushes the larger rocks at the upper end of the jaw and the opening of the lower end allows the crushed rock to fall from the jaws.
The movement of the moving jaw at the upper end of the jaw follows a spherical path, whereas the movement at the lower end of the jaw follows a very narrow elliptical path. Most of the movement at the lower end of the jaw is lateral, which causes sliding of the rock particles against the stationary jaw, when the crusher is moved from position a) to b). The larger amount of sliding means increased amount of wearing of the wear plates near the lower end of the jaw [4]. However, the movement of the jaw crusher improves the crushing capacity of the jaw as the vertical motion at the upper part of the moving jaw helps to push the rocks towards the release end of the jaw.

The jaw crusher is powered by an electric motor, which is rotating the flywheel. A small amount of the kinetic energy stored in the momentum of the flywheel is consumed each cycle. The electric motor is used to keep the flywheel rotating at a certain speed. If the energy consumption per cycle overcomes the electric motor power, the speed of the jaw crusher decreases, and can in the worst case cause seizure. Crushing of rocks consumes energy in the compression cycle, but also the rotation of the eccentric axis requires energy. Therefore, the idle power consumption of jaw crushers is about 50 % of the full load power consumption during crushing [5].

2.2.2 Wear tests with a jaw crusher

The wear mechanism occurring in jaw crushers is generally described with a term gouging abrasion, in which sizeable grooves are generated onto the wear surface [20]. Gouging wear tests have been conducted for several decades as field tests or in more controlled laboratory tests. Sare and Constantine [21] criticized the use of simple laboratory tests such as the

pin abrasion test to assess an application involving also other wear mechanisms. In the pin abrasion test the pin is pressed with a constant load against a rotating counterbody, which typically is a SiC grinding paper. Instead, Sare and Constantine [21] supported the use of a pilot scale equipment for field wear testing. Blickensderfer [22] proposed certain criteria to improve the quality of a field wear test. The use of a test specimen should not change the wear conditions and geometry, and a shorter test time has to be used compared to the time for the wear part to become obsolete. However, field tests are expensive and require more time and manpower when compared to laboratory scale tests. Therefore, the laboratory test methods have also been under development since the beginning of the 20th century. Hall [23] and Ksenofontov [24] used small laboratory-size jaw crushers to rank materials according to their wear resistance. In 1971, Borik and Sponseller [25] modified a jaw crusher to facilitate testing with parallel and flat specimens instead of crowned and corrugated surfaces, which allowed easier manufacturing of the specimens. They used a stationary jaw plate as the test sample and a moving jaw plate as the reference sample, and the test result was the ratio of the weight losses of the test and reference samples. The reproducibility of the test was found to be good. Borik and Sponseller [25] also noted that the stationary jaw has a higher wear rate than the movable jaw. Borik and Scholz [26] used the same method to assess the gouging wear resistance of several types of materials. In 1980, Sare and Hall [27] compared the test procedures from a statistical point of view. They argued that using the reference material in the movable jaw and the test material in the stationary plate gives information about the relative wear but not about the experimental error. When the stationary jaw wear rate is differing from the movable jaw due to the jaw geometry, also the wear rate comparison is affected. These deficiences can be overcome by running a new test for each material, where the test and reference specimen places are switched. Sare and Hall continued that when the two tests were compared using the reference specimen, the standard error increased when comparing the test specimens. They suggested an alternative procedure of testing all the materials against each other, where the reference material would be one of the test materials. As the number of tests in a series is twice the number of test materials, each material is tested twice in the same jaw position. This procedure was also used by Sare and Arnold [28]. American Society for Testing and Materials published a modification of this procedure as a standard ASTM G 81-97a [1], where both jaws were split in half to contain a reference material side and a test material side, and the reference material would be in a place opposite to the test material. The advantage was that one test was enough to find the wear ratio of one material to the reference with a same precision as with the previous procedure using only half of the number of tests. However, in 1991 Sare and Constantine [29] pointed out that the ASTM G 81-97a was disregarding the variability of the reference material and suggested a procedure, where the split pair specimen would be tested without a reference specimen. Table 2.3 shows the test sample placement of test materials A, B, and C and the reference material R in five test arrangements.

Lindqvist and Evertsson [30, 31] studied the wear of jaw and cone crushers. They built their wear model to be proportional to the pressure p that is caused by the compressive movement. Wear W is a sum of the sliding and compressive components, and for single compression it can be written as

$$\Delta W = \frac{1}{W_c} \int_0^1 pvdt + \frac{p}{W_s} \tag{2.6}$$

where W_c is the wear coefficient of the sliding term, W_s is the wear coefficient of the compressive term, and v is velocity. Another model that they used for the cone crusher was the sum of the normal pressure p_{normal} and the shear pressure p_{shear} [32]:

Table 2.3: *Comparison of the jaw crusher test procedures. The test materials A, B, and C are compared to reference R.*

Ref	Stationary / Movable	1	2	3	4	5	6
[27]	S	R	R	R			
	M	A	B	C			
[27]	S	R	R	R	A	B	C
	M	A	B	C	R	R	R
[27]	S	A	B	C	B	C	A
	M	B	C	A	A	B	C

Ref	Stationary / Movable	1	2	3
[28]	S	R A	R B	R C
	M	A R	B R	C R
[29]	S	C B	A B	C A
	M	A C	C A	B B

$$\Delta W = \frac{1}{W_\epsilon}(p_{normal} + K_s p_{shear}) \tag{2.7}$$

where W_ϵ is a wear resistance related parameter and K_s is a parameter scaling the effect of shear pressure when no slip occurs.

2.3 Tribology and contact forces

Hutchings [33] defines tribology as the science and technology of interacting surfaces in relative motion. Such interactions are friction and wear, and the interaction of lubricants with those factors. Several points have to be considered when examining the contact forces between the rock and the jaw plate and the resulting wear. This chapter discusses how the surface topography, contact and friction between the surfaces are defined and measured.

2.3.1 Surface profile

Even visually smooth surfaces are wavy and rough in the micro- or nanoscopic scale [34]. These surface height deviations can be measured with various types of profilometers. The surface profile is defined as an intersection of the real surface by a specific plane [35]. The earliest profilometers moved a mechanical surface contacting probe on the specimen surface, which measured the surface profile of a single line as displacements of the probe along the measured path. Similar line scanning can also be achieved for example with laser profilometers, which project a focused laser beam on the target and measure the surface height from the reflection path of the light. Several statistical values can be calculated from the surface profile, such as the arithmetic mean height or the average roughness R_a of the profile, or the root mean square (rms) roughness R_q [33]. The mean roughness depth R_z is the mean of the single heights of the sum of the largest profile peak and valley taken within the sampling length l_r [35]. Equations (2.8) and (2.9) show the definition of the R_a and R_q values:

$$R_a = \frac{1}{L_p}\int_0^{L_p} \mid z(x) \mid dx \tag{2.8}$$

$$R_q = \sqrt{\frac{1}{L_p}\int_0^{L_p} z^2(x)dx} \tag{2.9}$$

where z is the height of the profile that deviates from the mean profile height at the position x from the origin, and L_p is the overall length of the profile. Several measures are needed to explain the profile roughness, as for example the average roughness gives no information about the shapes or spacings of the surface irregularities. These can be measured as the profile height probability distribution and the spatial distribution of peaks and valleys of the profile, and can be described with an amplitude density function $\rho(z)$ that is proportional to the probability of finding a point on the surface at height z above the mean line [33]. A symmetrical profile leads to a symmetrical amplitude density curve about the position of the mean height. Asymmetric surface leads to skewness S_k of the density curve defined as

$$R_{sk} = \frac{1}{{R_q}^3}\int_{-x}^{x} z^3\rho(z)dz \tag{2.10}$$

where R_q is the standard deviation of the amplitude density function. Figure 2.4 presents four surface profiles, where in a) R_{sk} is positive, in b) negative, and in c) and d) the skewness is zero due to the symmetry of the surface [36].

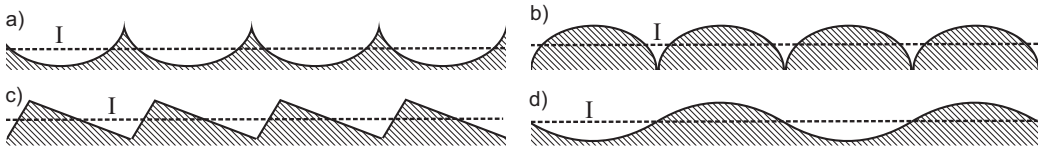

Figure 2.4: *Examples of skewness profiles. R_{sk} is positive in a), negative in b) and zero in c) and d) [36].*

Equation (2.11) shows another measure, which is the kurtosis R_{ku} or the sharpness of the peak of the height distribution curve:

$$R_{ku} = \frac{1}{{R_q}^4}\int_{-x}^{x} z^4\rho(z)dz \tag{2.11}$$

A kurtosis value less than 3.0 indicates a broad and flat distribution curve, and a value higher than 3.0 a more sharply peaked distribution [33].
Rough surfaces are usually not flat but corrugated, and they can have concave or convex shapes. The shape of a complex surface is included in the surface profile, but it is not relevant information regarding the roughness of the surface. Filters can be used to separate the longwave and shortwave components of the profile. ISO standard (ISO 11562) defines three filters that separate the surface texture profile into longwave and shortwave components: The Ls filter defines the intersection between roughess and shorter wave components, the Lc filter defines the intersection between roughness and waviness components, and the Lf filter defines the intersection of waviness and even longer wave components.
The primary profile, the roughness profile, and the waviness profile are separated by the above mentioned Gaussian filters [35]. The nominal form (tilt) has been removed from the raw profile to show the shape of the primary profile. The waviness profile takes into account the wave components that remain between the Lc and Lf filters, where Lc cuts the shorter roughness related wave components and Lf the longer form related components. The

roughness profile is formed from the wavelengths between the Ls and Lc filters, where the long wave components are cut with the Lc filter and the very small components with the Ls filter.

2.3.2 Surface texturing

The surface profile can be extended by scanning several parallel lines to produce areal measurements. Alternatively, several measurement techniques such as white light interferometry, focus variation and confocal microscopy can produce areal surface contour maps by vertically scanning the optical field of view. In these methods the resolution of the map is limited by the used magnification of the objective. The surface contour maps are visually efficient but the data needs to be processed for numerical comparison. A scale limited surface is created using Ls, Lc and Lf filters that remove the shortest and longest wave components [37].
The average roughness or the arithmetical mean height S_a of the scale limited surface is defined as

$$S_a = \frac{1}{A} \iint_A \mid z(x,y) \mid dxdy \tag{2.12}$$

where A is the defined area of measurement, x and y the position coordinates, and z the height of the scale limited surface. Similarly the root mean square height S_q, the skewness S_k, and the kurtosis S_{ku} of the scale limited surface are defined as [37].

$$S_q = \sqrt{\frac{1}{A} \iint_A \mid z^2(x,y) \mid dxdy} \tag{2.13}$$

$$S_k = \frac{1}{{S_q}^3} \left[\frac{1}{A} \iint_A \mid z^3(x,y) \mid dxdy \right] \tag{2.14}$$

$$S_{ku} = \frac{1}{{S_q}^4} \left[\frac{1}{A} \iint_A \mid z^4(x,y) \mid dxdy \right] \tag{2.15}$$

2.3.3 Contact between surfaces

The contact occurs only between the highest irregularities of the surfaces, when two rough surfaces are pressed against each other. This means that the real area of contact is smaller than the apparent area of contact. As the true area of contact is smaller than the apparent area, also the pressure between the contacts is higher than that of the apparent area. The elastic deformation of surface asperities can be estimated with a Hertzian contact of sphere and plane:

$$a = \left(\frac{3F_N r}{4E} \right)^{1/3} \tag{2.16}$$

where E is the modulus of elasticity, r the radius of the sphere, F_N the normal force, and a the radius of the contact circle between the sphere and the plane [33]. The maximum shear stress beneath the indenter occurs at a depth $0.47a$ that initiates plastic flow when a yield criterion is reached. The zone of plastic deformation extends eventually to reach the surface as the normal force F_N is increased. The mean pressure over the area can rise up to 3 times the uniaxial yield strength σ_y of the material before fully plastic indentation occurs. This is due to the two thirds of the applied pressure that goes to hydrostatic pressure and does not affect the production of plastic flow [38]. In a surface with many contours, the pressure is

divided to an increasing number of surface contours with increasing normal force. The real area of contact is found to be linearly proportional to the normal force [39].

2.3.4 Friction during sliding

Amontons' three laws of friction [33] describe the relation between the normal and frictional forces in the apparent contact of two surfaces:

I Normal force F_N and tangential force F_T caused by friction are proportional, $F_T = \mu F_N$, where μ is the friction coefficient.

II Tangential force of friction is independent of the apparent area of contact.

III Tangential force of friction is independent of the sliding velocity.

These laws are true for many materials and many conditions, but not for all [33]. In metals the change of environment can cause high fluctuations as the friction is highly affected by the oxide layer on the metal surface. The lack of oxide layer causes adhesion of the surfaces that form asperity junctions with a certain cross-sectional area A_j. The real area of contact A is the sum of these asperity junctions. In a plastically deformed state, the pressure is close to the indentation hardness H of the softer material, and the relation to normal force is F_N =AH, if the asperities are supporting the load. If sliding occurs between the surfaces, the junctions can be presumed to have a shear stress τ required to break the junction, and friction force of the junction due to adhesion becomes F_{adh} =Aτ. The adhesive friction coefficient of these components is constant $\mu_{adh} = \tau/H$ [40]. The yield strength σ_y is about 1.7 to 2 times the yield strength in pure shear τ_y, and $H \approx 3\sigma_y$, thus $\approx 5\tau_y$. Then μ_{adh} can be estimated to be ≈ 0.2 [33]. In contrast, Tabor [38] notes that after the yield point σ_y has been reached, the ideally plastic material passes the ultimate tensile strength UTS of the material, thus UTS = 0.33H.
In addition to adhesion of the surfaces, frictional forces are also caused by larger scale plastic deformation when harder asperities are ploughing the surface of the softer material. In a plane strain model, the friction coefficient μ_{def} caused by a wedge of semi-angle α_{sa} is $\mu_{def} = cot\alpha_{sa}$ [33]. The sum of μ_{adh} and μ_{def} is around 0.3, when the slopes of the surfaces are typically less than 10°. However, higher coefficients of friction can be achieved with metals. This is explained by junction growth during sliding, when the junction's true contact area A increases due to plastic deformation. When a tangential force F_T is applied, the junctions experience an additional shear stress τ. To remain in the point of yielding, this additional shear stress means that the yield pressure p_0 caused by the normal stress must be reduced to value p_1, and the area of contact must grow. Equation (2.17) shows the relationship determined by Tresca's yield criterion. Equation 2.18 shows the same relationship using normal and tangential forces [33].

$$ {p_1}^2 + 4\tau^2 = {p_0}^2 \tag{2.17} $$

$$ {F_N}^2 + 4{F_T}^2 = A^2{p_0}^2 \tag{2.18} $$

Equation (2.18) allows the coefficient of friction to rise to very high values, but usually it is limited by the ductility of the deforming material or the presence of a weak interfacial film [33].

2.4 Wear of metals

Wear is usually defined as an unwanted material loss or damage to a surface. The wear situation can be classified into several categories, and DIN 50320 standard divides wear into four mechanisms [2]. Adhesive wear occurs by the formation and breakage of adhered junctions or bonds. Abrasive wear occurs when a hard particle or a hard protuberance of a countersurface is forced against and sliding along a softer surface [33]. In surface fatigue material is lost when cracks that are forming on the surface due to cyclic loading grow large enough. Tribochemical reaction describes material loss due to chemical interactions in the contact, e.g., due to the removal of the oxide layer by corrosion.

Wear is usually measured as mass loss W_m of the wearing object or as volume loss W_V from the specific location of the object. For example in scratch tests, the slider can plough material to the sides and produce a groove. A certain volume of material is displaced but not necessarily detached from the surface. The deformation damage of the surface, which does not remove material, is difficult to measure. Cracks, flakes and grooves can cause damage to the system by increasing the surface roughness, which can cause increased friction in the tribosystem. In other environments the surface damage can cause initiation of fatigue fracture, or increase the corrosion rate of the material. Usually wear is only measured as the amount of volume loss of the object as detached particles, which can be obtained from the weight measurements, if the density ρ of the material is known. The volume loss can also be determined with surface profilometry, if the original dimensions of the object are known.

The measured wear is accumulated either from a continuous wear event or from several events, and the amount of wear depends on the length and number of these events. Wear rate can be used to compare the wear situations that have different number or length of events. The most exact measure of wear is found in scratch testing, where wear W is defined as a function of distance L the slider has grooved the surface, i.e., $W_m/L(g/mm)$. In more complicated tests wear can be related to the nominal sliding distance, which does not represent the actual sliding distance, but where the nominal and actual length of sliding can be directly related. The time dependency of the wear rate can be used if the sliding motion is uncertain or unmeasurable. Then, wear per test time W_m/t (g/s) is usually used. In crushing applications, the wear rate is usually also dependent on the amount of comminution of the crushed material, and is announced as wear per mass of crushed material W_m/m $(g/kg\ or\ g/ton)$.
Wear resistance is the capability of a material to resist wear, and is thus the inverse of wear $\frac{1}{W}$. Relative wear resistance $\varepsilon = \frac{W_{ref}}{W_{mat}}$ is often used in the wear comparison, where W_{mat} and W_{ref} are the wear of the test and reference materials, respectively.

2.4.1 Abrasive and adhesive wear

Because of the closeness of abrasive and adhesive mechanisms, both mechanism are generally active in a wear situation. In adhesion, the deformation of the contact faces can result in work hardening of the protuberances, which can then act as abrasive protuberances. In abrasion, a film of adhered material can form on the surface of the abrading particle, and adhesion can occur between the adhered material and the counterface. Atkins [41] criticized the division of wear into these two categories due to the mixed nature of adhesion and abrasion, as both categories can have same acting wear mechanisms. He suggested the use of the term "penetrative wear" instead.

Archard's [42] study of adhesive wear is widely used to explain the relationship between wear and the contact forces, and is also used in abrasive wear. Archard's theory postulates that the wear rate is proportional to the load and is independent on the apparent area of contact. Archard's equation 2.19 shows that the volume wear W_V is dependent on the normal force F_N and sliding distance L, and on the inverse of the hardness of the material. K_{ad} is a dimensionless coefficient of adhesion wear that can be determined experimentally.

$$W_V = K_{ad} \frac{F_N L}{H} \tag{2.19}$$

Equation 2.20 rewrites the Archard's equation (2.19) as the volume wear rate per unit sliding distance:

$$\frac{W_V}{L} = K_{ad} \frac{F_N}{H} \tag{2.20}$$

The wear rate in adhesive contact is then the ratio of the external pressure and the material's capability to resist the pressure, i.e., its hardness. The wear coefficient K_{ad} contains the unknown factors. Several studies have been conducted to characterize these factors and to modify equation 2.20 also to fit the abrasive test results. For example Khruschov [43] listed several basic principles of abrasive wear during friction against fixed abrasive grains:

- Linear wear Δl is directly proportional to the stress σ and the friction path ΔS: $\Delta l = c \cdot \sigma \cdot \Delta S$, where c is a proportionality coefficient.
- The relative wear resistance ε in pure annealed metals is directly proportional to the hardness H: $\varepsilon = c_2 \cdot H$, and correlates with the modulus of elasticity E: $\varepsilon = c \cdot E^{1.3}$, where c and c_2 are coefficients.
- The relative wear resistances of the heat treated structural steels show linear dependence on the bulk hardness: $\varepsilon = \varepsilon_0 + c_3 (H - H_0)$, where ε_0 and H_0 are the relative wear resistance and hardness of the material in annealed condition, and c_3 is a coefficient.
- The relative wear resistance is not affected by work hardening if the abrasive hardness is higher than the hardness of the cold work hardened structure.

The abrasive contact situation can be described by several qualifying terms that classify abrasion according to the wear environment, the geometry and speed of the contact, and according to the mechanical properties of the particle and the counterface material.

2.4.2 Classification by the wear environment

The environment of the abrasive particle or protuberance defines how constrained the movement of the abrasive is when it contacts the counterbody. Sliding abrasion or **two-body abrasion** is used to describe a situation where the abrading particles or protuberances are fixed to one surface that restrains the possibility of rolling of the particles [44]. The fixed position causes the abrasive event to be conducted at a fixed angle between the face of the particle and the countersurface. This term is typically used to describe grinding, scratch tests, or pin-abrasion tests. There are also other tests that can fit into this category, such as the sliding contact vs. rolling contact test by Mouritz and Hutchings [45]. In this test, the contact is closer to two-body abrasion with a steel body in contact with a large rock

counterface.

In rolling abrasion, the particle has no fixed support when pushed against the wearing surface, but it relies on the support of a counterface or other particles. The term **three-body abrasion** has often been used, when the abrading particles are between two surfaces with a freedom to roll or slide against the surfaces [46]. The abrasive particle is momentarily fixed to either of the surfaces, described here as the third body that supports the particle enough to enable sliding or rolling movement against the counterface. Axén et al. [47] showed that the hardness of the counterbody is an important factor in three-body abrasion. The increasing hardness of the specimen can result in a decrease in wear resistance, if the hardness of the counterface is overcome. Yang and Garrison [48] showed that the microstructural features improving the wear resistance in two-body abrasion lead to a similar influence on the wear resistance in three-body abrasion. Gates [49] argued that the classification of abrasion into two or three-body abrasion is flawed, and it would be preferable to base the classication on the severity of the wear. Also, Fang et al. [50] considered two-body abrasion to be a special case of three-body abrasion, where all the particles are sliding on the surface. In contrast, Wang and Wang [51] proposed a wear model for the three-body abrasion category, where the interactions between the abrasives and the wearing surfaces are primarily by indentations.

Erosion defines a situation, where the particles have a high degree of freedom of movement when they are contacting the surface [2]. Material is removed from the target surface due to abrasion, or in the case of a brittle material, due to fracturing. The kinetic energy of the particles is an important factor, and the definitions of impact-erosion or impact-abrasion are used when the particles have a high velocity or momentum. The proper use of the terms have been under investigation. Gates et al. [52] studied the ball mill wear mechanism and found that the impact-abrasion is not a suitable description for the ball mill environment and suggested the use of high-stress abrasion instead, which classifies the situation according to the mechanical strength of the abrasive particles.

Open and **closed** systems are also used to describe the environment. In a open system the wear debris is removed from the system and does not affect the wear rate. In a closed system the wear debris can affect and change the wear environment properties either by acting as loose abrading particles or as solid lubricants.

2.4.2.1 Chemical environment

The chemical reactions between reagents and the surfaces can influence the outcome of wear. Corrosion or oxidation can produce a surface layer that can also be beneficial by reducing the friction and preventing adhesion between the metal bodies. The oxides, however, can also have a detrimental effect by acting as abrasive particles in closed systems.

The effect of humidity in abrasive wear has been investigated by several authors [53–55]. The presence of humidity can increase the wear rate in two-body abrasion but is found to be important only at low wear intensities. In three-body abrasion the humidity can assist the fracturing of particles to produce fresh particles with high angularity, thus increasing the wear rate. Bingley and Schnee [56] studied the wear of metals under wet and dry three body conditions and concluded that the wet conditions with larger particles of 60 μm in size promoted wear by sliding and cutting.

The environment can also change the properties of the abrasive particles. Bohloli and Hoven [57] examined how water affects the comminution in the cone crushing environment and concluded that the influence of water decreased the tensile strength of the rock and produced less fines.

2.4.3 Contact geometry: ploughing, prow formation, or cutting

The geometry of the contact between the particle and the counterface defines whether the contact is ploughing on the surface or whether the contact is defined as cutting. In general, when the attack angle α_a is small, the contact is defined as ploughing, where a sliding particle pushes the counterface material to the sides of the groove. Figure 2.5 shows the basic shapes of ploughing and cutting abrasion.

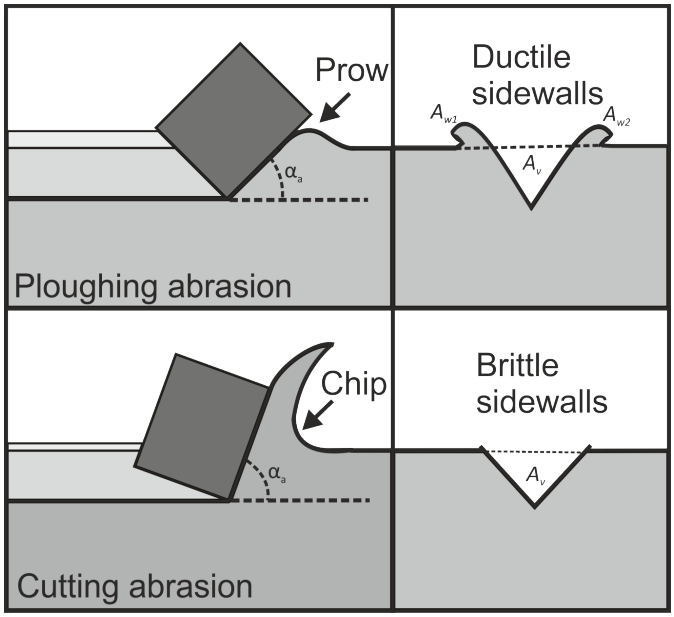

Figure 2.5: *Ploughing and cutting abrasion, showing the prow and chip formation and the attack angle α_a of the abrasive particle*

Rabinowicz [58] included the effect of the opening angle θ of a conical abrasive to the volume wear W_V of the specimen material. Equation 2.21 shows the wear rate form of the Rabinowicz equation, which is similar to the Archard's Equation 2.20. The K_{ad} of adhesive wear in equation 2.20 is now defined as the cotangent of the average opening angle of the abrasive particles, i.e.,

$$\frac{W_V}{L} = \frac{cot\theta F_N}{\pi H} \tag{2.21}$$

With increasing attack angles the geometry of the contact increases the size of the prow in front of the scratch head. Challen and Oxley [59] showed that a slip line field model gives a steady state volume wear over a given distance as:

$$\frac{W_V}{L} = \frac{1}{\sqrt{2\tau_f}} \frac{cos(\alpha_s + 0.5cos^{-1}\sigma_f)}{cos(\pi + (\alpha_s - 0.25\pi + 0.5cos^{-1}\sigma_f))} \tag{2.22}$$

where α_s is the slope of the asperity, σ_f the strength of the interfacial film $\sigma_f = \tau_y/k$, τ_f is the shear flow stress of the softer material, and τ_y the shear strength of the film. Challen et al. [60] suggested a critical angle α_c where the wear debris changes from torn-off wear particles into chip formation, when $\alpha_a > \alpha_c$. At the critical attack angle α_c, the prow becomes unstable and starts to cut material into chips. Generally, the wear as a removal of material is higher in cutting than in ploughing, where the material can also be displaced on to the surface instead of being removed. Bates et al. [61] examined the transition from ploughing to cutting with a pin-on-disc device inside a scanning electron microscope. They reported a three-step process: first a bulge is formed in front of the slider, followed by a crack propagating parallel to the sliding direction. In the third phase, the wear debris platelet is pushed forward while remaining attached to the bulge.

In addition to the ploughing and cutting modes, Hokkirigawa and Kato [62] included the wedge formation mode as the transition zone between ploughing and cutting. In their results the cutting mode activated with the increase of penetration. The presence of the wedge formation mode was dependent on the high shear strength of the contact interface. When the penetration depth was kept the same, the degree of wear increased with increasing hardness of the material. Kitsunai et al. [63] conducted repeated pass scratch tests and defined a fourth mode of contact as shear tongue forming in front of the indenter. The mode changed from ploughing through shear tongue mode to wedge formation, and ended in the cutting mode when either the load or the number of passes was increased.

The wear volumes of a ploughing groove and a cutting groove are different, and also depend on how the wear is defined. For example, Torrance [64] suggested that the scratch tests with a ploughing Vickers indenter remove material mainly by removing the side walls of the groove. This behavior is enhanced by the roughness of the specimen surface. In ploughing, fractured or flaky side walls of the groove remain in single pass scratch tests, but can be easily removed with overlapping passes. Zum Gahr [2] rised a question whether the loosely adhered particles on the surface should already be considered as wear debris.

Garrison [65] suggested that for ploughing the volume wear rate can be written as

$$\frac{W_V}{L} \approx \frac{(1-f)F_N}{H_{def}} \tag{2.23}$$

where f is the fraction of a wear groove ploughed to either side of the abrasive particle but not removed from the surface, and H_{def} is the hardness of the deformed material. He concluded that in ploughing the term $(1-f)$ depends primarily on the ductility and not on hardness. Zum Gahr [66, 67] concluded that in scratch testing the ratio of the volume removed by microcutting to the volume removed by ploughing, f_{ab}, can be obtained from the ratio of the positive and negative areas of the groove cross-section as

$$f_{ab} = \frac{A_v - (A_{w1} + A_{w2})}{A_v} \tag{2.24}$$

where A_v is the cross-sectional area of the groove and A_{w1} and A_{w2} are the cross-sections of the material pushed to the sides of the groove. When no material has been detached, the value of f_{ab} is 0 and the abrasion causes only ploughing. The higher the value of f_{ab}

is, the more of the material has been detached by scratching. When f_{ab} is 1, the removal mechanism is ideal microcutting.

2.4.4 Surface deformation and fatigue

Although surface fatigue is classified as its own wear mechanism, the transition from ductile grooving to brittle grooving is not straightforward. Continuous overlapping grooving can produce a highly deformed layer on the wear surface that can wear by fracturing. This fracturing is often associated with a tensile wave that follows the scratch head. Suh [68] proposed a delamination theory for the chip removal in slow speed sliding wear, where the crack nucleates at the subsurface and propagates towards the surface. Once meeting the surface the particle is removed by the crack bending under tension towards the slider passing over.

Multiple pass scratch testing has been used to produce a more controlled wear test. Shetty et al. [69] compared the multiple pass scratching with a diamond indenter and with irregular Al_2O_3 particles. They concluded that the deformed surface features produced by the Al_2O_3 particles corresponded to the low-stress rubber wheel abrasion tests (RWAT), whereas the features produced by the geometrically better defined diamond indenter did not. Xie and Williams [70] also conducted multiple pass scratch tests with varying attack angles α_a of the indenter and measured the wear rate of the specimen. They concluded that the average wear rate W_{wr} can be written as:

$$W_{wr} = \frac{V\mu}{F_T L} = \frac{\mu r_{def}}{C\tau_k \epsilon_t tan^2\alpha_a} \left(\frac{h_s}{h+h_s}\right)^{0.5} \tag{2.25}$$

where V is the removed volume, L is the sliding distance, F_T is the tangential force, r_{def} is proportional to the total work going to plastic deformation, C is a constant, τ_k is the average shear flow stress, ϵ_t is the true fracture strain, h is the depth of penetration, and h_s is the height of the ridges of previous grooves.

Even if the wear surface was originally smooth, the abrading conditions are bound to increase the roughness of the wearing surfaces. The geometry of the contact between the wearing surface and the abrasive particles is changing with the roughness. Slip-line field analysis of rough surfaces showed an increase of wear with increasing roughness of the surface [71]. The wear rate was also found to depend on the elastic modulus-to-hardness ratio of the abraded softer surface.

2.4.4.1 Speed of abrasion

The strain rate of deformation on the grooved surface is dependent on the speed of the abrading particle. The local deformation at higher strain rates can cause heating of the deformed surface, which can change the mechanical properties of the materials. Misra and Finnie [44] experimented on the sliding speed in two-body wear contact and found that the wear resistance increases with increasing sliding speed up to 65 mm/s. They suggested that the increase in the wear resistance is due to the increase of flow strength with increasing strain rate. Misra and Finnie [72] concluded that the size effect of the abrasive particles causes lower wear with particles below 100 μm, as the shallow surface layers exhibit higher flow strength against abrasion.

2.4.5 Material properties

The wear resistance of a material is not a material property. The test environment defines, which material properties are important for the wear resistance. In many cases the most relevant mechanical properties are the tensile yield strength as the ability to resist deformation and the ductility as the ability of the deformed surface to resist fracturing. Other material properties influencing the abrasive wear are the crystal anisotropy, mechanical instability, strain distribution, work hardening capability, and fracture toughness [2]. Hardness of the material is the most used measure in the comparison of materials' wear resistances.

2.4.5.1 Hardness

Indentation hardness is the most used measure of the wear resistance due to the simplicity of its measurement, and as the higher indentation hardness can in many cases be assumed to provide better abrasion resistance. Hardness is not exactly a material property, but can approximate the tensile strength of the material. The hardness test can be considered as a controlled surface deformation test that measures the material's resistance to deform by indentation. However, abrasion requires lateral movement of the particle to slide on the countersurface and to deform the material on the surface for high strains. Otherwise it is more preferable to classify the contact as indentation, where the deformation is local and strains are lower. The size of the indentation can be used for measuring the hardness of the material. Similarly, scratch tests can also be used to determine the scratch hardness, and the results are generally comparable [73]. However, Atkins and Liu [74] showed that the depth of the groove in sliding was smaller than the depth of the static indentation, when the attack angle α_a was very small. Higher velocities can also cause changes in the scratching results with materials having time dependent properties [73].

During abrasion the plastic deformation usually increases the hardness of the surface layer. The amount of work hardening of the material is important for the extent of wear. Richardson [75] showed that the maximum hardness and the corresponding yield stress are related to the relative wear resistance of the material. The strength properties of the worn material depend also on the geometry and strength properties of the abrasive [76]. The wear resistance of the specimen material relative to the reference material is affected by the relation of the maximum hardness of the specimen and the hardness of the abrasives [77]. Also heterogeneous materials with harder phases were investigated. Richardson [77] concluded that when the size of the hard phases is less than the size of the wear debris, the hard phases act only effectively by strengthening the material. Phase sizes larger than the wear particles are more effective and act as obstacles in abrasion.

Equations 2.21 and 2.23 define the relation between hardness and wear. Torrance [78] also found a correlation between the wear resistance and hardness in the pin abrasion tests, and formulated this as

$$\varepsilon_i \approx \frac{H_i}{H_r}\left(1 + K\left(\frac{H_r}{E_r} - \frac{H_i}{E_i}\right)\right) \tag{2.26}$$

where ε_i is the relative wear resistance, E_i, E_r, H_i and H_r are the elastic modulus and the maximum hardness values H_U of the test (i) and reference (r) materials, when H_U is obtained from the tests of Richardson [75]. Torrance estimated that $H_U = H + 300 + 130C_{wt.}$, where $C_{wt.}$ is the carbon content in weight percent. Zum Gahr [79] stated that the ratio

f_{ab} in equation 2.24 can also be written using the deformation capabilities of the materials as:

$$f_{ab} = 1 - \left(\frac{\varphi_{lim}}{\varphi_s} \right)^{2/\beta_d} \tag{2.27}$$

where φ_s is the effective deformation on the wearing surface, φ_{lim} is the capability of deformation of the materials before microcracking occurs, and β_d is a factor describing the decay of deformation with increasing depth and depends on the work hardening behavior of the material, i.e., $\beta_d = (H_{def}/H)^{1/3}$. Zum Gahr [67] showed that the linear wear intensity $W_{l/s}$ of a scratch test can be written as:

$$W_{l/s} = \Phi_1 \left[1 - \left(\frac{\varphi_{lim}}{\varphi_s} \right)^{2/\beta_d} \right] \frac{p}{H_{def}} \tag{2.28}$$

where p is the applied surface pressure and Φ_1 is a geometrical factor describing the shape of the abrasive particles.

Figure 2.6, taken from Zum Gahr [2], shows that the wear resistance of various metals cannot be explained with bulk hardness alone. The hardness of pure metals follows a linear relationship to wear resistance, whereas more complex materials such as tempered steels and cold deformed steels may not. The proportionality is found by using the ratio of deformation hardness H_{def} and f_{ab}. However, Zum Gahr concludes that f_{ab} does not represent only the capability of deformation and hardness but involves also other factors of the material and the tribological system.

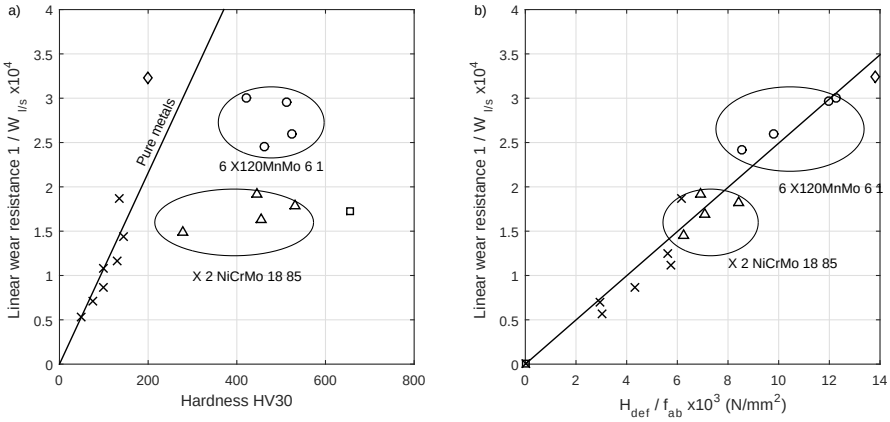

Figure 2.6: *Wear resistance against mesh 80 SiC grinding paper in a pin abrasion test with 0.71 MPa contact pressure versus a) hardness of the undeformed material, b) ratio of the deformed hardness and f_{ab} values of the wearing materials obtained from single scratch tests using a diamond scratch head [2].*

2.4.5.2 Fracture toughness

Fracture toughness is used as a measure of the material's resistance to crack propagation, and it is especially useful with brittle materials. Zum Gahr [2] concluded that it can be useful for predicting wear, as with higher hardness the fracture toughness often decreases. When a critical limit of the tensile stresses in contact is reached, the abrasive wear of brittle materials occurs by crack formation and propagation. Hornbogen [80] and Atkins [41] showed that the ductility and fracture toughness are also important in abrasive and adhesive wear. In similar blunt ploughing situations a brittle material can lose material by fracturing, whereas a ductile material is only ploughed aside by the scratch head. There is no clear division to brittle and ductile materials, as there is a transition range where the ductile wear by plastic deformation changes to increasingly brittle deformation with a higher chance of critical crack growth [80].

2.4.5.3 Effect of temperature on the microstructure in abrasion

Mechanical deformation causes heating of the specimens, and locally the temperature can rise to high values. The contact of adhesion or abrasion also causes a high degree of deformation on the surface, and the surface temperature of the contact points can rise to high levels. Moore [81] determined the contact temperature during pin abrasion by using the pin and the SiC abrasive grit as a thermocouple. He concluded that the temperatures in contact can rise to a range of 325°C - 900°C, when the overall temperature is compensated by the contacts that involve forming of chips. According to Eyre [82], the rubbing of contacts can rise the temperature up to the austenization temperature of steels and form a fine and dispersed microstructure known as the white layer due to its resistance to etching reagents. The hardness of the white layer was reported to rise up to 700 - 1200 HV [82]. The high hardness of the white layer can cause brittleness. Yang et al. [83] studied the effect of the white layer on the wear resistance of materials and concluded that the white layer in most cases decreases the wear resistance. The cause of this is the cracking of the white layer from the matrix and removal by delamination. Even through the temperatures can rise as high as to the austenization temperature, the time when the white layer is formed is very short. Xu et al. [84] used TEM to examine the white layered microstructure of a worn crater from impact tests with AISI 1045 steel specimens, and concluded that the white layers showed no phase transformation but nano crystallization of the original ferrite and cementite phases. Hosseini et al. [85] stated that the microstructure of the white layer is dependent on the reached temperature. Mechanically induced white layers form at flash temperatures below the austenization temperature due to severe plastic deformation, while transformation induced white layers form above the austenization temperature. The reported white layer microstructures of originally martensitic and bainitic stuctures contained primarily ferrite and cementite for the mechanically induced white layers, or martensite, austenite, and cementite for the transformation induced white layers [85].

2.4.5.4 Shear localization

When the material is deformed the strain can be distributed homogeneously or inhomogeneously. In a microscopic scale, the inhomogeneous strain distribution is concentrated in slip bands or shear bands. Inhomogeneous strain can also occur due to adiabatic heating of the shear band. The increased temperature causes thermal softening that results in shear localization. Shear localization is dependent on the strain-rate of the deformation, where

shear banding is impossible below a critical strain-rate limit [86]. The strain rate of abrasion is highest in a region close to the surface and decreases with increasing subsurface depth [87]. Low stacking fault energy of the microstructure favors inhomogeneous slip that results in discontinuous chips when cutting abrasion occurs [2]. The dislocation structure depends on the stacking fault energy, where low stacking fault energy favors planar arrays and high stacking fault favors cell structures. Vingsbo and Hogmark [88] showed the chip formation by adiabatic shear banding in martensitic steels in single pass pendulum grooving. Söderberg et al. [89] varied the penetration depth in the single pass pendulum test, and concluded that at shallow penetrations the materials rank according to their yield strength. With increasing groove size the thermal properties of the materials become increasingly more important.

Sundararajan [90] proposed a model for two-body abrasive wear that was based on the localization of plastic deformation. The abrasive wear coefficient K can be obtained as:

$$K = \frac{W_V}{F_N L} = \frac{\beta_c \mu (n+1)}{A_c S_0 (1 - C(T_c - 300)) e_c^{n+1}} \tag{2.29}$$

where β_c is the fraction of contacts with attack angle above the critical value α_c, μ is the friction coefficient, n is the strain hardening exponent, A_c is a parameter related to the flow stress with an average around A_c=1.5, S_0 is a constant related to the flow stress, C is the temperature coefficient of the flow stress, T_c is the average temperature of the chip, and e_c is the critical strain for the localization of deformation. The model was shown to fit to the experimental pin abrasion data obtained from the literature. The minimum possible value C_{min} of thermal coefficient C corresponds to the melting point T_m of the steel [90].

$$C_{min} = \frac{4.5}{{T_m}^{1.3}} \tag{2.30}$$

Coefficient K in Equation 2.29 uses flow stress S instead of hardness as a material property resisting wear.

$$S = A_c S_0 \epsilon^n (1 - C(T_c - 300)) \tag{2.31}$$

Flow stress is described as the sum of athermal, thermally activated and viscous components [90]. Equation 2.31 shows the athermal component dominated flow stress [90]. The athermal stress component consists of long range internal stresses, for example, from the increased dislocation density.
The thermally activated component is the resistance of dislocation motion caused by barriers in atomic scale, such as impurity atoms or variations in the Peierl's stress of moving dislocations within an atomic plane [91], and its effect decreases with the increase of the temperature. The thermally activated component of f.c.c metals is negligible compared to the athermal component, while with b.c.c metals it shows a major contribution to the flow stress mainly at temperatures below room temperature [90]. Sundarajan mentions also that the increasing hardness of the alloy increases the dominance of the athermal component over the viscous component until at high strain rates above 10^4 s^{-1}, where the viscous components become dominating [90]. Viscous components involve dislocation interactions with electrons and thermal vibrations (phonons) causing drag, which increases the flow stress [92].
In steady state wear the strain ϵ reaches the critical value e_c for chip formation, which can be larger than the strains achieved in the quasi-static mechanical testing [90]. The strain hardening exponent n does not stay constant but decreases when the strain reaches high values. With f.c.c metals the flow stress shows saturation at high strains, which causes n to

decrease indefinitely, whereas with the b.c.c metals the flow stress shows no saturation but n still decreases [90]. The strain hardening exponent depends also on the strain rate [90]. Investigations with scratch tests [93] and rubber wheel abrasion tests [94] show linear correlation between the wear of the specimens and the flow stress coefficient S_0, whereas the strain hardening exponent n obtained from the quasi-static tensile tests did not significantly correlate with the wear.
Sundarajan [90] proposed that the critical strain for localization and chip formation e_c can be estimated from the ratio of deformed hardness H_{def} and bulk hardness H of the material.

$$\frac{H_{def}}{H} \approx \left(\frac{e_c}{0.08}\right)^n \tag{2.32}$$

where the value 0.08 is an estimation of the additional strain caused by the hardness test.

2.4.5.5 Multiphase materials

This section concentrates on how the wear resistance is affected by the multiphase microstructure of steels and cast irons, containing carbide hard phases and softer phases. Kruschov [43] determined a rule of mixture, where the total wear resistance ε_T of a multiphase material is the sum of the wear resistance of the phases ε_{ph} multiplied by the volume fraction v_{ph} of the phases, i.e.,

$$\varepsilon_T = \Sigma v_{ph} \varepsilon_{ph} \tag{2.33}$$

Garrison [95] concluded that Equation 2.33 was valid when the volume wear rates of the phases were proportional to the load, but invalid when the wear rates were proportional to the pressure and thus depended on the area of contact. Simm and Freti [96] added that the rule of mixtures is valid if the groove depth is no larger than the size of the reinforcing particles. Colaco and Vilar [97,98] included the contribution of hard phases to the Archard's equation 2.20 and obtained

$$\frac{W_V}{L} = K\frac{F_N}{H} + v_{hp}\Psi \tag{2.34}$$

where v_{hp} is the volume fraction of the reinforcing particles and Ψ is a factor depending on the change of the volume loss caused by the reinforcing particles. Ψ can have a negative effect if the fracture of the reinforcing particles increases the volume wear.

The carbide hard phase has significantly higher hardness than the softer steel phases. It has also higher hardness than most of the usual natural abrasive phases, quartz and feldspar. The higher hardness of the carbides effectively prevents abrasion against softer materials. Al-Rubaie [99] showed that in the case of multiphase materials the equivalent hardness H_{eq} was related to the wear resistance of the materials in pin-abrasion tests. The equivalent hardness can be written as

$$H_{eq} = v_m H_m + v_{hp} H_{hp} \tag{2.35}$$

where v_m is the volume fraction of the matrix, v_{hp} is the volume fraction of the hard phase, H_m is the hardness of the matrix measured after the wear test, and H_{hp} is the hardness of the hard phase. The benefit of the carbide phases to the wear resistance also depends on the abrasion conditions. Albertin and Sinatora [100] conducted ball mill tests on several steels containing differing amounts of carbides, and concluded that the increase in the carbide percentage increased the wear resistance in less severe conditions of softer rock materials. With

quartz the wear rate was increased due to the removal of the metal matrix and the following cracking of the carbides. In addition to their hardness and volume fraction, the size and shape of the reinforcing particles also affect the wear resistance of the material. The effect of the reinforcing particle size on the wear resistance is dependent on the size of the abrasive protuberances or particles [2]. The carbides can be considered only as hardness increasing reinforcements of the matrix when the penetration volume is much larger than the carbide size.

The size distribution of the carbides can also be important. Hu et al. [101] conducted a numerical investigation on the effect of reinforcing particles on the wear resistance of materials. Their simulations showed that a proper combination of small and large reinforcement particles is more effective to improve the wear resistance than single sized particles.

The shape and composition of the carbides also affect the wear resistance of a multiphase material. Llewellyn [102] conducted jaw crusher tests according to the ASTM G81-97 standard and published the wear ratio of selected materials. He concluded that the steels containing M_7C_3 carbides suffer from increased gouging abrasion due to microcracking and microspalling compared to the steels containing primarily finer eutectic carbides. Liujie [103] compared a high vanadium and high chromium cast iron under rolling contact, and concluded that the fine vanadium carbides prevent crack initiation and growth. The wear occurred by fatigue spalling and the wear rate of the high chromium steel was four times higher than that of the steel containing vanadium. Wei et al. [104] studied the effect of the shape of vanadium carbides in high speed steels on the wear resistance with the pin abrasion test, and concluded that evenly dispersed and spherical particles produce the best wear resistance.

2.4.6 Abrasive particle properties

High-stress and **low-stress** abrasion are used to classify the abrasive wear using the abrading particles' mechanical properties as a limiting factor. If the crushing strength of the abrading particles is exceeded to break the particles, then the situation is called high-stress abrasion. If the particles remain unbroken, the wear situation is low-stress abrasion. Gouging abrasion is used to describe the high stress abrasion by bigger abrasive particles, which remove material from the surface in larger fragments [33].

2.4.6.1 Hardness

Abrading particle's properties are important to the resulting severity of the wear of the counterface material. Particle hardness needs to be 1.2 times higher than the hardness of the counterface material for abrasion to occur [38]. This transition from non-abrading to abrading motion is not exact with metallic protuberances. Torrance [105] showed that a protuberance that is 1.25 times harder than the counterface stops grooving after the flow stress is high enough to collapse the protuberance and the attack angle is reduced below 30°. Wear is also occurring in the protuberances in the case of equal or lower hardness to the counterface, which causes blunting of the protuberances of the abrading particles. Quartz has a Vickers hardness of 750-1200 HV, meaning that it is capable of abrading martensitic steels. Angularity and size of the particles or the protuberances are also important. Particles are most abrasive when they are sharp and conical and have a size between 100 μm - 500 μm [33].

2.4.6.2 Size

Avient et al. [106] tested experimentally the correlation between friction and wear in pin-abrasion tests between pure metals and emery paper. They found that in two-body abrasion the size of the abrasive does not affect the amount of wear, when the abrasive particle size is larger than 70 μm. The size independence of the amount of wear was also shown to be similar in tests with a three-body wear condition by Rabinowicz et al. [53]. They concluded that this critical size of the abrasive particles was connected to the size of the adhesive wear debris [58]. Woldman et al. [107] found that the removal of wear particles was dependent on the degree of penetration, and at very light loads the low degree of penetration created no sidewalls in ploughing, causing a high degree of wear.
Nathan and Jones [108] showed with a belt grinder-type abrasion tester that the abrasive size independence is valid only for abrasives below 150 μm, at speeds below 0.5 m/s, and with loads under 1 kg. Above these limits the wear results showed dependence on the mentioned parameters. With microscopic particles, the contact area relative to the abrasive surface area is quite large. The crystalline microstructure of microscopic particles consists of single or very few grains or phases, and the contact area relation decreases as the size of the abrasive increases. The amount of grains and phases can increase in larger particles, which creates a more homogeneous structure. When the particles are macroscopic, the contact area localizes in the protrusions of the particle.

2.4.6.3 Shape

The shape of the abrasive defines the actual abrasion geometry in a situation where the wearing surface is ideally flat. Increasing angularity or abrasivity with sharp protrusions allow smaller attack angles α_a in the contact, which promotes cutting abrasion. Kelly and Hutchings [109] showed with a modified ball cratering test that the abrasivity of silica particles with various sizes and shapes varied by a factor of six, which was mostly attributed to the different shapes of the particles. The shape of larger particles defines how the contact points are supported. A flat particle has less probability to roll on the surface than a round particle. Also, elongated or flake-like particles are usually mechanically weaker than round particles, as the contact points can be further apart from the centerline of the particle. The loads at the contact points can cause bending and increase the tensile stresses in the particle, which can result in fracture.

Various methods have been used to determine the shape of the abrasive [110, 111], and for example Hamblin and Stachowiak [112] and Stachowiak [113] developed a numerical characterization method for particle angularity. They concluded that the quadratic spike parameter SPQ had a linear correlation with the abrasive wear rates. SPQ can be obtained by evaluating the apex angle θ of the peaks in the profile of the abrasive particle as triangles:

$$SPQ = \frac{1}{n_p} \Sigma cos \frac{\theta_i}{2} \tag{2.36}$$

where n is the number of spikes analyzed. Stachowiak [114] correlated the morphology of worn surfaces to the measured shape of the abrasive particles, where rounded particles created smooth grooves and angular particles produced sharp indents and narrow cutting grooves.

2.4.6.4 Toughness

In addition to hardness, the fracture toughness of the abrasive particle determines how well the particle can withstand loading. The abrasives with ionic and covalent atomic bonds are brittle and break at low strains in tension with very little capability to deform [115]. The natural rocks contain multiple crystalline phases and can have various amounts of porosity and pre-existing cracks. These affect the amount of loading the particles can withstand. The strength of the particles in compression is higher than their strength in tension. However, loading of the particle in compression causes also tensile forces due to shearing, which can initiate growth of the pre-existing cracks [7].

2.4.6.5 Intermixing of abrasive particles with the metal matrix

The wear surface has various interactions with the abrasive particles. The penetration of particles into the material can result in an intermixed layer of abrasive particles and metal material of the matrix. The hardness of the matrix determines how deep the intermixed layer can develop. Yao and Page [116] concluded that right conditions of compression can develop a surface layer of the embedded comminution product and reduce the wear by ploughing or cutting. Heino et al. [117] stated that the wear resistance of steels with hardness between 400-800HV benefited from the embedded quartz layer, whereas steels with hardness less than 400 HV experienced a reduced wear resistance caused by the embedded particles.

2.4.7 Friction in abrasion

In addition to normal sliding friction, the abrasive particle can have increased coefficient of friction μ due to the deformation of the opposing surface. The friction depends also on the material selection, e.g., the contact between a diamond scratch head and a steel surface presents a low friction situation. Yurkov et al. [118] slid a diamond cone with a curved tip of 5 mm radius on a steel specimen and measured the coefficient of friction of about 0.1 when the load was 200-500 g. When the adhesive μ_{adh} friction is low, as in the case of scratch tests with a diamond indenter, the measured friction is caused mainly by grooving. Zum Gahr [2] defined the friction in grooving wear μ_g as:

$$\mu_g = \frac{4}{5\pi K_{CA}} \frac{F_N sin\alpha_a}{R^2 H_{def}} \tag{2.37}$$

where R is the tip radius and K_{CA} is a factor of crystal anisotropy. The value of K_{CA} is about 5 for cubic metals, but depends on crystal orientation.

Another factor influencing the friction is how the abrasive is supported. Misra and Finnie [119] measured a friction coefficient of 0.25 in three body abrasion, which was half of the value 0.5 obtained in two-body abrasion tests. They suggested that the difference in μ is due to the rolling and sliding of the abrasive particles even at high loads. The deformation of the wearing surface affects the friction coefficient. Pintaude et al. [120] measured the friction in pin abrasion tests with selected steels and concluded that the friction coefficient increases with the increase of the hardness ratio H_{def}/H_0, where H_{def} and H_0 are the hardness of the deformed surface and the initial hardness of the material, respectively. Deeper penetration of the abrasive generally increases the frictional forces. Sinha and Sahay [121] measured the cutting forces with a single abrasive grain and found that the normal force was close to constant with varying cross-sections of the groove and varying thickness of the chip, whereas

the tangential force varied linearly with the cross section of the chip.

2.4.7.1 Friction and wear

Avient et al. [106] showed that wear W_{ab} is proportional to the normal force F_N and the coefficient of friction μ, i.e.,

$$W_{ab} \simeq cF_N(\mu - \mu_0) \tag{2.38}$$

where μ_0 is the coefficient of friction at zero wear and c is a constant. Goddard [122] continued the tests with non-metallic materials and found that the linear relation between friction and wear is not applicable due to fracturing of the minerals at and near the sides of the grooves.

The wear equations do not contain the area of contact as a factor. The change of the area of contact is shown to rebalance equation 2.18, when the tangential force is changed in the sliding situation. Therefore in adhesion and abrasion the friction component should show a relationhip to the area of contact. However, Mulhearn and Samuels [123] explained that when the surface area increases, the number of contacts increases proportionally, and the load per contact point decreases by the same ratio. They also found that the area of contact between the materials and the scratch head was the same in both cutting and ploughing, when the height of the prow in ploughing and the contact length of the chip in cutting was included.

Xie and Williams [124] developed a micro-cutting model to predict the value of μ and the specific wear rate W_K, when a surface is sliding against a rough harder surface:

$$\mu = \left(\frac{2}{\pi}\right)^{0.5} \frac{tan\alpha_a}{l^{0.25}} \left(1 + \mu_f \left(1 + \frac{\pi}{4tan^2\alpha_a}\right)^{0.5}\right) \tag{2.39}$$

$$W_K = 0.003 \frac{tan^3\alpha_a}{\mu_f \tau_f l^{0.5}} \left(\frac{H}{H_{def}}\right)^{0.5} \tag{2.40}$$

where α_a is the attack angle of the hard asperity $\alpha_a < 60$ °, l is the dimensionless distance between adjacent wear tracks describing the relative overlap of successive scratches, H_{def} is the hardness of the deformed surface, H is the hardness of the bulk material, τ_f is the shear flow stress, and μ_f is the interfacial coefficient of friction between the soft material and a hard asperity. Cutting can occur at low attack angles below 10°, when the right conditions are met, such as in side wall stripping [62, 64]. Torrance [125] mentionend that cutting at a low attack angle is possible at low μ_f and l values.

2.4.8 Abrasion work

In principle, the amount of work can be determined from the abrasion test, when the tangential force history is known with the given length of abrasive path. This work includes the amount of work done in the sliding contact as well as the work done for the deformation of the surfaces. Separation of these components can be difficult from the wear test measurements. The wear specific portion of work that actually removes material can also be

quite low. However, Kallas [126] suggested that the specific wear energy correlates with the relative wear resistance and also with the static and dynamic indentations.
Beckmann [127] proposed that the wear volume is proportional to the work done by the shear forces in the surface region. Equation 2.41 shows that the amount of wear depends on the shear stress τ, the energy density transferred to the wearing body e_s^*, the real A and apparent A_{ap} area of contact A, and the sliding path L. e_s^* is characteristic of the material and can be obtained from the amount of shear work conducted to remove a unit volume of material.

$$W_V = \frac{\tau}{e_s^*} \frac{AL}{A_{ap}} \tag{2.41}$$

Larsen-Badse [128] suggested that the wear resistance could be measured as the energy required to remove a unit volume of material. The abrasion wear resistance is affected by the stress-strain behavior of the specimen material, and the microstructure such as fine carbide spacing [129]. Their studies suggested that only about 17-18.6 % of the cutting work was directly involved in the chip formation, when the coefficient of friction was 0.65. The energy of grinding was also investigated by Malkin and Joseph [130]. They ended up in a direct relationship between the grinding energy and melting energy of the material. Malkin and Joseph also reported that 75 % of the work went to chip formation and 25 % to friction.

The linear work in sliding can be defined as $W_{work} = F_T L$, where the work is conducted by the tangential force. The coefficient of friction of the test can be used to determine the tangential force $F_T = F_N \mu$. Combining these two equations gives

$$F_N = \frac{F_t}{\mu} = \frac{W_{work}}{\mu L} \tag{2.42}$$

Equation 2.43 shows one form of the Archard's Equation 2.20, where the normal force is substituted with Equation 2.42:

$$\frac{W_V}{L} = K \frac{F_N}{H} = K \frac{W_{work}}{\mu H L} \tag{2.43}$$

When L, representing the unit sliding distance of wear, and work are equal on both sides, the relation of work and wear becomes:

$$\frac{W_V}{W_{work}} = K \frac{1}{\mu H_{def}} \tag{2.44}$$

Equation 2.44 shows that the ratio of wear and work is inversely related to the coefficient of friction and hardness of the surface. In the case of high stress abrasion, the deformed surface hardness H_{def} should give a better approximation for the ratio of wear and work in the steady state wear condition.

2.4.9 Comparison of the high stress and gouging abrasion test

The abrasion wear test configuration can affect the relative wear resistance of the materials, if the dominating wear mechanism changes. Gore and Gates [131] conducted low stress rubber wheel and high stress steel wheel abrasion tests with dual phase materials and concluded that the carbides lower the friction between the steels and the abrasives. This changed the behavior of the abrasive from rolling toward sliding on the steel specimen, which also increased the velocity of the particles and the extent of crushing of the particles. These factors

resulted in a decrease of the wear resistance with increasing hardness, which was opposite to the results of the rubber wheel abrasion tests. Dube and Hutchings [132] also concluded that the extent of fracture of the abrasive particles should be taken into account when interpreting the results of rubber or steel wheel abrasion tests. Ala-Kleme et al. [133] compared the wear resistance of metal matrix composites when tested with the rubber wheel abrasion tester and a laboratory-size cone crusher. They concluded that the different ranking order of the MMC materials was due to the different abrasive size used in the tests. The smaller size of sand used in the RWAT resulted in the wear of the matrix, whereas with the cone crusher the reinforcing particles were able to protect the matrix from the larger sized abrasives. Ala-Kleme et al. [133] concluded that the size of the abrasive is important in the material tests conducted for rock crushing applications.

Hawk et al. [134] compared the test results of several wear test equipment, including the jaw crusher test. They concluded that in the jaw crusher test hardness improves the wear resistance of materials with hardness lower than 250 HB. The results obtained from the jaw crusher tests are markedly different from the other test equipment, where the effect of hardness on the wear resistance is linearly increasing even with materials of high hardness. Tylczak et al. [135] compared the laboratory test results to the results from field experiments and found a similar order of results when the wear mechanisms were similar. They concluded that the laboratory tests can provide a good measure of the relative wear resistance if the test is selected according to the field wear test.

3 Design of the dual pivoted jaw crusher

The design of the dual pivoted jaw crusher was based on the idea of controlling as many variables in the test as possible. Movement of the jaws and geometry of the jaws were among the most important of them. In a common single toggle jaw crusher, the angle and the movement of the jaws is varying depending on the location of the jaw plate and which part of the crushing cycle is considered. Figure 3.1 shows an overall picture of the dual pivoted jaw crusher.

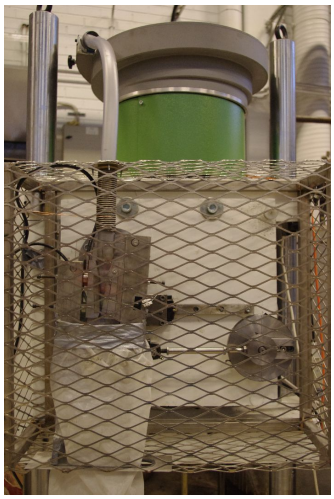

Figure 3.1: *The dual pivoted jaw crusher with a vibrating bowl feeder at the top, a flywheel on the right, and a collection system at the bottom of the picture. A tube is used to feed single stones into the crusher. The moving parts of the equipment are all inside a cage for personnel protection.*

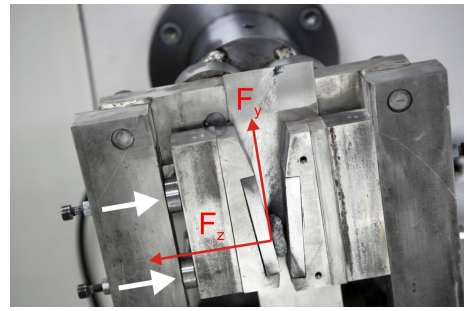

Figure 3.2: *The crushing cavity of the DPJC without the front sideplate. The arrows show the location of the force sensors under the specimen holder and the directions of the measured forces Fz and Fy.*

3.1 Operational systems

The test equipment contains the following elements:

- Jaw frame assembly
- Motor with gearbox and flywheel
- Feeding system
- Collection system
- Measurement system

3.1.1 Jaw frame assembly

The dual pivoted jaw crusher (DPJC) is different from other jaw crusher designs in the uniform throw of the jaws throughout the jaw surfaces. Two pivot points of the jaw crusher are located in each jaw, hence the term "dual pivoted". Figure 3.3 shows the schematic of the DPJC with two different test settings. The left and right hand sides of the jaw assembly are named as "Jaw1" and "Jaw2", respectively. Each side consists of a rigid jaw frame, which is connected to two axles from both ends. The axles are diagonally connected to upper and lower circular supports. The circular supports are locked to prevent their rotation when the equipment is in operation, but to enable their rotation when their clamps are loosened. When the circular support is rotated, the tilt angle β of the diagonal direction of the axles is changed relative to the vertical direction. The axle tilt angle β can be freely selected and locked into place by tightening the circular supports. When the angle between the axles is the same in both upper and lower circular supports, the jaw frames of both sides are parallel to each other at all times.

The upper circular support is fixed in place against the backing steel plate, which supports also the flywheel and the electric motor. The lower circular support is fixed to the backing plate with an assembly of horizontal and vertical linear bearings. This allows the swinging motion of the lower circular support and prevents the rotation of the support and the movement of the support in the direction normal to the image plane in Figure 3.3. A shaft connects the lower circular support to the flywheel that is rotated with an electric motor, causing the rocking motion of the jaw frames when the flywheel is turned. This rocking motion causes the jaw frames to change the swing angle α from the vertical start position. The length of the shaft and the connection point of the shaft and the flywheel can be changed to set the length of the swing. As the jaw frames are parallel, the opening angle of the jaws is controlled only by the angles of the rectangular specimens in the specimen holders, which hold the test specimens at certain angles from the jaw frame.

The mechanism allows variable ways to set up the movement and the geometry of the gap between the jaws. The main variables are the axle tilt angle β, which defines the starting position of the crushing cycle, the swing angle α, which defines the throw of the crushing cycle, and the set minimum distance d_{min} (gap) between the jaws. The axle tilt angle β can be changed either by changing the angle of the axles, or by changing the length of the shaft between the lower circular support and the flywheel. The swing angle α is controlled by setting the distance of the connection point of the shaft from the center of the flywheel. The minimum gap d_{min} is set by adding backing plates between the jaw frame and the specimen holders of both jaws, and can also be adjusted with the length of the shaft. Figure 3.2 displays the crushing cavity of the DPJC when axle tilt angle $\beta = 90°$.

3.1.1.1 Specimen holders and placement of the force sensors

The opening angle of the jaws is an important factor in the jaw geometry. As the jaw frames are constantly parallel, the desired angle is achieved by specimen holders, which tilt the specimen to a certain angle. Both jaws can accept tilted specimen holders restricted only by the distance between the jaw frames that is affected by the angle β. Figure 3.4 shows the cross-section of the Jaw1 specimen holder that tilts the specimen 5° from vertical. The specimen holder is tightened into the jaw frame with two 12.9 grade M6 steel screws with tension of 15 kN in each screw. The pretension is required because of the force sensors that are located between the specimen holder and the jaw frame. In addition, there is also a filler block that is used to set a desired minimum gap between the jaws. The jaw frames contain multiple screw holes to change the vertical position of the specimen holder. This is

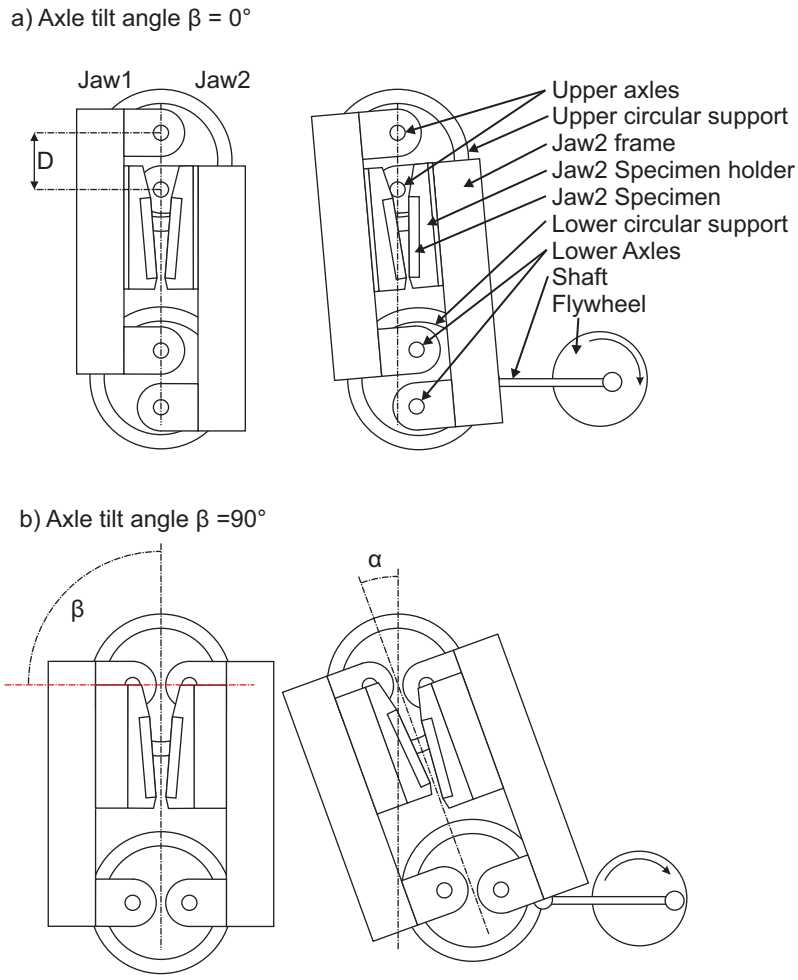

Figure 3.3: *a) Schematic of the jaw frame with angle $\beta = 0°$ between the axles and the jaw frame, and b)the circular supports and axles rotated* 90° *from the vertical.*

required as the jaw frames are displaced when β is changed. The current configuration has possibilities to set the specimen holders to the same level when $\beta = 0°$, 15°, 30°, 45°, 60°, 75°, and 90°.

Figure 3.4 shows the XYZ coordinate system that is set according to the force sensor directions in the Jaw1 jaw frame. Z-direction is always normal to the jaw frames, Y-direction parallel to the vertical face of the jaw frame, and X-direction perpendicular to both Z and Y directions. The Kistler 9601A VarioComp piezoelectric force sensor measures the X and Y axis forces up to 2.5 kN. The force measurement range for the Z axis is 10 kN with a 15 kN pre-tension load. The pre-tension prevents slipping of the sensor on the counterfaces and provides accurate readings in the X and Y directions. The rectangular 75 mm x 25 mm x 10 mm specimen plate is held in place by two screws going through the lower end of the specimen holder.

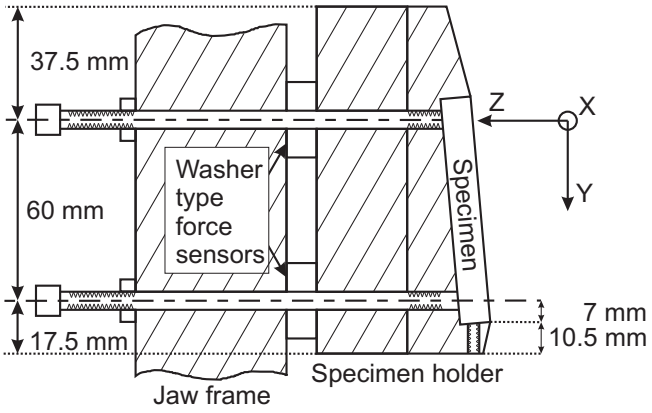

Figure 3.4: *A schematic illustration of the attachment of the force sensor and the specimen holder with two screws holding a 15 kN pretension each. Two smaller screws going through the bottom of the specimen holder keep the specimen in place during the test.*

3.1.2 Feeding system

A vibrating bowl feeder with a 400 mm inner diameter at the base of the bowl feeds the stones into the crusher. The bowl feeder raises the stones from the bowl in a spiral path and drops them to the feeding tube one stone at a time. A hopper can be used to feed the vibrating bowl, but the 4 kg batches of stones used in the current tests did not need the hopper. The feed rate of the rock can be controlled with the amplitude setting of the hopper. The feed rate was set to the highest possible where the stones did not jam into the feeding tube or choke the jaw. The test was run at the maximum capacity that depended on the geometry and settings. The vibrating bowl feeder drops smaller rocks first and largest rocks last from a rock batch of wider size distribution. This means that growing rock size decreases the capacity, as it generally takes a longer time to crush larger rocks. After the rock falls from the bowl feeder, it continues to fall in the feeding tube of 25 mm in diameter. The tube guides the rock to fall between the jaws. A light port system was built into the tube using Infrared LEDs and IR photo-detectors. The port system was used to measure the number and frequency of passing rocks.

3.1.3 Collection system

After the rock particles are crushed to a size small enough to pass the release end of the jaw crusher, they continue to fall into the collection bin. The crushing cavity and the collection bin are closed with a plastic cover to prevent airborne transfer of dust and rock particles. The collection bin also contains an air intake that creates a lower pressure in the collection bin. This causes air to flow into the system from the feed end preventing dust from escaping. The finest airborne particles travel through the intake and larger particles fall to the bottom of the collection bin. The wear debris was collected with a detachable magnet that was placed on the lower pivot axle of Jaw1. Only the axles of the frames were ferromagnetic, as the jaw frames and the specimen holders were made from austenitic stainless steel, which prevented the collection of unwanted metallic debris from the holders.

3.1.4 Electric motor with gearbox and flywheel

A 1.5 kW electric motor and a connecting gearbox with a 90° angle are positioned behind the backing plate. The axle from the gearbox goes through the plate and connects to the flywheel positioned on the same side of the backing plate as the jaw frame assembly. When the motor is run by 50 Hz AC current, the flywheel rotates at a speed of 217 rpm, which is also the number of crushing cycles per minute. The speed of the equipment can be freely adjusted from 40 rpm to 430 rpm. The angular momentum needed to crush rocks of 10 mm in diameter is low at the point of the flywheel of 160 mm in diameter, as single rocks can be crushed by turning the flywheel by hand.

3.1.5 Measurement system

During the tests, the compressive and sliding forces are measured with two washer type Kistler 9601A VarioComp piezoelectric force sensors. The sensor placement is shown in Figures 3.2 and 3.4. The sensors are capable of measuring loads of 25 kN in the Z-direction, and 2.5 kN in the X- and Y- directions. The F_z and F_y channels of the force sensors were connected to a Kistler Type 5073 four channel charge amplifier. The factory calibration values were used in the charge amplifier settings for the tests. The Z-direction calibration of the sensors was tested with Instron® 5967 screw driven uniaxial load tester, and the Y-direction calibration was tested in place in the jaw crusher by loading with free weights. Both factory calibration values proved satisfactory with less than 5 % deviation from the known load. Various sensors were used to detect the displacement of the jaw. As the rocking motion is quite large in the β=90° tilt, the angular displacement of the jaw frame was measured from Jaw2 upper axle with Joral HP38 magnetic angle sensor, which gives 0-5 V signal when rotated from 0° to 360°. The approximate angle of rotation was 20°. This sensor gave a good signal for large rotations, but for smaller rotations it proved to be too inaccurate. For the β=45° tilt, a similar Joral HP38 sensor was used with 0-5 V signal when rotated from 0° to 45°. This change increased the signal sensitivity from 1V/75° to 1V/9°. An extensometer was used for the β=0° tilt, as it could measure the exact displacement of the jaws in the Z-direction more precisely. The extensometer was not used for other tests because of the Y-displacement of the jaw frames. When the jaws compress rocks between them, the load causes elastic deformation of the axles that are supporting the jaws. This elastic deformation can be seen with the extensometer, which is measuring the direct displacement of the jaw frames. When the angle sensor is measuring the rotation of the axle, the elastic deformation of the axles is not shown in the angle sensor measurements. The analog signal from the sensors was measured with two Tie Pie Handyscope HS4diff oscilloscopes, which were connected to a computer. The four channel oscilloscopes were synchronized to the same clock, giving a total of 8 measuring channels. The measurements were recorded with Tie Pie's own software. The test was recorded at a 12 bit resolution and a recording rate of 5000 Hz. The measurement file size was set to 4 000 000 measurements, corresponding to 800 seconds, or to 8 000 000 measurements, corresponding to 1600 seconds for tests requiring extended time. The measured files were processed with Matlab® software.

3.2 Movement of the dual pivoted jaw crusher

The movement of the jaw frames is controlled by the fixed 60 mm distance D between the axles in both upper and lower circular supports. In Figure 3.3 a) with $\beta = 0°$ the line D is vertical and parallel to the jaw frames, and the Jaw1 jaw frame is 60 mm higher than the right jaw frame. The maximum gap between the jaws is reached when the jaw frames are

vertically aligned. The gap between the jaw frames closes rapidly when the swing angle α is increased. Figure 3.5 shows the relation of the compressive displacement to the lateral or sliding displacement between the jaw frames when the swing angle α is 10°. There is about 10 times more compressive motion than sliding motion, when β is close to 0°. When $\beta =$ 90°, the sliding motion is now dominant and the compressive displacement is small. The compressive movement relation to the sliding movement increases with increasing β. One quarter circle with a radius D describes how the gap between the jaws is closing or opening from $\beta = 0°$ to $\beta = 90°$. The compressive position d_Z and the lateral position d_Y of the jaw frames can be calculated during the tests with Equations (3.1) and (3.2), where D and β stay constant and the swing angle α is detected with magnetic angle sensors.

$$d_z = D(sin(\alpha + \beta) - sin(\beta) \tag{3.1}$$

$$d_y = D(cos(\alpha + \beta) - cos(\beta) \tag{3.2}$$

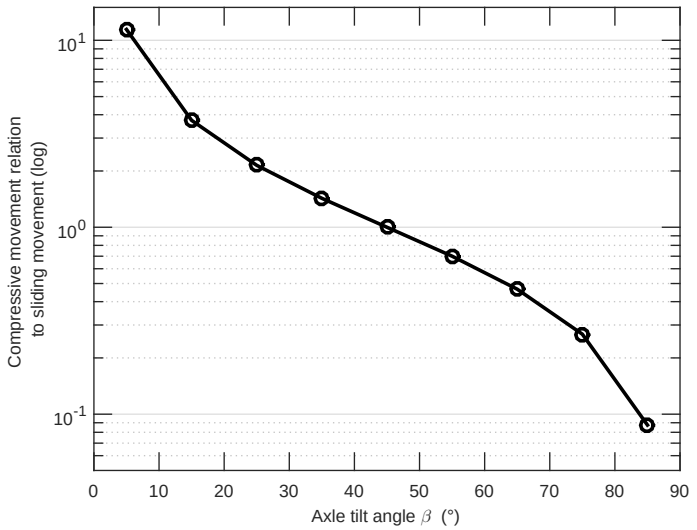

Figure 3.5: *Illustration of the change in the ratio between compressive and sliding displacement. The marker at $\beta = 5°$ shows a 10° swing from $\beta = 0°$, and $\beta = 85°$ shows the 10° swing from $\beta = 90°$.*

3.2.1 Movement of the Jaw1 and Jaw2 specimen surfaces

The simplest way to visualize the movement between the specimen surfaces is to keep Jaw2 stationary and move Jaw1 relative to Jaw2. Figure 3.6 shows three situations, where the specimen in Jaw2 is kept in place and Jaw1 is moved to produce the compression cycle when β=90°. The three illustrated jaw openings were also used in the tests. The jaw opening angle is the same 10° in a) and c), but the set angle of the specimen holders is different. In a), both specimens are tilted 5° from vertical, whereas in c) only the specimen in Jaw1 is tilted 10°. In e), both specimens are tilted 12.5° from vertical for a total opening angle of 25°. Figures 3.6 b), d), and f) show the jaw configuration after the compression cycle, where

the minimum gap is the same in all configurations. The 10 mm sphere illustrates the lowest position in the jaws, where a round 10 mm rock particle can fit if it is not crushed during the crushing cycle. The intact rock particle is moved about 30 mm along the specimen surface of Jaw2 in each of the three cases. However, the rock is displaced along the specimen surface of Jaw1 for a total displacement of 9.7 mm, 12.5 mm and 1.7 mm when changing from a) to b), c) to d), and e) to f), respectively. The differences in the movement of the rock particle are caused by the tilt of the specimen in Jaw2. As the Jaw1 specimen approaches Jaw2 with a circular path having a radius of 60 mm, the lowest end of the specimen moves vertically higher than the lowest point of the specimen in Jaw2. When compared to an untilted specimen, a tilted specimen in Jaw2 increases the gap between the specimens the farther the Jaw1 specimen is moved towards the Y-direction, and needs to be moved even further to reach the same minimum gap when the specimen in Jaw2 is not tilted.

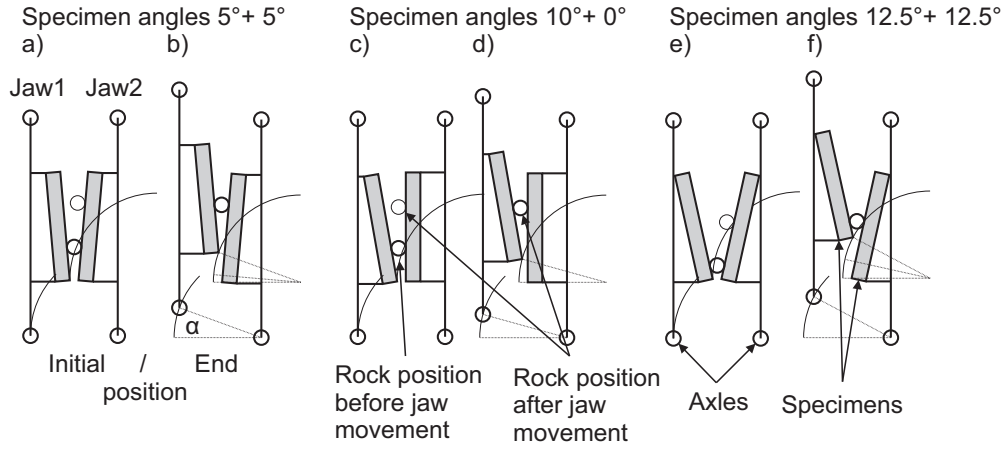

Figure 3.6: *Illustration of the effect of the specimen angle of Jaw2 on the sliding displacement of the jaws, when Jaw1 is swang from a) to b), or c) to d), or from e) to f) to have the same amount of compressive displacement in each case.*

Figure 3.7 a) illustrates the test geometry with β=90° tilt, where only the specimen in Jaw1 is tilted by 20°, and b) shows a test geometry where both jaws are tilted by 10°. The throw of 3 mm is produced with a longer path in b) because of the tilted specimen surface in Jaw2, showing longer ΔZ and ΔY displacements than in a). Figure 3.7 c) shows the situation b) when the coordinates are changed to Y_2 and Z_2 that are parallel and normal to the specimen surface in Jaw2, as also in Figure 3.7 a). The displacement ΔY_2 is now parallel to the specimen surface in Jaw2, and ΔZ_2 is normal to the specimen surface. The directions of the coordinates are also changed to describe the compression and sliding of rock particles against the specimen in Jaw2. The curved approach line of the Jaw1 specimen shows that the gap between the jaws widens until the tangent of the curve is parallel to the specimen surface in Jaw2. This means that the specimen in Jaw1 has to rotate 10° before compressive movement is actually conducted. After the initial rotation of 10° to compensate for the tilt of the specimen in Jaw2, the approach geometry becomes almost identical to the case where only the specimen in Jaw1 is tilted 20° from the Y-direction. The main differences are the opening of the gap until the specimen tilt angle is met, and as the compression cycle ends to the same minimum gap, the actual compressive displacement ΔZ_3 is slightly longer

than ΔZ_2 and its sliding component ΔY_3 shorter than ΔY_2. When the specimen in Jaw2 is parallel to the jaw frames, the ΔZ and ΔY displacements follow the coordinates of the force sensors. The displacements ΔZ and ΔY can be calculated using equations (3.3) and (3.4) :

$$\Delta Z = d_{Z2} - d_{Z1} = D(sin(\alpha_2 + \beta) - sin(\alpha_1 + \beta)) \tag{3.3}$$

$$\Delta Y = d_{Y2} - d_{Y1} = D(cos(\alpha^2 + \beta) - cos(\alpha_1 + \beta)) \tag{3.4}$$

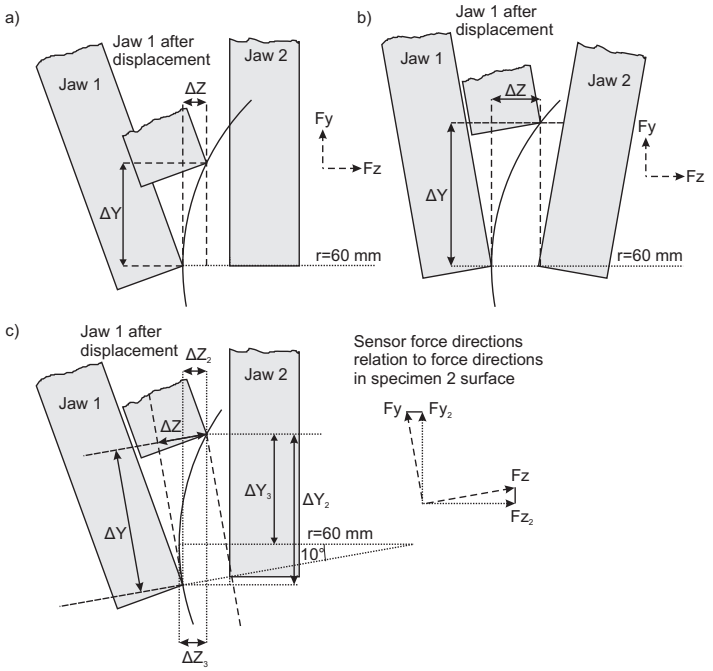

Figure 3.7: *The compressive cycle with the $\beta = 90°$ tilt, showing situations where a) Jaw2 specimen is parallel to the jaw frames, b) Jaw2 specimen is tilted 10° from the jaw frames, c) coordinate system is tilted to show situation b) where the Jaw2 specimen is parallel to displacement ΔY_2*

Equations (3.5) and (3.6) show the relation of ΔZ_2 and ΔY_2 to ΔZ and ΔY.

$$\Delta Z_2 = (\Delta Z - \Delta Y tan(Jaw2angle))\, cos(Jaw2angle) \tag{3.5}$$

$$\Delta Y_2 = \frac{\Delta Y}{cos(Jaw2angle)} + sin(Jaw2angle)\,(\Delta Z - \Delta Y tan(Jaw2angle)) \tag{3.6}$$

Finally, ΔZ_3 and ΔY_3 are:

$$\Delta Z_3 = \Delta Y_2 - Dsin(Jaw2angle) \tag{3.7}$$

$$\Delta Y_3 = \Delta Z_2 + D - Dcos(Jaw2angle) \tag{3.8}$$

4 Materials and methods

This chapter introduces the materials and wear testing methods used in this study. Results were also obtained by examining the worn specimens and the wear debris, and by measuring the comminution of the rock in the tests.

4.1 Materials

In this study, nine steels of varying chemical compositions and manufacturing methods were used as specimen materials. Table 4.1 shows the chemical composition, bulk hardness (HV), and density of the test materials. The S355 K2 G3 steel was supplied by Ruukki Metals (part of SSAB since 2014). The specimens were cut from a 10 mm thick plate, and the wear test surface was ground with P120 grit paper to remove the decarburized layer. CSA G40.21 100 QT (QT100) is a Canadian quench and tempered structural steel (ASTM A 514 Grade B rolled structural steel). These softer steels were used primarily as reference materials. The harder tool steels were powder metallurgically manufactured steels. Ralloy® WR6 and WR12 are commercial tool steels from Metso Minerals. WR6 steel was manufactured with both Hot Isostatic Pressing (HIP) and Spray Forming (SF), and are named as WR6H and WR6SF, respectively. WR12 steel was manufactured with HIP. WI5, WI7, WI8 are spray formed experimental high chromium steels from Metso Minerals, which are also referred to as tool steels in this thesis. XT710 is an austenitic high manganese steel from Metso minerals and has a good deformation hardening capability. The QT100, WR6, WR12, WI5, WI7, WI8 specimens for the DPJC tests were water jet cut from the ASTM-G81 jaw crusher test specimens, which were cut from larger ingots. The specimens of XT710, which is a commercial manganese steel from Metso Minerals, were cut from the liner plates of a commercial jaw crusher.

4.1.1 Microstructure of the tool steels

All tool steels had a tempered martensitic matrix. The tempering process used secondary hardening to lower the amount of retained austenite and to precipitate smaller carbides. The carbide content, type and size of the tool steels are different. Figure 4.1 shows the carbide microstructure of the high chromium steels WI5, WI7 and WI8. The chemical composition of the WI series produces a $(Fe, Cr)_7C_3$ carbide structure based on the Fe-Cr-C ternary equilibrium diagram [136]. The chromium carbides are elongated in all WI steels. The carbide volume fraction was measured from the optical microscope images taken with a 50x objective lens. The size and shape of the particles were measured using ImageJ software, and the results are shown in Table 4.2. The carbide content volume fraction of the WI steels varied from 27 % to 45 % , which were higher than the carbide contents of the WR steels. The size and shape analyses were performed from the direction where the carbides of the WI steels show an elongated shape. In all WI steels the carbides have approximately the same aspect ratio, with the difference that the amount of carbides varied between WI7 and WI8. WI5 had the largest carbides with the highest volume fraction of all steels used in the tests.
Figures 4.2 a) and b) show the round carbides of the spray formed WR6 Ralloy® tool steel, which are characteristic to all WR tool steels. Figures 4.2 c) and d) show the smaller

Table 4.1: *Chemical composition, hardness and density of the test materials. The compositions for S355, QT100 and WR6 are nominal compositions, while for WR12, WI5, WI7, WI8 and XT710 the compositions were measured with an optical emission spectrometer at Metso Minerals.*

Element (Wt. %)	S355 K2G3	QT100 CSA G40.21	WR6 Ralloy®	WR12 Ralloy®	WI5	WI7	WI8	XT710
C	<0.18	<0.2	2.9	1.1	3.98	2.5	3.28	1.24
Si	<0.5	0.45	<1.0	1.1	1.01	1.04	1.02	0.57
Mn	<1.6	1.5	<1.0	0.3	0.93	0.99	0.98	16.4
P	<0.025	0.03	<0.03	0.019	0.026	0.028	0.028	0.042
S	<0.02	0.015	<0.03	0.008	0.013	0.008	0.008	0.005
Cr	0	0.2	5.25	7.6	19.8	19.2	19	2.44
Ni	0	0	0	0.17	0.1	0.1	0.1	0.26
V	0	0	<11.5	2.4	0.1	0.093	0.09	0
Mo	0	0.2	1.3	1.8	0.62	0.57	0.56	0.04
B	0	0.003	0	0.0014	0	0	0	0
W	0	0	0	1.2	0	0	0	0
Nb	0	0	0	0	0.006	0.008	0.036	0
Hardness (HV)	190	280	620	687	781	750	743	240
Density (g/cm^3)	7.81	7.73	7.34	7.70	7.44	7.45	7.44	7.77

carbide size of the HIP conditioned WR6 steel and the WR12 tool steel, respectively. The measured vanadium carbide volume fraction of WR6 tool steels was similar in the SF and HIP conditions. WR12 steel contains both VC or WC and chromium carbides. In optical images the chromium carbides usually show as lighter color than the matrix, whereas the vanadium carbides and tungsten carbides show darker than the matrix. The measured total volume fraction of the VC and WC carbides in the WR12 steel was 12 %, while the chromium carbide fraction was 3 %. The spray formed WR6SF had the largest carbides of the WR series. In WR6H and WR12, the size and shape of the carbides were similar and much smaller than in the other studied tool steels.

Table 4.2: *Average size and shape of the carbides.*

Tool steel	Area (μm^2)	Major axis (μm)	Minor Axis (μm)	Aspect ratio	Volume fraction (%)
WR6H	0.66±0.40	1.07±0.32	0.73±0.22	1.48±0.33	25.11±0.90
WR6SF	25.36±16.80	6.04±2.24	4.74±1.78	1.30±0.23	22.74±1.17
WR12	0.73±0.44	1.08±0.35	0.79±0.25	1.37±0.24	14.80±0.78
WI5	33.81±34.73	8.81±5.96	4.20±1.65	2.04±0.92	45.49±0.98
WI7	11.97±12.11	5.17±3.50	2.56±0.84	1.95±0.83	27.26±0.12
WI8	12.80±10.41	5.57±3.26	2.60±0.88	2.10±0.97	35.29±0.26

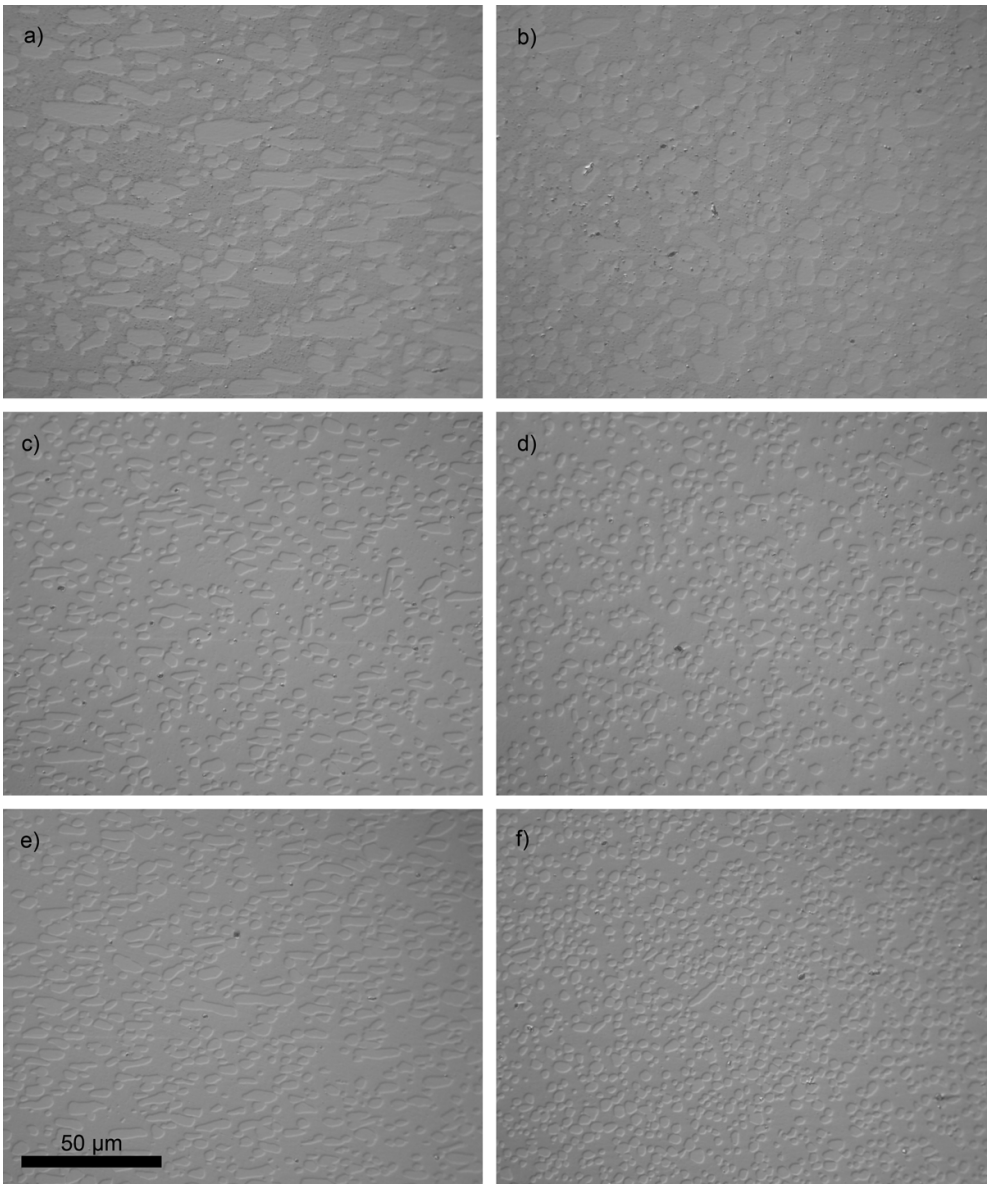

Figure 4.1: *Comparison of the carbide size and shape of the high chromium steels. a) WI5 , b) WI5 in the transverse direction, c) WI7, d) WI7 in the transverse direction, e) WI8, f) WI8 in the transverse direction.*

4.1.2 Abrasives and their properties

The G81-97 tests at NRC were conducted with a local morainal rock from Vancouver, Canada. The rocks used in the DPJC tests were quarried from Finland. Granite and gneiss were quarried from Sorila and Lakalaiva in Tampere, tonalite from Koskenkylä quarry and quartzite from Nilsiä. Table 4.3 shows the mineral composition of the rocks [137]. The UCS values of the rocks were obtained from Metso Minerals, and the composition of quartzite

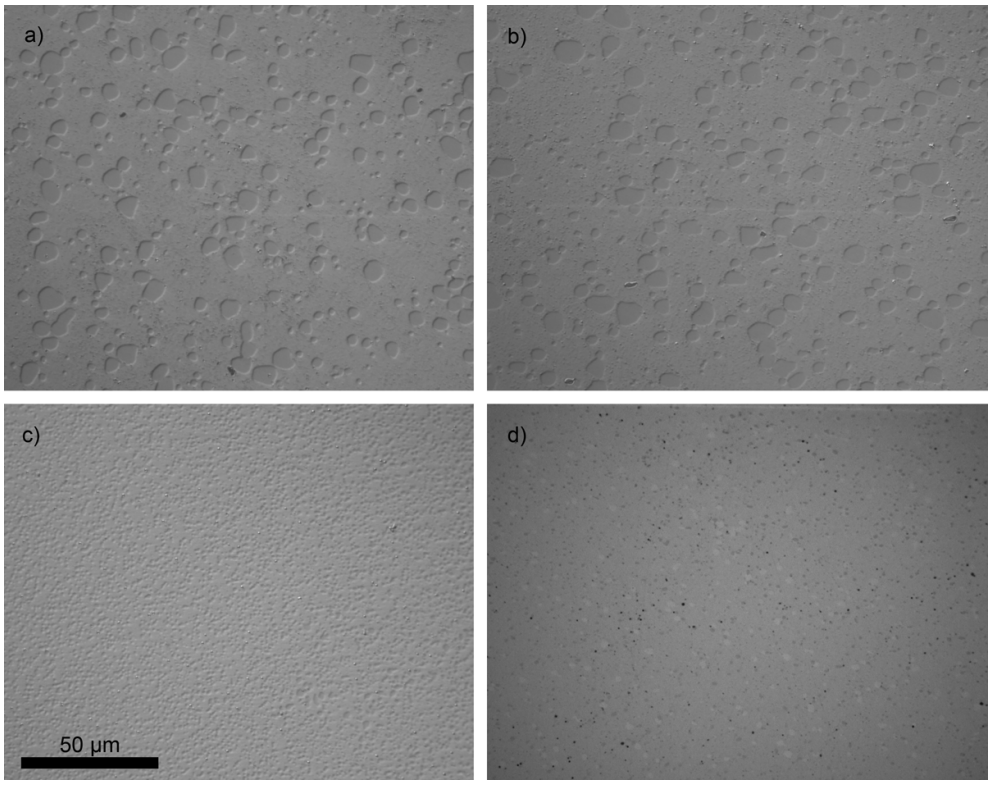

Figure 4.2: *Comparison of carbide size and shape of Ralloy® WR tool steels. WR6 a) in spray formed condition b) transverse direction, c) in HIP condition, d) WR12 in HIP condition.*

from Sibelco Europe.
Koskenkylä tonalite is a granodiorite and has a high mechanical strength due to the fine grain size, high strength of the minerals, and strong bonds between the minerals. Sorila granite has a coarser grain size and it contains quartz grains in groups with a size of 1-2 mm. These groups are surrounded by a finer mineral structure. The strong bonds add strength but the diversity of grain sizes weakens the structure [137]. Lakalaiva gneiss is metamorphic in structure, and its high biotite content is usually located in thin strips between the quartz and plagioclase grains. The high amount of biotite also weakens the microstructure, which on the other hand is compensated by the small grain size [137]. Nilsiä quartzite has high quartz content with small amounts of sericite and kaolinite minerals.

4.2 Test methods

The laboratory-size single-toggle jaw crusher tests according to the ASTM G81-97a standard were conducted at the University of British Columbia in Vancouver in collaboration with the Mining Materials Wear and Corrosion Program of the National Research Council (NRC) Canada. The DPJC tests were conducted at the Tampere Wear Center (TWC) laboratory of Tampere University of Technology. The room temperature of the TWC laboratory was 22 ± 2 $^{\circ}C$ and the measured relative moisture varied from 17 % during winter up to 70 %

Table 4.3: *Mineral composition of the rocks [137].*

	Granite	Tonalite	Gneiss	Quartzite
Quarry	Sorila	Koskenkylä	Lakalaiva	Nilsiä
Plagioclase	45 %	40 %	36 %	
Quartz	25 %	40 %	24 %	92-98 %
Feldspar	15 %		7 %	
Biotite	10 %	17 %	25 %	
Sericite				2-8 %
Kaolinite				0-5 %
Hornblende	5 %	3 %	5 %	
Granate			3 %	
Average grain size (mm)	0.7	0.3	0.3	
UCS (MPa)	193.9	308.4	63.7	
Bond w_i	16.0	15.6	13.9	
L.A. index	17.2	11.7	20.0	
Density (g/cm^3)	2.62	2.69	2.63	2.65

during summer.

4.2.1 ASTM G 81-97a Jaw Crusher test

The single-toggle jaw crusher was slightly modified according to the G81-97a standard. The corrugated jaw plates used normally in the jaw crusher were removed and specimen holders were used in place of the standard jaw plates. These specimen holders could hold two specimen plates in both jaws. The dimensions of the specimen plates in the ASTM G 81-97a tests are presented in Figure 4.3. The red rectangles show the locations from where the three DPJC specimens were cut from the stationary jaw specimen. The three wear surface sides, (1), (2) and (3), were saved for the cross-sectional examinations.
The test configuration used QT100 steel as a reference material, and the specimen plate set-up was as described in Table 2.3. The tests were conducted according to the ASTM G 81-97a standard [1]. The specimens were weighed before and after the test, and the volume loss of the specimen was compared to the volume loss of each reference sample using Equation (4.1):

$$W_R = \frac{\frac{X_s}{R_s} + \frac{X_m}{R_m}}{2} \tag{4.1}$$

where W_R is the wear ratio, X_s is the volume loss of the stationary specimen plate, R_s is the volume loss of the stationary reference plate, X_m is the volume loss of the moving specimen plate, and R_m is the volume loss of the moving reference plate. The wear ratio should be one when the reference plates are used as specimens, and it will decrease with increasing wear resistance of the specimen material.

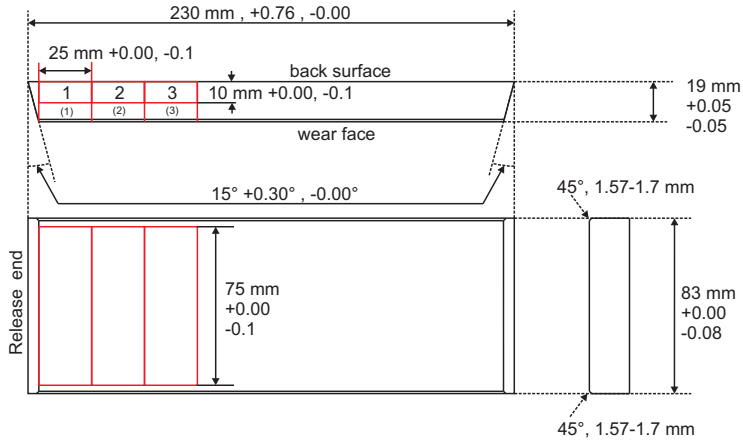

Figure 4.3: *A schematic of an ASTM G81-97a specimen plate. The red rectangles are the locations from where the three DPJC specimens 1,2 and 3 were cut.*

The main controlled variables of the ASTM G81-97a test are:

- 907 kg (2000 lbs) of morainal rock with approximate size of 25 mm in diameter was crushed in each test. The batch of rock was kept outside, and thus the rock was wet during the test.
- The jaw crusher was choke fed. Thus, the jaw crusher was fed to be approximately half full of rock during the test.
- Minimum gap was set to 3.2 mm. The gap was checked and corrected after 227 kg (500 lbs) of rock was crushed.
- Before the test series a reference pair was tested to check if the wear ratio of the specimen was close to unity.

Figure 4.4 shows the size difference of the morainal rock before and after crushing. As the feed and the product were not sieved, the images were used to estimate the sizes of the particles. The length of both the shortest and longest dimension of the particles was measured 50 times from the feed and from the product images. Only the largest particles of the product were used for the measurement. The longest dimensions of the feed and the product were on average 24.2 $\pm$10.2 mm and 12.0$\pm$4.3 mm, while the shortest dimensions were in average 14.9$\pm$6.3 mm 7.0$\pm$2.8 mm (St.Dev. 2σ). If the largest particles are used as a representative for the P_{80} value, the overall reduction ratio RR of the crusher can be approximated to be 2:1. However, the determination of the reduction ratio from the image analysis can overestimate the product size, as the smaller particles are unmeasurable with the resolution of the taken image. Therefore, the method provides only a rough estimate of the size reduction in the G81 tests, and the actual size reduction could be higher.
Figure 4.5 a) shows the jaw crusher test configuration and b) the crushing cavity of the jaw crusher with the specimen in place. Figures 4.5 c) and d) present the worn specimen plates after the specimen holders are removed and the wear surfaces are cleaned from mud and dust particles. The most worn area is visible in the middle of Figure 4.5 d), where the surface has a concave shape.

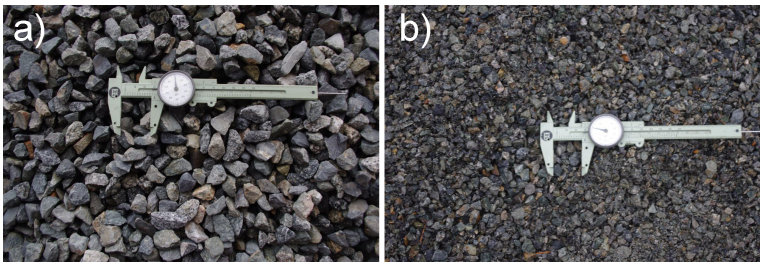

Figure 4.4: *Morainal rock a) before and b) after the test. The distance between the calipers of the ruler is 30 mm.*

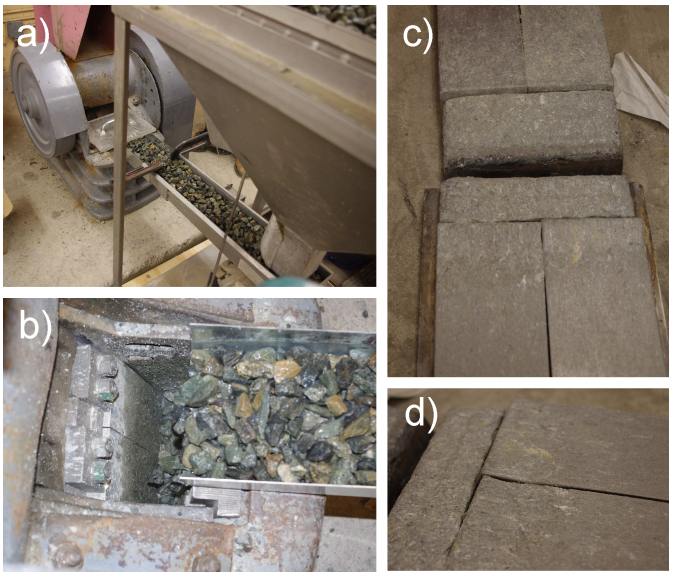

Figure 4.5: *a) The jaw crusher, the hopper and the vibrating linear feeding system, b) the crushing cavity of the jaw crusher with specimen plates in place, c) the jaws set on the table where the upper jaw is the moving jaw and the lower jaw is the stationary jaw, and d) the stationary jaw plates from another angle.*

4.2.2 Tests with the dual pivoted jaw crusher

The main variables that can be changed in a DPJC test are:

- Specimen angle in the specimen holder
- Axle tilt angle β with the swing angle α
- Minimum gap (d_{min}), or closed side setting (CSS)
- Maximum gap (d_{max}), or open side setting (OSS)
- Speed of the jaw crusher
- Crushed abrasive size and type

Three test series were planned to cover most of the above variables. The first test series consisted of repeatability tests with S355 structural steel. The first test series was used also to examine the effect of the axle tilt angle β on the wear of the specimens and on the accumulated work during the tests. The specimen angles and the effect of the rock size on wear and work were tested in the second test series with XT710 manganese steel, which was also used for testing the abrasiveness of different rock types. The third test series compared the wear resistances of carbide reinforced tool steels and the effect of the speed of the jaw crusher on wear. All test series were run with $\beta = 0°$ and $90°$ tilts to compare the fully compressive situation to a situation with an extensive sliding component.

The two-sided swing tests were conducted to examine how the wear of the specimens depends on the movement direction of the jaws. Usually the tests were conducted by swinging the jaws only on one side from the vertical rest position. There is also a possibility to swing the jaws to both sides from the rest position, when the axle tilt angle β is $90°$. The two sided swinging of the jaws produces two identical compression cycles in one turn of the flywheel. The test can be seen as a one-sided swing test where the specimens switch places with every cycle. Both swings were set to have the same 3 mm throw with the 3.15 and 6.15 minimum and maximum gaps. Some additional tests were also conducted with dissimilar specimens to examine how the wear result changes with the selection of the counterface.

A running-in test, or several tests, were conducted on each specimen before the actual test. The rocks can intermix with the wear surface especially in the case of softer steels, which may result in an increase of the weight of the specimen. The steady wear loss of materials begins after 2-6 kg of crushed rocks, depending on the test configuration. The running-in of the test specimens was conducted until the wear of the specimen was presumed to occur in a steady state. The actual tests were carried out by crushing a 4 kg batch of rocks per test.

4.2.2.1 Tests on S355 steel specimens

The repeatability of the test equipment was examined with S355 steel specimens worn by 12.5 mm to 14 mm sized granite from Sorila quarry. Table 4.4 lists the test parameters and shows the compressive displacement ΔZ and the sliding displacement ΔY between the jaws as the ratio $\Delta Z/\Delta Y$. ΔZ differs from the set 3 mm throw as the increasing lateral movement between the $5°$ tilted specimens require larger ΔZ values to achieve similar throw. Three specimen pairs were tested with the $\beta = 90°$ tilt and two specimen pairs with the $\beta = 0°$ tilt. In addition to repeatability, the test series was also used to determine how the compression and sliding motion affect the wear and work in the tests. Tests with $\beta = 45°$ and $\beta = 75°$ tilts were conducted to obtain also results between the extreme movements of the $\beta = 90°$ and $\beta = 0°$ tilts. These tests were conducted with one specimen pair for each tilt.

Table 4.4: *Test parameters of the S355 steel test series.*

β angle	$\Delta Z/\Delta Y$ (mm/mm)	min - max gap (mm)	material	rock size (mm)	tests (4kg)	specimen pairs
$0°$	3/0.3	3.15 - 6.15	S355	12.5 - 14	2	2
$45°$	3.2/3.3	3.15 - 6.15	S355	12.5 - 14	3	1
$75°$	3.9/10.7	3.15 - 6.15	S355	12.5 - 14	3	1
$90°$	5.0/24.0	3.15 - 6.15	S355	12.5 - 14	2	3

4.2.2.2 Tests on manganese steel specimens

The second test series used XT710 manganese steel as a specimen material, which is a typical material for the jaw crusher wear plates. The purpose of the test series was to examine how the change of several parameters affects the test outcomes. Table 4.5 presents the test parameters for each test, showing both the specimen setting S and the crushing setting C. An individual test name is a combination of the above mentioned settings. The first part on the test name (S1-S9) defines the Jaw1 and Jaw2 specimen pair used in the test, and the second part (C1-C8) defines the rock and the crushing parameters of the test. Each test consumed 4 kg of selected abrasive, and several tests were conducted using the same specimen pair. The running-in of each specimen pair was conducted with a 4 kg rock batch. All tests were conducted with a rotational speed of 217 rpm, except for test S9-C8, which was conducted at 315 rpm. Tests from C1 to C4 of each specimen angle were consecutively tested with the same specimen pair. Tests with S7 and S8 specimen pairs compared the crushing behavior of three other rock types, which can also be compared with S1-C1 or S4-C1 tests.

All crushing settings C1-C8 were used to conduct tests with 5° + 5° specimen holders. Crushing settings C1-C4 were also repeated with 10° + 0° and 12.5° + 12.5° specimen holders to test the effect of the specimen holder angle on the crushing situation. Figure 3.6 displays a schematic overview of how the specimen angle affects the movement of the jaw crusher. The tests used several initial rock sizes and crushed the rocks with two close side settings (CSS). The flow chart of the tests with the consecutive crushing settings C1-C4 , which were designed to produce comparable results with similar reduction ratios, is presented in Figure 4.6. Tests with the C1 and C3 settings used the initial rock size distribution of 10 mm - 12.5 mm and crushed the rocks with different gap settings, which produced different reduction ratios of the product. Tests with the C2 setting were continuation tests to crush the product rock of the C1 setting tests into a smaller size with the CSS of 0 mm. This allowed for a comparison between the crushing settings C1 and C2 with different feed and product size, but similar (2:1) reduction ratio. Also the cumulative crushing test result of C1 and C2 settings (C1 + C2) can be compared to the tests with the C3 setting, as they both have the same (4:1) reduction ratio. Tests with the C4 setting crushed the rock with a 4 mm - 6.3 mm size distribution with the CSS of 0 mm. The majority of the product of tests with CSS as 3.15 mm were of size 4-6.3 mm. The similarity of the feed size and the similar (2:1) reduction ratio allow for a comparison of tests with the C2 and C4 settings.

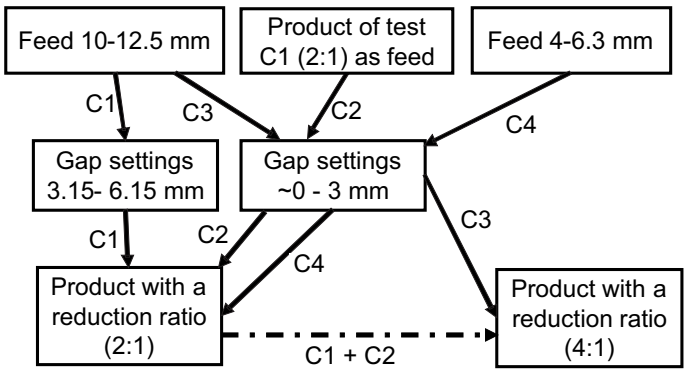

Figure 4.6: *Flow chart of the crushing tests with the XT710 manganese steel*

Table 4.5: *Test parameters of the manganese steel XT710 test series.*

Specimen setting S			Crushing setting C	
Test	β	Specimen angles	Min - Max gap (mm)	Feed (mm) Granite
S1-C1	0°	5°+5°	3.15 - 6.15	10 - 12.5
S1-C2	0°	5°+5°	0 - 3	product of C1
S1-C3	0°	5°+5°	0 - 3	10 - 12.5
S1-C4	0°	5°+5°	0 - 3	4 - 6.3
S2-C1	0°	10°+0°	3.15 - 6.15	10 - 12.5
S2-C2	0°	10°+0°	0 - 3	product of C1
S2-C3	0°	10°+0°	0 - 3	10 - 12.5
S2-C4	0°	10°+0°	0 - 3	4 - 6.3
S3-C1	0°	12.5°+12.5°	3.15 - 6.15	10 - 12.5
S3-C2	0°	12.5°+12.5°	0 - 3	product of C1
S3-C3	0°	12.5°+12.5°	0 - 3	10 - 12.5
S3-C4	0°	12.5°+12.5°	0 - 3	4 - 6.3
S4-C1	90°	5°+5°	3.15 - 6.15	10 - 12.5
S4-C2	90°	5°+5°	0 - 3	product of C1
S4-C3	90°	5°+5°	0 - 3	10 - 12.5
S4-C4	90°	5°+5°	0 - 3	4 - 6.3
S5-C1	90°	10°+0°	3.15 - 6.15	10 - 12.5
S5-C2	90°	10°+0°	0 - 3	product of C1
S5-C3	90°	10°+0°	0 - 3	10 - 12.5
S5-C4	90°	10°+0°	0 - 3	4 - 6.3
S6-C1	90°	12.5°+12.5°	3.15 - 6.15	10 - 12.5
S6-C2	90°	12.5°+12.5°	0 - 3	product of C1
S6-C3	90°	12.5°+12.5°	0 - 3	10 - 12.5
S6-C4	90°	12.5°+12.5°	0 - 3	4 - 6.3

Test	β	Specimen angles	speed	crushing setting	Rock type
S7-C5	0°	5°+5°		as in C1	gneiss
S7-C6	0°	5°+5°		as in C1	tonalite
S7-C7	0°	5°+5°		as in C1	quartz
S8-C5	90°	5°+5°		as in C1	gneiss
S8-C6	90°	5°+5°		as in C1	tonalite
S8-C7	90°	5°+5°		as in C1	quartz
S9-C8	90°	5°+5°	(315 rpm)	as in C1	granite

4.2.2.3 Tests on tool steel specimens

The third test series was used to compare the wear resistance of eight steels. All the tests were conducted with a min-max gap of 3.15 mm - 6.15 mm, 10 mm - 12.5 mm granite from Sorila, and with 5° + 5° specimen holders. Moreover, tests were conducted at three different jaw crusher speeds. All specimens were tested three times with 4 kg batches of rocks after running-in the specimen with a 4 kg rock batch. Table 4.6 lists the materials used in the tests. The ASTM G 81-97 tests were used for comparison with this test series.

Table 4.6: *Test parameters of the tool steel test series. All tests had the minimum and maximum gaps as 3.15 and 6.15 mm, the specimen holder angles as 5° + 5°, and Sorila granite of size 10 - 12.5 mm as the crushing media.*

β	speed (rpm)	S355	QT100	WR6H	WR6SF	WR12	WI5	WI7	WI8
0°	217		X	X	X	X	X	X	X
90°	217	X	X	X	X	X	X	X	X
90°	46	X					X		
90°	315	X	X	X	X	X	X	X	X
G81			X	X	X	X	X	X	X

4.2.2.4 Analysis of the recorded data

The accumulating work was calculated from the recorded data with the Matlab® software. The data was processed with a code, which slightly smoothed the recorded data, synchronized the timing of the channels, calculated the force and displacement from the voltage signals, calculated the coordinate system in use and the sum of the force signals of the two sensors, and integrated the force and displacement data to obtain the accumulating energy. Figure 4.7 shows an example of the force and displacement signal data with the work integral. The effect of elastic compression cycles of the rocks between the jaws is shown in compression peaks 1,2 and 4, counting from the left hand side of the figure. The integrated work returns back to the same level as before the cycle, whereas in cycles 3 and 5 the sudden loss of support from the rock accumulates into work as the rock particle is crushed or slipped between the jaws.

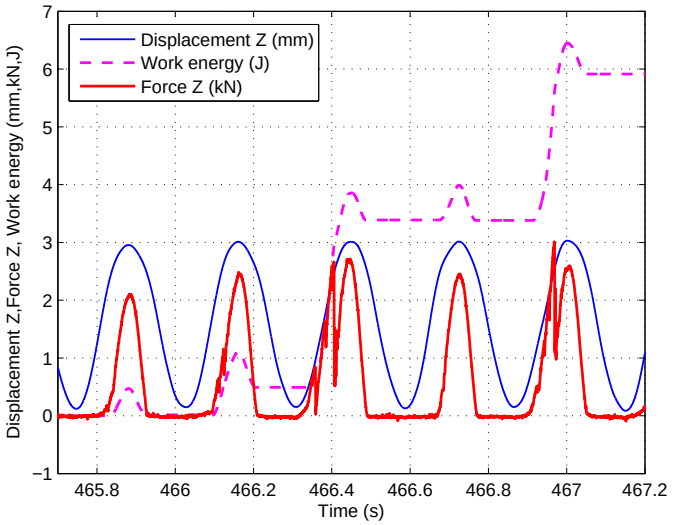

Figure 4.7: *Effect of elastic and inelastic compression on the accumulating work.*

4.3 Wear surface and material characterization

This section describes the methods used for characterizing the wear and changes in the microstructure of the test specimens.

4.3.1 Measurement of wear

The wear of the specimens was determined as the mass loss of the specimen between the initial weighing and weighing after the wear test. The weight of the specimens was measured with 0.001 g accuracy using Precisa XT 1220M scale. Specimens were weighed at least five times, and the median value of the measurements was used as the weighing result, because typically the deviation of the individual measurements of the scale was ±1 mg. The absolute accuracy of the scale was also considered less important, as the mass loss was determined as the change of weight of the specimen. The density of the specimens was measured in order to convert the mass loss to the volumetric loss of the material. This was important as some of the steels had lower density than the ordinary S355 steel due to the alloying elements. The density of the steels was measured by comparing the weight of the specimen in air and immersed in purified and ion changed water. The method calculates the mass of the displaced water m_w from the weight difference of the specimen $m_w = m_{air} - m_{water}$, which is used with the known density (0.998 g/cm^3 at 20 °C) of water ρ_w in equation 4.2.

$$\rho = \frac{m_{air}}{V} = \frac{m_{air}}{\frac{m_w}{\rho_w}} = \frac{m_{air}}{\frac{m_{air}-m_{water}}{\rho_w}} \tag{4.2}$$

4.3.2 Microscopy

The microstructure of the test materials, the specimen wear surfaces, and the cross-sections were examined with Leica MZ75 stereo microscope and Leica DM2500M materials analysis microscope. The specimens were also examined with Zeiss ULTRAplus ultra high resolution field emission scanning electron microscope (SEM). The electron microscope is equipped with through-the-lens secondary and backscatter detectors, angle selective backscatter detector, INCA ENERGY 350 energy dispersive spectrometer (EDS) X-ray detector from Oxford Instruments, a possibility to conduct scanning transmission electron microscopy (STEM), and a Nordlys F400 electron backscatter diffraction (EBSD) detector from HKL.

4.3.3 Hardness testing

The Vickers hardness of the test materials was measured with Struers Duramin A-300 hardness tester with 1, 5, and 10 kg weights. Matsuzawa MMT-X7 micro hardness tester was used for lighter weights. Hardness measurements were taken from both the undeformed parts of the wear test specimens and from the deformed part of the wear test specimen. Two methods were used to measure the deformed wear surface:

1. Cross-sectional measurements.
2. Taper-sectional measurements at a 10° angle to the plane of the wear surface.

Hardness tests from the cross-sections are widely used for the characterization of surfaces. The benefit of this method is the ability to measure the depth profile of the hardness. However, the measurements close to the surface can be unreliable because the sharp edge can cause a loss of strength of the microstructure. Also the edge is often rounded, which causes distorted indentations. The size of the indentation also determines how close to the surface

it is possible to conduct the measurements, and also defines the allowable distance between the indentations. The depth of the Vickers indentation is about 0.2 times the diagonal of the indentation. The cross-sectional hardness depth profiling was used with the specimens of the ASTM G81-97c tests so that measurements were taken up to 50 μm from the wear surface with a spacing of at least two times the diagonal size of the indentations. Also the clearly misshaped indentations were not included in the measured values.

The 10° taper-sections were used in the hardness profiling of the DPJC specimens. Taper-sections are more difficult to produce, but allow more reliable measurement of hardness closer to the surface than with the cross-sectional method, if similar loads are used. The low angle between the taper section and the surface can decrease the effect of the edge proximity to the measured hardness, when compared to the cross-sectional measurement. The hardness values were measured as close as half the diagonal distance from the 170° edge between the wear surface and the taper-section. The depth profile was constructed from measurements along the taper-section up to the surface level, when the angle of the surface was known. However, the indentations from various depths are not from the same location but rather along the surface. Figure 4.8 shows an example of how the three test methods compare with indentations of 50 μm in diagonal, when the highly deformed layer thickness is also 50 μm.

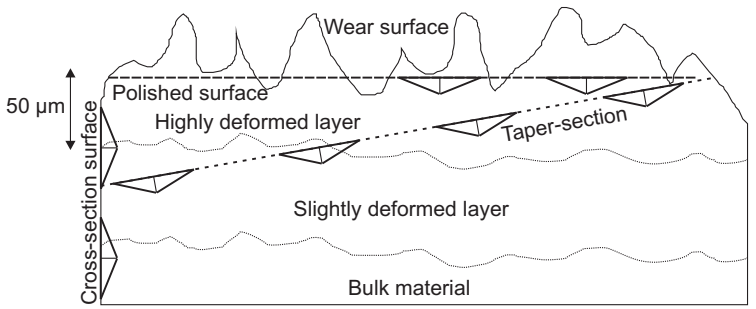

Figure 4.8: *Comparison of the hardness test measurement methods used in this work.*

4.3.4 Specimen preparation

To remove the loose rock particles, the specimens were rinsed with ethanol and gently wiped with a tissue before measuring the weight loss after the wear tests. Ultrasonic cleaning with ethanol as solvent was used before the optical and scanning electron microscopy of the wear surfaces. Cutting and sectioning of the specimens was conducted with Struers Discotom-5 and Accutom-50. Smaller pieces were hot mounted into Polymax mount. The sectioned surfaces of the specimen were ground with P80, P120, P240, P360, P600, P800, P1200 and P2400 papers before polishing with 8 μm, 3 μm and 1 μm diamond paste. Colloidal silica was used as the final polishing step for the EBSD examinations. The taper sections were produced from full sized DPJC specimens by grinding and polishing the wear surface at a 10° angle while supporting the sample in a special holder. The polished surface was finished with Struers OP-S colloidal silica suspension to remove the deformed layer due to grinding. The taper section was also etched with nital 2 % to reveal the microstructure of the sample.

4.3.5 Profilometry

The equipment used for profiling was Veeco WYKO NT1100 optical interferometer, which uses white light interferometry to detect the surface profile, and Alicona Infinite Focus G5, which uses the focus contrast for profiling. The possible objectives for both devices were 5x, 10x, 20x and 50x, in addition to which Alicona could also be operated with 2.5x and 100x objectives. The scratch test specimens were profiled with NT1100, while Alicona was used for the specimens of the DPJC and G81 wear tests.

4.3.6 Rock size analysis

All tested rocks were sieved to control the size distribution before the test and to determine the size change of the rocks after the tests. The rocks were sieved with a Retsch analytical sieve shaker A-200 using a sieve pack of 10 mm, 8 mm, 6.3 mm, 4 mm, 2 mm, 1 mm, 500 μm, 250 μm and the bottom bin. The sieving time for the pack was three minutes. Sieve sizes of 125 μm, 64 μm, and 36 μm were also used for some tests.

5 Results

This chapter presents the results of the wear tests. The information obtained with the sensor systems is also shown in addition to the wear and sieving measurements.

5.1 Jaw crusher tests

The dual pivoted jaw crusher tests were conducted in three series. The first test series concentrated on the repeatability of the tests, while the second test series experimented on how the jaw angles and the rock type and rock size affect the test results. The third series concentrated on the material comparison and how the speed affects the test results. The test results of the third series are compared to the G81 jaw crusher test results.

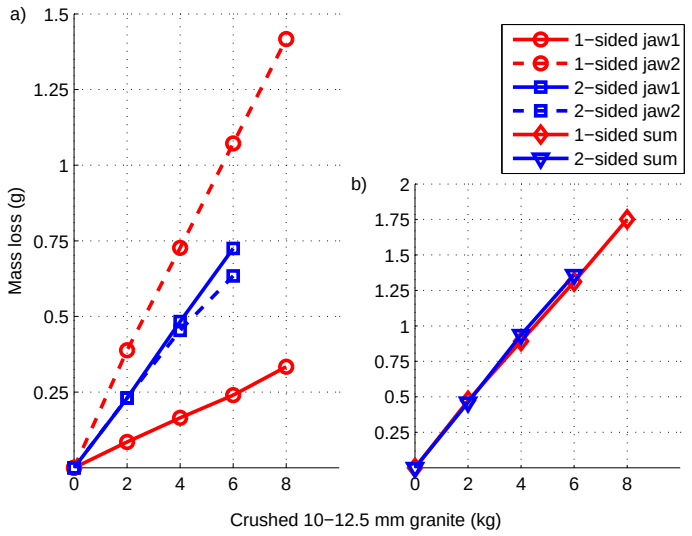

Figure 5.1: *a) QT100 specimen pair worn with the 90° tilt using one-sided and two-sided motion from the vertical rest point, b) sum wear of the specimens.*

Two sided swing tests were performed to further understand the behavior of the test equipment. Figure 5.1 shows two tests conducted with QT100 test material. Both tests are conducted with $\beta = 90°$ differing only in how the jaw swing is set. In one-sided swing the crushing cycle is conducted only in one direction from the vertical position of the jaw frames, where the gap between the jaws is widest with the $\beta = 90°$ tilt. Swing of the jaw frames to either direction closes the gap until it reaches the minimum gap at the extreme position of the swing. When the swing is done to one side only, it causes the sliding wear to occur mainly in one jaw, whereas the two-sided swing produces almost identical wear of the specimens in both jaws. This behavior is shown in Figure 5.1 a), where the two-sided

swing produced quite similar wear in the specimens in both jaws, while the one-sided swing caused a quite large difference between the wear of specimens in each jaw.
The difference between the one-sided and two-sided swing configurations can also be seen in that the two-sided swing specimens change their roles after each swing, where specimens are either pushing the rock to slide against the opposite specimen or are in place to receive the sliding of the rock. Figure 5.1 b) shows that the sum mass loss of the specimens is identical and does not depend on whether the test with the $\beta = 90°$ tilt is conducted with a one-sided or a two-sided swing. However, all the other tests were conduced with a one-sided swing to determine the difference between the wear of the specimens in the Jaw1 and Jaw2 positions.

5.1.1 Tests on S355 specimens

The S355 structural steel and Sorila granite with a size distribution of 12.5 - 14 mm were used to examine the effect of sliding movement with the change of the axle tilt angle β on the test results and the repeatability of the DPJC tests. Figure 5.2 shows the average volume loss of the test specimens with four tilt angles β. The results of the specimens are shown in two separate figures with different vertical scales to better show the differences in the wear rates of the specimens. The running-in tests are also presented on the negative sides of the figure coordinates. Initially, the rock particles intermixed with the softer steel matrix causing the specimen weight to increase. The test with $\beta = 0°$ required a running-in with up to 6 kg of rocks before the wear rate stabilized to follow a nearly linear behavior. In the tests with $\beta = 90°$, the specimens in Jaw2 show almost linear wear, including the running-in test, whereas the Jaw1 specimens have a negligible wear rate during the 2 kg running-in test. The pre-tests with $\beta = 45°$ show behavior similar to the pre-tests with $\beta = 0°$.

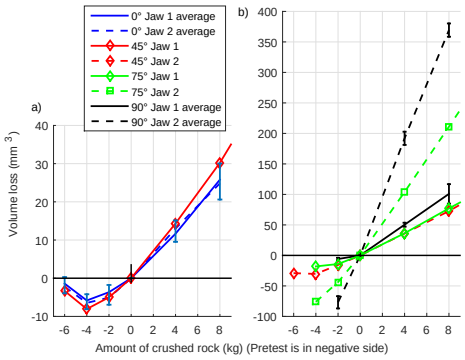

Figure 5.2: *Volume loss of S355 specimens in Jaw1 and Jaw2 with a) $\beta = 0°$, and b) $\beta = 75°$ and 90°. The results with the $\beta = 45°$ tilt are split to show the Jaw1 in a) and the Jaw2 in b). Feed: 12.5 mm - 14 mm granite.*

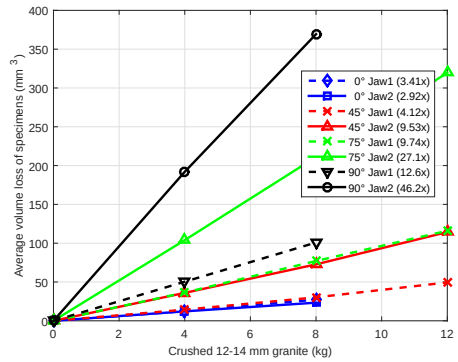

Figure 5.3: *Average volume loss of S355 specimens in Jaw1 and Jaw2. Feed: 12.5 mm - 14 mm granite.*

The error bars in Figure 5.2 show the 95 % confidentiality boundaries of the normal distribution, which is the standard deviation $2\sigma_{st}$ of the tests with $\beta = 0°$ and $\beta = 90°$. The relation of the range of the standard deviation to the volume loss of the material was larger in the tests with $\beta = 0°$ than in the tests with $\beta = 90°$. The repeatability of the tests is discussed further in Section 5.3.

Figure 5.3 shows the average volume loss of the specimens after the running-in tests. The wear rates are nearly linear in all the tests, and the wear rate coefficients of the curves are listed in the legend of the graph. All tests had the same min-max gap, but the amount of lateral displacement ΔY was 0.3 mm, 3.3 mm, 10.7 mm, and 24 mm with $\beta = 0°$, 45°, 75°, and 90°, respectively. The wear rates of the specimens in Jaw1 and Jaw2 were the same, when ΔY of the jaws was 0.3 mm. The Jaw2 specimen was much more affected by the change in the lateral displacement. Even a small increase in ΔY from 0.3 mm to 3.3 mm increased the wear rate of the Jaw2 specimen by a factor of ∼3. Similarly, increasing ΔY from 3 mm to 10.7 mm increased the wear rate by a factor of ∼3. The further increase of ΔY to 24 mm was not as consistent, but in total it caused the Jaw2 specimen wear rate to increase by a factor of 16 from 2.92 mm^3/kg to 46.2 mm^3/kg, whereas the wear rate of the Jaw1 specimen increased only by a factor of four.

The amounts of work needed for crushing the rock were also compared. Figure 5.4 shows the accumulating work during the test. The selected β angle of the test affects the capacity or the time needed to crush the rock. The feed rate of the rock was adjusted according to how fast the DPJC could crush the rocks. The feed rate was set as high as the test configuration allowed. The tests with $\beta = 90°$ are the most efficient in crushing the rocks in the shortest time, and there was no choking of the crusher. With the other axle tilt angles the amount of rocks between the jaws could cause choking of the crushing cycle. This was due to the high contact area of the rock and the elasticity of the jaws, causing only elastic compression of the rocks. The choking needed a manual removal of the excessive rocks from the crushing cavity. Another cause for the seizure of the crushing test was choking of the feeding system. The 12.5-14 mm rock had a higher tendency to get stuck in the feeding tube with an inner diameter of 25 mm. Because of this behavior the accumulating work in Figure 5.4 shows horizontally flat sections where no crushing work was conducted. However, choking of the jaw crusher does not affect the overall accumulating work, and the scatter in the total work integral was small between the tests with the same β tilt.

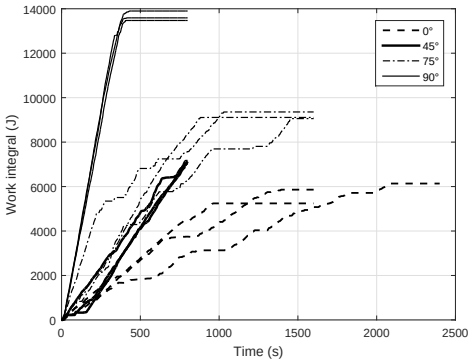

Figure 5.4: *Accumulating energy in the tests with S355 specimens. Blue, red, and black lines show tests with $\beta = 0°$, $\beta = 45°$, $\beta = 75°$,and $\beta = 90°$, respectively. The number indicates the number of individual tests with each axle tilt. Feed: 12.5 mm - 14 mm granite.*

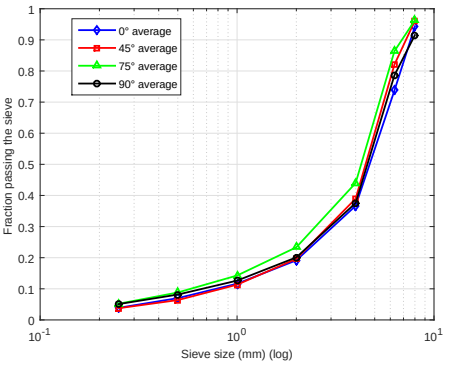

Figure 5.5: *Average sieved size fractions of the product from tests with $\beta = 0°$, 45°, 75°, and 90°. The test material is S355. Feed: 12.5 mm - 14 mm granite.*

Figure 5.5 presents the average size distribution of the 4 kg rock batch after the tests with S355 specimens. There is some minor scatter in the larger rock sizes, but the amounts of smaller rocks are similar. The small scatter shows that the product outcome of the tests is not changed by the change of angle β or the change of the sliding displacement of the jaws.

5.1.1.1 The relation of wear and work

Figure 5.6 shows the relationship between the movement of the DPJC jaws and the wear and work done in the S355 steel tests. As the actual compressive displacement, or the throw, is constant in the tests, the only factor changing in the jaw movement is the lateral displacement, which causes an increase both in the wear rate of the specimens and in the measured work of the system. The increase in the wear rate is not linear but follows roughly the exponential function shown in Figure 5.6. Another possible fit is an exponential function of type y=a*exp$^{b*log10(x)}$.

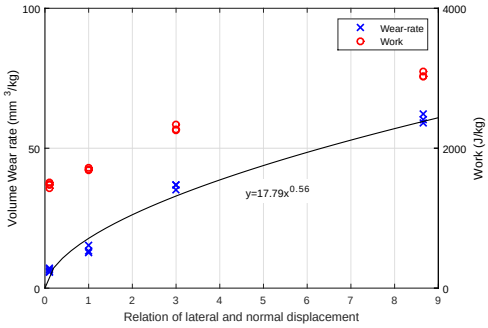

Figure 5.6: *Wear and work as a function of the relation of lateral and normal displacement in the tests with S355 steel specimens. Feed: 12.5 mm - 14 mm granite.*

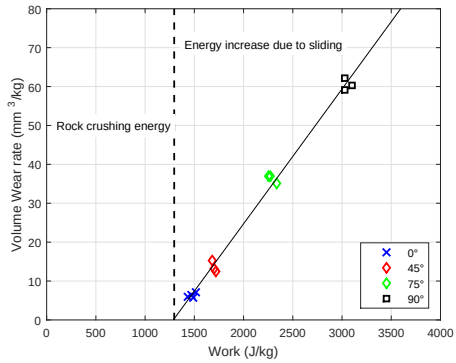

Figure 5.7: *Relation between the wear rate and the work done in the DPJC tests with S355 steel specimens. Feed: 12.5 mm - 14 mm granite.*

Figure 5.7 a) shows the relation between the amounts of wear and work in the first test series with 12.5 mm -14 mm granite and S355 steel specimens also shown in Figure 5.6. Each point in the data represents a separate test with 4 kg of rock crushed per test. The amount of wear increases linearly with increasing work, which is caused by the increase of the sliding distance in the tests with the $\beta = 0°$, $\beta = 45°$, $\beta = 75°$ and $\beta = 90°$ tilts. The increase can be assumed to be caused only by the relation of movement, as all other possible variables were not changed. The linear fit crosses the zero volume wear level at the work of 1300 J/kg, which suggests that a certain amount of energy was consumed in the crushing process and is not related to the movement of the jaw crusher. The total amount of work can be assumed to be a sum of the comminution work W_c needed to crush the feed to product size, and the work needed to wear the specimen W_s, i.e., $W_{work} = W_c + W_s$. The sieving results showed that the outcome of the comminution was similar in all tests, which indicates that similar amounts of work should be needed in comminution. The sliding movement in the test should not have a large effect on how much work is actually consumed in the fracture process of the stones. Usually the compressive forces cause tensile fracture to occur in a plane that is aligned with the direction of compression [7]. The introduction of a sliding component can cause shear stresses in the stone as the resultant force vectors are no longer

on the same plane. However, Refahi et al. [138] stated that in a single spherical particle compression the tensile fracture mechanism is dominant over the shear fracture mechanism, which indicates that the overall crushing work should not be affected by the direction of the force components.
The 1300 J/kg level can be presumed to be the minimum amount of energy E_0 needed to crush the 12.5 mm -14 mm sized particles in the DPJC test. The excess energy is consumed by the sliding of the stones on the specimen surface, which is also causing wear of the specimens. Even the compressive crushing with the $\beta = 0°$ tilt has a small sliding component: when the irregular stones are pushed against the irregular wear surface, the stones can slip and push material small distances on the wear surface. Also the angles of the jaws cause the direction of the compressive force to deviate from the normal of the surface, which promotes slipping and sliding.

5.1.2 Tests on manganese steels

The manganese steel XT710 was used as the specimen material in the second test series. The used rock was mainly Sorila granite of size 10-12.5 mm, but other rock types and sizes were also used. The test series compared how the test results depend on the three varying sets of specimen angles. Figures 5.8 and 5.9 present the volume losses from several tests with the axle tilt $\beta = 0°$ and 90°. The tests with different jaw opening angles (S1-S6) are grouped according to the used crushing setting (from C1 to C4, and C1+C2). The gray scaled bars show the total volume wear rate of both Jaw1 and Jaw2 specimens in the test. The overlaying thinner white and black bars present the individual wear rates of the Jaw1 and Jaw2 specimens, respectively.

The wear of the specimen in Jaw1 was overall slightly higher than in Jaw2, when the specimens were tested with the $\beta = 0°$ tilt in Figure 5.8. The difference in the wear could have been caused by the side plates being attached to the Jaw2 specimen holder, which means that the side plates moved only with respect to the Jaw1 specimen holder. There was also a small gap between the side plates and the Jaw1 specimen holder to prevent contact. As the side plates were 1.5 mm thick steel sheets, the rocks could slightly bend them and cause additional wear of the edges of the specimens in Jaw1. However, the edges were not excessively rounded.

In the tests with the S2 specimen pair, the specimen angles were 10° + 0°, i.e., only the Jaw1 specimen surface was tilted. This resulted in even higher relative wear between the Jaw1 and Jaw2 specimens compared to the tests with evenly tilted specimens. The cumulative wear in both S2-C1 and S2-C2 tests, shown as S2 test of C1+C2 setting in Figure 5.8, has a markedly higher wear of Jaw1 specimen when compared to the S2-C3 test, which also changes the order of the sum wear rates between the tests S1, S2 and S3.

Another interesting result was the very low wear rate in the test S1-C1, being the lowest of the entire series. As the test result was quite different compared to the other C1 tests, the test was repeated with similarly low wear rate. The wear rate of the S1-C1 test was doubled, when the rock product was crushed in the test S1-C2. In addition, tests S1-C3 and S1- C1+C2 gave similar wear rates for both Jaw1 and Jaw2 specimens, as well as for the sum of the specimen wear rates. The third comparison of tests with the C2 and C4 settings showed a similarity between the wear rates, but the overall wear rate in the tests with the C4 setting was lower.

Figure 5.9 shows the wear rates in the tests with $\beta = 90°$. The increased lateral displacement in the Y direction caused higher wear in the specimens in Jaw2 in all tests. Overall, the 10°+0° specimen angles used with the S5 specimen pair significantly decreased the wear rate in comparison to the 5°+5° specimen angles of the S4 specimen pair. Even the order of the higher wear rate was changed when comparing the S4-C1 and S5-C1 tests. The difference comes from the different approach of the jaws shown in Figure 3.7, depending on the jaw angle of Jaw2. In the tests with 10°+0° jaw angles, the lateral and compressive movements of the jaws begin from the maximum gap and increase slowly. In comparison, the lateral movement of the jaws in the tests with 5°+5° specimen angles causes further opening of the jaw from its open position. This effect causes higher velocity of the lateral movement when the actual compressive movement of the jaws begins. The increased speed of the contact could cause the different wear rate between the tests with the S4 and S5 specimen pairs.
The wear rates in the tests with C3 and C1+C2 crushing settings were quite similar for all S4, S5, and S6 specimen pairs. Also the tests with C2 and C4 settings showed similar wear rates. The tests with $\beta = 90°$ clearly show that the individual wear rates in the tests with C1 and C2 settings can be cumulative. There was no distinctive difference in the wear rates when the rock was crushed in one or two stages, if the product size was similar. In most cases, the larger rock size tests with the C1 setting had a slightly higher wear rate as compared to the tests with the C2 setting.

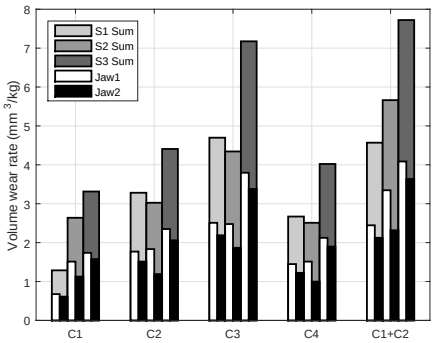

Figure 5.8: *Volume wear rates of XT710 specimens in the tests with $\beta = 0°$ tilt. Feed: 10 mm - 12.5 mm granite.*

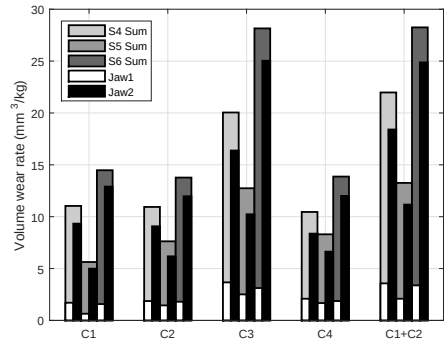

Figure 5.9: *Volume wear rates of XT710 specimens in the test with $\beta = 90°$ tilt. Feed: 10 mm - 12.5 mm granite.*

The accumulated work was determined from all tests. Figure 5.10 shows the amount of work in the tests with the tilt angle $\beta = 0°$, where the white and black bars are the work done in compressive Z and lateral Y directions, respectively. The gray bars show the sums of the work in Z and Y directions. The work is shown both in a) Z-Y coordinates aligned according to the sensor and in b) Z_2-Y_2 coordinates aligned normal and parallel to the surface of the specimens in Jaw2. The Z_2-Y_2 coordinates are used, since most of the increase in the wear rate caused by the increase in the lateral movement is subjected to the Jaw2 specimens. Setting of the coordinates along the specimen surface is presented schematically in Figure 3.7. The amount of work in the Y_2 direction is increased when the coordinate system is changed to have the Y_2 direction parallel to the specimen surface. Also, the work in the Z_2 direction is decreased by roughly the same amount. In principle, the total amount of work should be the same and not dependent on the coordinate system. Small deviations are

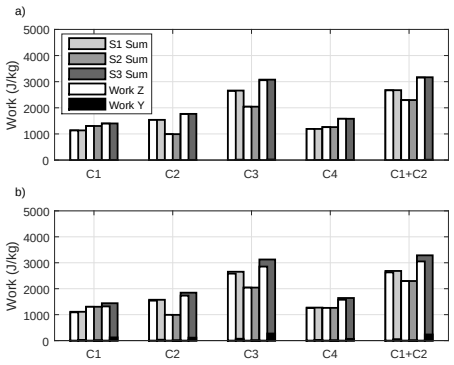

Figure 5.10: *Accumulated work during the tests with XT710 specimens and $\beta = 0°$ tilt. In a) the normal force F_Z and lateral force F_Y are in the coordinate system of the force sensors, and in b) F_{Z2} and F_{Y2} are in the coordinate system aligned according to the Jaw2 specimen surface. Feed: 10 mm - 12.5 mm granite.*

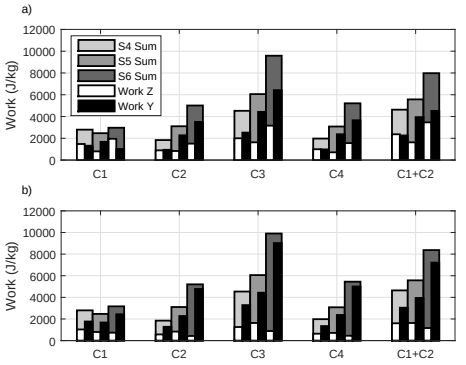

Figure 5.11: *Accumulated work during the tests with XT710 specimens and $\beta = 90°$ tilt. In a) the normal force F_Z and lateral force F_Y are in the coordinate system of the force sensors, and in b) F_{Z2} and F_{Y2} are in the coordinate system aligned according to the Jaw2 specimen surface. Feed: 10 mm - 12.5 mm granite.*

caused by the algorithm that reads the measured data and calculates the accumulated work.

When the work in the tests with S1 (5°+5°) and S2 (10°+0°) specimen pairs are compared, the amounts of work show similar levels with the C1 and C4 settings. When the tests are continued with the C2 crushing setting, the amount of work increases in the S1-C2 and S3-C2 tests but decreases with S2-C2. Supposedly the smaller feed size in the tests with the C2 crushing setting comminutes easier, when the jaw angles are uneven, which could also show as a lower volume wear rate in the S2-C2 test than in the other tests with the C2 crushing setting. The same trend is shown for C3 and C1+C2 test settings. However, it is unclear why the benefit of the S2 setting compared with the other settings does not show in the tests with the C4 setting.

Figure 5.11 shows the accumulating work in the tests with $\beta = 90°$ tilt. Generally, the work is highly increased with the increase of the lateral movement between the jaws. At maximum the increase in the lateral movement triples the amount of work in the S6-C3 test with 12.5°+12.5° specimen angles, when compared to the work in the S3-C3 test. Similar comparison between tests S2-C3 and S5-C3 yields the same factor, whereas tests S1-C3 and S4-C3 have the same factor of less than two. When comparing similar factors of wear, tests S2-C3 and S5-C3 and tests S3-C3 and S6-C3 have roughly the same factor of three between the wear rates, whereas for S1-C3 and S4-C3 tests this factor is over four. These numbers mean that the increase in the lateral movement causes a much higher wear increase, and the amount of consumed work in the tests with the (5°+5°) specimen angles is lower compared to other specimen angle configurations.

Overall, the tests with the widest specimen angles produced the highest amount of wear and work. The trend of lower amount of work in the tests with the S2 specimen pair and $\beta = 0°$ tilt is not shown in the tests with the S5 specimen pair and $\beta = 90°$ tilt, whereas the

tests with the S4 specimen pair showed the lowest amount of work with the C2, C3 and C4 crushing settings. In the tests with the C1 crushing setting, the amount of work is more or less similar for all specimen pairs with the $\beta = 90°$ tilt. The comparison of tests with C3 and C1+C2 crushing settings shows similar amount of work with S4 and S5 specimen pairs, whereas for some reason the tests with the S6 specimen pair shows higher work with the C3 than with the C1+C2 crushing setting.

The final part of the manganese tests included tests with several rock types. These tests were conducted only with 5°+5° specimen angles. Figure 5.12 shows a) the amount of work needed to crush 1 kg rock batches with the initial size of 10-12.5 mm, and b) the wear rate of the specimens tested with both $\beta = 0°$ and 90° tilts. Both granite and gneiss produced similar amounts of work and wear during the tests. Similar kind of comparison was previously conducted with the crushing pin-on-disc [139], which also showed similar wear rates for granite and gneiss, when the wear of the pin was compared to the comminution rate of the rocks. Tonalite had both the highest work energy and wear rate of the tested rock types. Quartzite produced the second highest amount of wear but the lowest comminution work, since quartzite had the lowest mechanical strength.

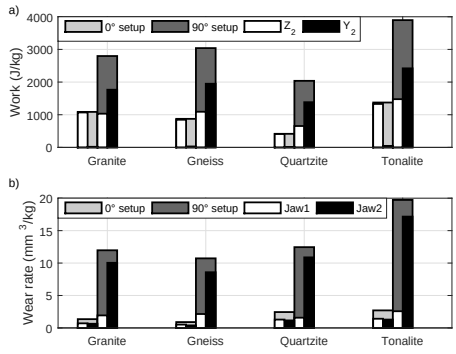

Figure 5.12: *a) Accumulated work in the Z_2 and Y_2 coordinate system (white & black bars) and the total work with various rocks (grey bars), b) wear rate of the Jaw1 and Jaw2 specimens with various rocks (white & black bars), and the total wear (grey bars). The specimen angles were 5°+5°. Feed: 10 mm - 12.5 mm granite.*

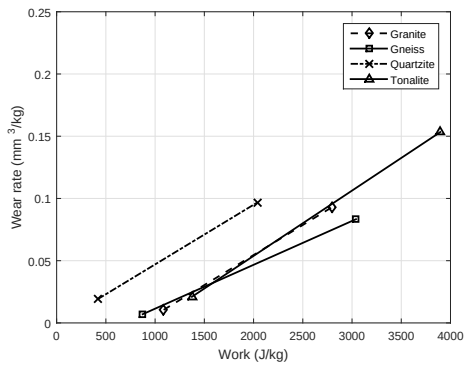

Figure 5.13: *Relationship between wear and work in the tests with various rocks. The tests conducted with $\beta = 0°$ and 90° tilts are shown as a pair of markers, which are connected with a line. Feed size: 10 mm - 12.5 mm.*

Figure 5.13 shows the relationship of wear and work for different rock types. Gneiss, granite and tonalite group together along a line starting from 1000 J. Tonalite, being the toughest of the studied abrasives, shows higher work and wear than gneiss and granite but positions itself along the same line. This suggests that regardless of the mechanical strength of the rock, the relationship of wear and work is the same. This is not true with quartzite, which shows a totally different slope and position in the chart. The minimum energy needed for comminution falls to very low values, which indicates that quartzite is either very brittle or its crack density is high. The slopes of the lines are fairly the same, which means that the increase in the sliding movement increases wear and work by the same relative amount as for the other rock types.

5.1.2.1 Size distribution of abrasives after the tests

Figure 5.14 shows the abrasive size distributions after the tests with S1 ($\beta = 0°$) and S4 ($\beta = 90°$) specimen pairs and 5°+5° specimen angles. There is a difference between the product sizes of tests S1-C1 and S4-C1. However, the change of the axle tilt angle caused no difference between the product sizes, when the crushing was continued with the C2 crushing setting. Also the tests with the C3 crushing setting produced a similar size distribution as the tests with the C2 crushing setting, whereas crushing with the C4 setting produced a coarser product size than the tests with the C2 and C3 crushing settings. The product of the tests with the C1 setting contained a wider size distribution of rocks, which in turn allows the crushing events to occur in a wider gap range. Smaller feed size of the C4 setting with a narrow size distribution of rocks uses a narrower region of the specimens to crush the rocks, being quite close to the minimum gap end of the specimens. This again could allow more rocks to escape the crushing cavity during the opening cycle.

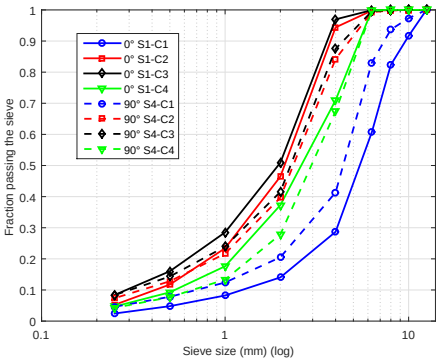

Figure 5.14: *Size distribution of the rocks after the tests with XT710 specimens and 5°+5° specimen angles. Feed: 10 mm - 12.5 mm granite.*

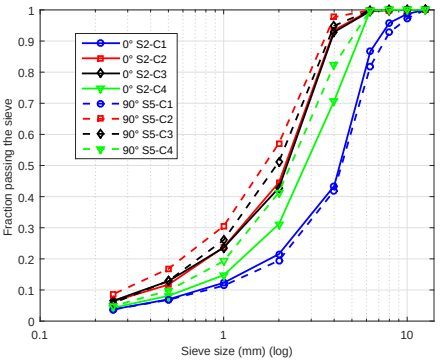

Figure 5.15: *Size distribution of the rocks after the tests with XT710 specimens and 10°+0° specimen angles. Feed: 10 mm - 12.5 mm granite.*

Figure 5.15 shows the size distributions after the tests with S2 and S5 specimen pairs and 10°+0° specimen angles. The size distributions of the rock product show similarity to the tests conducted with the S1 and S4 specimen pairs. Also the tests with S3 and S6 specimen pairs and 12.5°+12.5° specimen angles show similar product size distributions, as presented in Figure 5.16. The size distribution of the test S6-C1 was unfortunately not measured before the test S6-C2. Although there are variations in the test results, the trend and the order of the results show similarity at all specimen angles. The product of the tests with the C4 crushing setting was the coarsest of the tests conducted with the minimum and maximum gaps set as 0 mm and 3 mm.

Because there seems to be some variation in the product size, the reduction ratios RR of the tests were calculated with Equation 2.1. This shows that there is some variation between the tests, where for example the RR of the C4 setting is generally lower. The average values of the tests with the C1 and C2 settings are close to the approximated RR of (2:1), but there are quite big deviations between the tests with different jaw angles. The tests with C3 and C4 produce lower RR ratios than the approximated ratios of (4:1) and (2:1).

Figure 5.17 shows the product size distribution of different rock types. Granite and gneiss have a very similar product size distribution, but tonalite shows a slightly coarser prod-

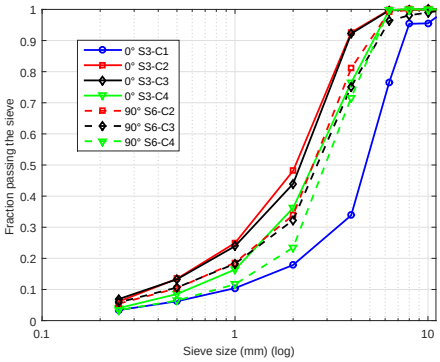

Figure 5.16: *Size distribution of the rocks after the tests with XT710 specimens and 12.5°+12.5° specimen angles. Feed: 10 mm - 12.5 mm granite.*

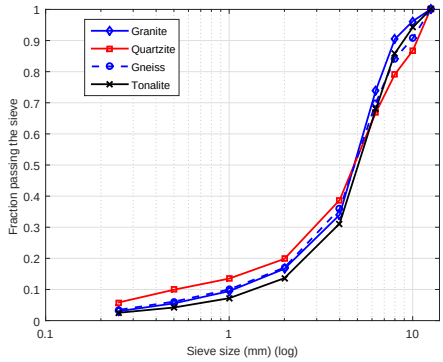

Figure 5.17: *Product size distribution of several rock types after the tests with XT710 specimens, 5°+5° specimen angles and β = 90° tilt. Feed: 10 mm - 12.5 mm.*

Table 5.1: *Measured reduction ratios RR of the F_{80} and P_{80} values of granite rock from the tests with XT710 steel specimens. (!) The RR value of test S6-C2 represents the total reduction ratio after both C1 and C2 tests (C1+C2).*

β	Crushing setting $->$	C1	C2	C3	C4
angle	Specimen angles	RR	RR	RR	RR
0°	5°+5° (S1)	1.6	2.3	4.0	1.2
0°	10°+0° (S2)	2.0	1.76	3.5	1.3
0°	12.5°+12.5° (S3)	1.9	2.3	4.1	1.6
90°	5°+5° (S4)	2.4	1.3	3.3	1.2
90°	10°+0° (S5)	2.0	2.0	4.0	1.5
90°	12.5°+12.5° (S6)		3.0(!)	3.4	1.5
	Average ($\pm 2\sigma$)	1.96 $\pm$0.61	1.94 $\pm$0.85	3.74 $\pm$0.69	1.38 $\pm$0.35

uct size. The difference between the size distributions seems small, when considering the variations caused by the geometry of motion in the granite tests. Quartzite shows a size distribution containing finer sized product and a smaller amount of coarse sized product than the other minerals. The difference is notable when compared to the tests with granite and gneiss, but it can also be due to random variations in the tests.

5.1.2.2 The effect of test geometry on the relationship of work and wear

The results of the tests with the S355 steel demonstrated a linear relationship between wear and work. The tests conducted on the manganese steels can be used to estimate the effect of the feed size, the reduction ratio, and the jaw angles on the relationship of the wear of the specimens and the accumulated work. The tests were conducted on XT710 specimens using a smaller feed size than in the tests with the S355 steel specimens. Therefore, the test settings are not quite identical. Figure 5.18 a) shows a comparison of the volume wear rate and work in the tests where 10-12.5 mm feed was crushed to the product of size P_{cr} (C1) and 0-3 mm (C3). Figure 5.19 a) shows the tests with the feeds of size P_{cr} and 4-6

mm crushed into the product size of 0-3 mm (C2 and C4). Each pair of markers shown in Figures 5.18 and 5.19 are tests with the same jaw angle and axle tilt angles of $\beta = 0°$ and 90°. For example, the tests with the S1 & S4 specimen pairs have the same jaw angles of the specimens but different sliding movement. The slopes of the lines indicate how much wear and work increase with the increased sliding movement of the jaws, which is assumed to be similarly linear as in Figure 5.7 with the S355 steel specimens.

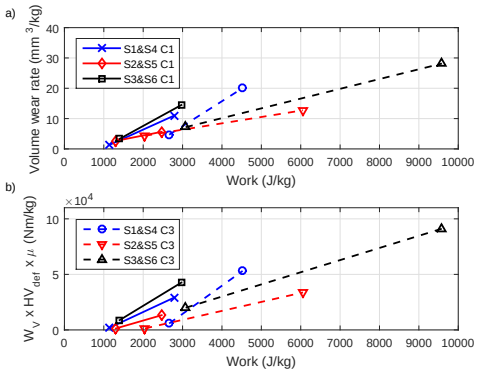

Figure 5.18: *a) Relation between the wear rate of the XT710 specimens and the work at all tested specimen angles of the C1 and C3 crushing settings, b) relation between the wear rate, adjusted by the deformation hardness and μ, and work.*

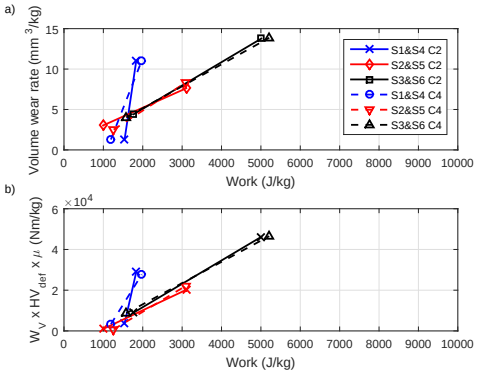

Figure 5.19: *a) Relation between the wear rate of the XT710 specimens and the work at all tested specimen angles of the C2 and C4 crushing settings, b) relation between the wear rate, adjusted by the deformation hardness and μ, and work.*

The tests with the C1 crushing setting show increasing amounts of wear and work, when the specimen angle changes from 10°+0° (S2 & S5) to 5°+5° (S1 & S4) and to 12.5°+12.5° (S3 & S6). The increased reduction ratio RR of the C3 crushing setting increases both wear and work with all jaw angles compared to the tests with the C1 crushing setting. However, the minimum energy value E_0 of comminution is not as clear in these tests, when compared to the tests with the S355 specimens. The 5°+5° jaw angle tests with the C1 crushing setting show the minimum energy of around 1000 J/kg for RR = 2, and about 2000 J/kg when the approximate reduction ratio is doubled. However, the tests with 10°+0° jaw angles show quite much variation in the values. Figure 5.19 a) of the smaller feed size shows similar results for both 10°+0° and 12.5°+12.5° jaw angles, causing the value of E_0 to be very small.

Not all test pairs show the expected result of reaching the zero wear rate at a certain amount of work. These deviations in Figures 5.18 a) and 5.19 a) can be explained by examining the other variables that have been changing between the tests. Figure 5.20 shows the friction coefficient of the events, which accumulated work. The coefficient of friction of abrasion against Jaw2 specimen increases with an increasing jaw angle. Also the change of deformation hardening of the specimen can affect the wear and friction results. Figure 5.20 a), b), c) and d) show the test results for the C1, C2, C3 and C4 crushing settings, respectively. Equation 2.44 can be used to estimate the effect of μ on the wear rate and work in the test. The μ values were taken from the peak positions of the curves in Figure 5.20. In addition, the deformed hardness of the Jaw2 specimen surface from the tests with 5°+5° specimen angles shown in Figure 5.38 was used in the equation. Figures 5.18 b) and

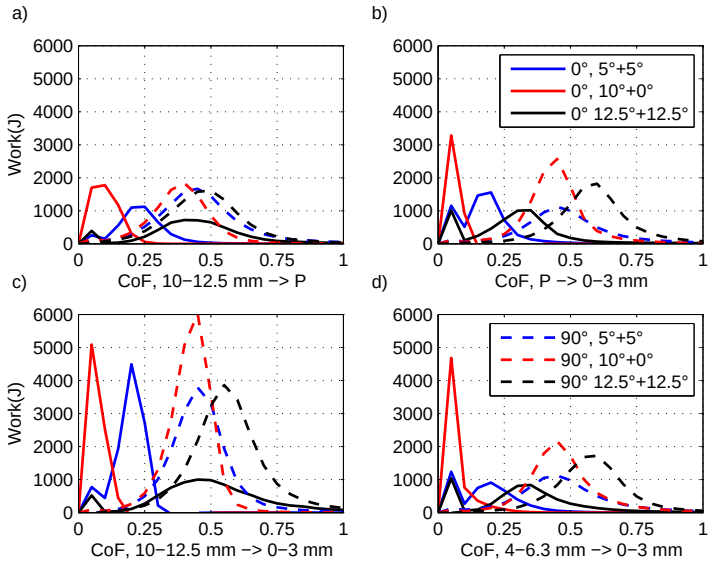

Figure 5.20: *Work accumulation as a function of the friction coefficient in the tests on the XT710 steel and granite feed.*

5.19 b) show the relation between the wear rate, multiplied by the coefficient of friction and the deformation hardness, and the amount of work. The slopes in the plots are the dimensionless wear coefficient K values of Equation 2.44. The adjusted wear rate decreases the variations of E_0, when Equation 2.44 is used to take into account the changed variables of the tests. The results show a better grouping of E_0 values at around 1000 J/kg or 2000 J/kg, when the reduction ratio RR is 2 or 4, respectively.

Figures 5.18 and 5.19 show that there is a difference in the minimum energy E_0 depending on the reduction ratio RR of the crushing setting, and that the slope of the test pairs depends somewhat on the selected jaw angles of the specimens. Figure 5.21 shows another comparison of the tests with the C1, C2 and C3 crushing setting, where the markers connected with a line show the cumulative results of C1 and C2 tests (C1+C2) with either $\beta = 0°$ or 90° tilt. The tests with the C3 crushing setting are shown with connected markers between the tests with the $\beta = 0°$ and 90° tilt. The comparison shows that most tests with the $\beta = 0°$ tilt have a similar slope and are grouped together, with the exception of tests S1 C1+C2 with a lower wear rate. This group also contains the tests S5 C1+C2 with the $\beta = 90°$ tilt, and tests S2 & S5 C3, which were all conducted with the 10°+0° specimen angles. The other tests S4 C1+C2 and S6 C1+C2 with the $\beta = 90°$ tilt show much steeper slopes and have higher amount of wear of the specimen relative to the amount of consumed work in the tests. The end points of the lines also meet with the markers from the tests (S1 & S4 C3 and S3 & S6 C3) done with the C3 crushing settings, which crush the rock batch similarly to the sum of the C1 and C2 settings. The steeper slope in the tests with a large sliding component and tilted Jaw2 specimen shows that the work needed for the wear is lower compared to the grouped slope of the other tests. This indicates that the wear removal mechanism could have changed due to the increase of the sliding movement.

The above results showed only the relationship between the wear, or wear modified with μ and H_{def}, and work. The size distribution of the product from the manganese test showed that the reduction ratio is not exactly constant between the tests, and can be seen to affect

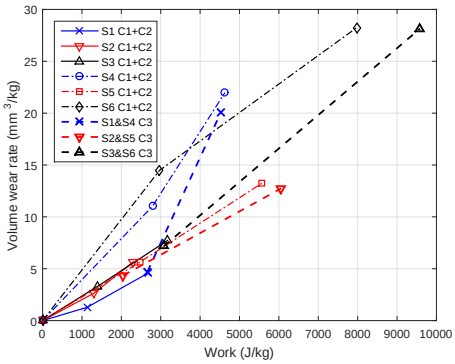

Figure 5.21: *XT710 specimen wear and work comparison of the cumulative tests C1+C2 with either $\beta = 0°$ or $\beta = 90°$ tilts and tests with the C3 crushing setting with both $\beta = 0°$ and $\beta = 90°$ tilt.*

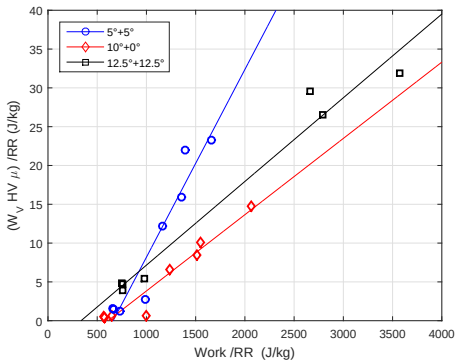

Figure 5.22: *Relationship between modified wear and work in the tests with the XT710 steel, when both are normalized with the reduction ratio RR.*

the outcome of both work and wear. Figure 5.22 shows a comparison between the modified wear and work, when the reduction ratio is used to normalize both wear and work. This compensates for example for the lower amount of crushing in the tests with the C4 crushing setting, and also normalizes the higher RR of the tests with the C3 crushing setting to the same level with the other tests. The higher work values show the results of $\beta = 90°$ tilt with a linear fit between the tests with $\beta = 0°$ and 90° tilts. The S6-C1 and S6-C2 test is showed as the sum of wear and work (C1+C2) with a single marker, as only the size distribution result from the S6-C2 test was measured. This comparison shows similar results as in Figure 5.21, where the tests with the 5°+5° specimen angles show a higher slope of the fit compared to the other specimen angles. The tests align nicely with the fitted lines with few outliers, and the tests with the specimen angles of 5°+5° and 10°+0° meet at work levels of around 600 J/kg, which yields 1200 J/kg of work with RR = (2:1). This is higher than the estimated 1000 J/kg, but the method of calculating the minimum energy is more complex with the implementation of μ and H_{def}. These tests cannot discriminate which of the minimum crushing energy values are correct. The slopes of the tests with 12.5°+12.5° do not show similar minimum crushing work values. This could also mean that the fit might not be linear in all cases. The easier slipping of the rock with larger jaw opening angles could be reasoned to be caused by the larger amount of low contact slipping, as the measured contact force producing most work in the tests with the C3 crushing setting is around 1.5 kN with the 12.5°+12.5° specimen angles and around 2.5 kN with the specimen angles of 5°+5°.

5.1.3 Tests on tool steel specimens

This test series compared the wear and work in the tests conducted on several carbide reinforced tool steels. Figure 5.23 shows the average wear rate of the tool steel and QT100 specimens with $\beta = 0°$ and 90° tilts. The average wear in the test with $\beta = 90°$ was calculated from five tests with a 4 kg rock batch. The average wear in the tests with $\beta = 0°$ was calculated from three tests. The white and black bars in Figure 5.23 are the wear of the specimens in Jaw1 and Jaw2, respectively, and the height of the gray bars represents

the sum wear of the specimens. The amounts of wear are rather low, as the selected tool steels have a high hardness and are designed for high wear resistance. The steels of the WI series show lower wear rates in the tests with the $\beta = 90°$ tilt in comparison to the steels of the WR series. However, there was no clear trend observed in the tests with the $\beta = 0°$ tilt.

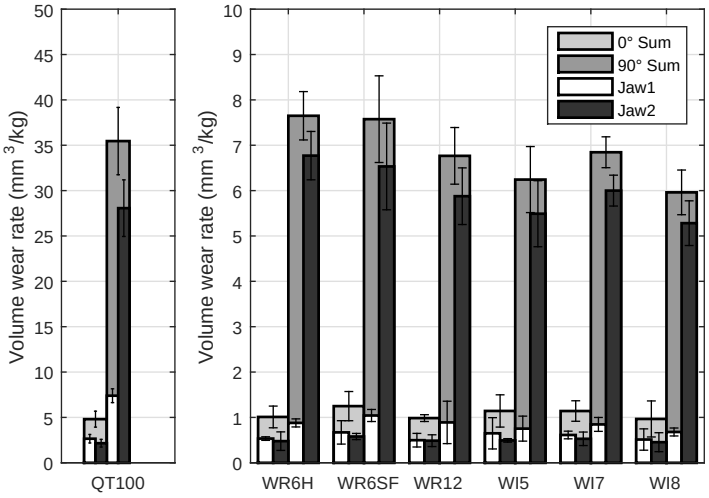

Figure 5.23: *Volume wear rates of the Jaw1 (white) and Jaw2 (Black) specimens, and the total wear rate of both specimens (gray) of the tool steel series. The error bars show the $2\sigma_{st}$ variance. Feed: 10 mm - 12.5 mm granite.*

The accumulated work was calculated from single tests with $\beta = 90°$, and from the average of three tests with $\beta = 0°$. The results are shown in Figure 5.24. The softer steel QT100 requires the same amount of work in the test as the harder steels. It appears that the amount of work is more dependent on the geometry and movement of the jaws than on the material of the specimen. The WI5 steel, which has the highest carbide content and hardness, requires the lowest work at both $\beta = 90°$ and $\beta = 0°$ tilts. The work is done mainly in the Z_2 direction with the $\beta = 0°$ tilt, whereas with $\beta = 90°$ the work is quite evenly divided between the Z_2 and Y_2 directions, where the compressive work in Z_2 direction is generally only slightly increased from the $\beta = 0°$. The comparison of work in the Z_2 and Y_2 directions shows higher amount of lateral work for the softer QT100 steels than for the harder tool steels. The harder surface usually has lower roughness, as the penetration of the particles is shallower. This can lead to a lower amount of frictional resistance towards sliding and lower amount of work in the lateral direction compared to the compressive work.

The ASTM G81-97 tests showed a similar difference between the wear rates of the moving and stationary jaw plates as the DPJC tests with the Jaw1 and Jaw2 specimens. Figure 5.25 shows that the stationary jaw reference plates Rs had the highest wear-rate. The control test with only QT100 specimens is also shown, indicating that in all jaw positions the QT100 pair wears more than when the opposing jaw is of a harder steel. This trend could also be the cause for the lower wear rates of the Rs reference specimens when matched with the harder WI series steels. The lowest value of Rs in the WI8 test shows quite large deviation

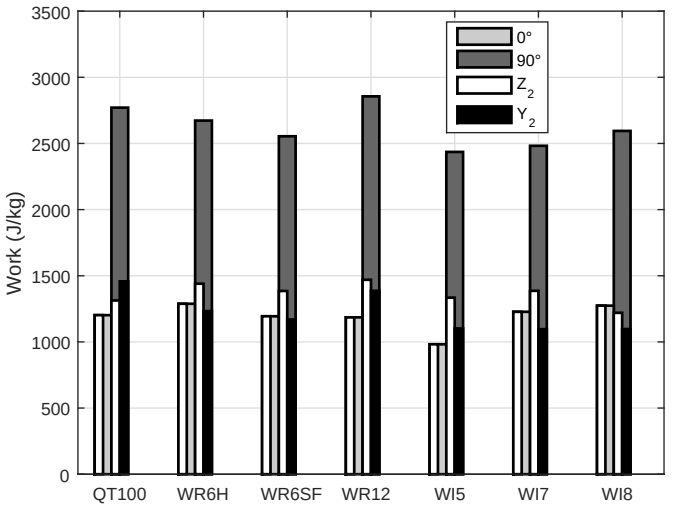

Figure 5.24: *Accumulated work with the $\beta = 0°$ and 90° tilts. Feed: 10 mm - 12.5 mm granite.*

from the other tests. The test was conducted with rock containing snow, which might have changed the wear conditions such as the temperature of the jaw crusher and had an effect on the weight measurements of the rock batch. Interestingly, the reference plates of the moving jaw Rm showed higher wear rates when the opposing jaw was of WI series steels compared to the WR series steels. The hardness of the specimen materials could have also influenced this behavior.

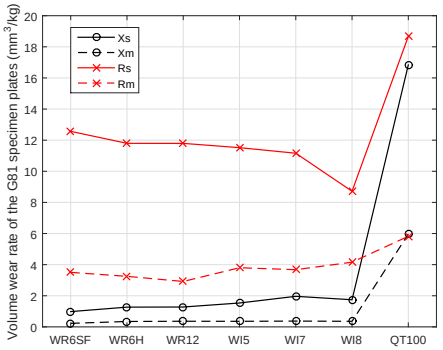

Figure 5.25: *Wear rates of the specimen and reference plates in the ASTM G81-97 tests with the calibration test using only QT100 specimens. Feed: ∼ 25 mm morainal rock.*

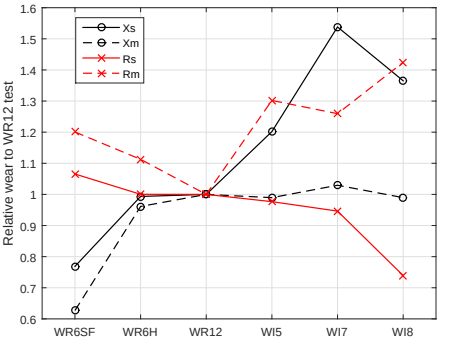

Figure 5.26: *The wear of jaw plates in the ASTM G81-97 test normalized with the result of the WR12 jaw plates. Feed: ∼ 25 mm morainal rock.*

Figure 5.26 shows the wear rate of the specimen plates relative to the test with the WR12

specimens, which allows for a better comparison of the specimen plates. The wear rate of the WI series steels as the stationary jaw test specimen Xs was generally higher than that of the WR series steels, and for the WR6SF the wear rate was exceptionally low. Interestingly, the total wear rate as the sum of all specimens in the test varied from 15.9 mm^3/kg to 16.6 mm^3/kg in all tests, except for WI8, which reached only 14.4 mm^3/kg because of the decreased wear rate of the Rs reference plate. When excluding the WI8 result, the standard deviation of the sum wear was 0.30 mm^3/kg, which is lower than the 0.41 mm^3/kg and 0.39 mm^3/kg of the sum wear of specimen or reference plates, respectively. The results show that the wear rates of the jaw plates are not independent but are affected by the properties of the opposing jaw plate.

The wear ratios of the specimens to the reference are required in order to compare the results of DPJC with the G81 test results. The wear ratio for the DPJC tests was calculated from the volume loss result of the specimen divided by the volume loss result of the QT100 reference, and for the G81 test according to the ASTM G 81-97 standard. Figure 5.27 a) presents the wear ratios of the tool steels individually for the specimens in Jaw1 and Jaw2, and for the sum wear of the specimens. The G81 test is shown as a black bar in Figure 5.27.

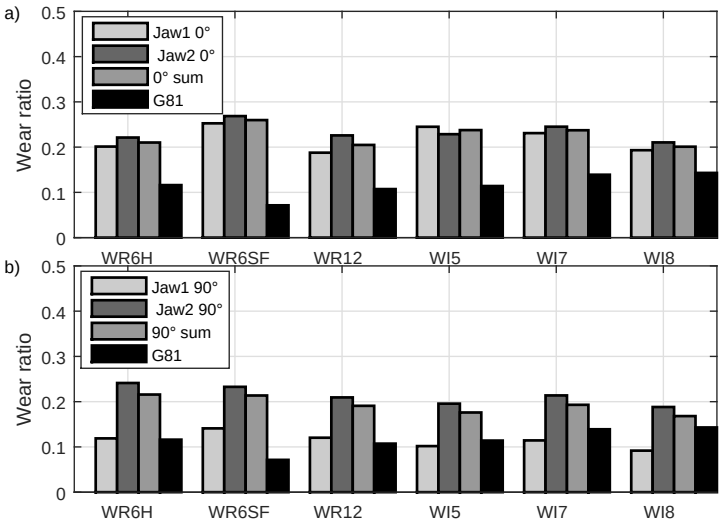

Figure 5.27: *Wear ratio of the tool steels to the QT100 reference with a) $\beta = 0°$ and b) $\beta = 90°$. Feed in DPJC tests: 10 mm - 12.5 mm granite, in G81 tests ∼ 25 mm morainal rock.*

WR6SF had the lowest wear ratio in the G81 tests, and overall the WR steels performed better than the WI steels. In the DPJC tests with $\beta = 90°$, WR6SF had the highest wear ratio of the WR steels, which was also close to the WI7 and WI8 wear ratios. WR12 had the lowest wear ratio of the WR steels with $\beta = 90°$ and shared the lowest wear ratio position with the WI8 steel in the tests with the $\beta = 0°$ tilt. The test materials in the WI series had a higher wear ratio than the WR steels in the G81 tests, which is opposite to the tests with $\beta = 90°$, where WI5 and WI8 steels showed the lowest wear ratios. Generally, the wear ratio to the reference is higher in the DPJC tests than in the G81 tests. Only when the individual jaw wear ratios are compared, the wear ratio of the specimen in Jaw1 in the tests

with the $\beta = 90°$ tilt is in the same range with the G81 tests.

5.1.3.1 Speed tests

The dynamic wear behavior of the test materials was studied by increasing the speed of the jaw crusher in the tests with $\beta = 90°$. The specimen angles were 5°+5°, and the granite rock batch of 4 kg for each test was of size 10 - 12.5 mm. The specimens were tested at the speed of 315 rpm in addition to the normal speed of 210 rpm. These test series included also the S355 and XT710 materials from the first two test series. Slow speed tests of 50 rpm were also conducted on two steels. Figure 5.28 shows the volume loss of the specimens at three different speeds.
The increasing speed of the equipment also increased the wear rate of the specimens, with an exception of QT100. The wear was mostly increasing in the specimens in Jaw2, which received the sliding movement of the rock. In the case of the WI5 steel, the wear of the specimen in Jaw2 decreased significantly at the slower 50 rpm speed, whereas the Jaw1 wear rate was similar at all crushing speeds. The increase of wear was slightly higher for the steels of the WR series compared with the steels of the WI series.

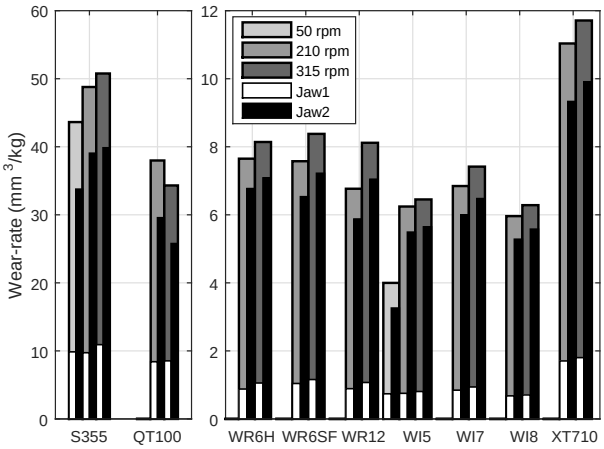

Figure 5.28: *Effect of speed on the wear of the specimen. The grey bars show the total wear rate of the specimens and the white and black bars the wear rate of the Jaw1 and Jaw2 specimens, respectively. Feed: 10 mm - 12.5 mm granite.*

Also the accumulated work increased when the speed of the jaw crusher was increased. Figure 5.29 shows the amount of work per kg of crushed rock. At 50 rpm, the amount of work required by the WI5 steel did not change much, whereas for the S355 steel the measured work was smaller than in the tests with the speed of 210 rpm. The increase of the speed from 210 rpm to 315 rpm increased the amount of work for most of the materials. The two exceptions were the decrease of work for the S355 steel and the slight increase of work for WR12. When the work was compared in the Z_2 and Y_2 directions, S355 required the same amount of sliding work regardless of the speed, whereas the amount of compressive work was changed. With the other steels, the increase of speed increased the compressive work, while for example for WR12 the sliding work decreased slightly. WR6 steels showed the

largest increase of the work in the sliding direction.

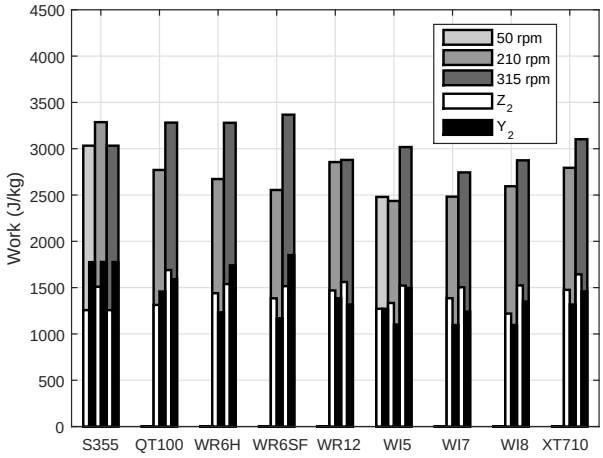

Figure 5.29: *Effect of speed on the comminution work. The white and black bars are the work conducted in the Z_2 and Y_2 -directions, and the gray bars are the total work of the tests at different speeds. Feed: 10 mm - 12.5 mm granite.*

5.1.3.2 Size distribution of the product

The size distribution of the product was not much affected by the different specimen materials. Figure 5.30 shows the average size distribution with $2\sigma_{st}$ errorbars. Also the softer QT100 steel produced a similarly comminuted product as the tool steel specimens. When the speed of the jaw crusher was increased to 315 rpm, the average curve shows that the product contains a smaller amount of larger rocks than in the 210 rpm tests. The speed of the crusher may also have an effect on the comminution rate, as the rock particles have less time for free fall between the compressive cycles.

5.1.3.3 Comparison of wear and work of the tool steels

Figure 5.31 a) shows the correlation between the volume wear rate and the accumulated work of the tool steels in the DPJC tests with 5°+5° jaw angles. The measured work in the WI5 tests with $\beta = 0°$ shows a deviation from the other test results, which was due to unsuccessful measurement of work caused by a faulty bearing. Also the WI7 and WI8 measurements were affected but were managed to be redone. Unfortunately there was not enough rocks of the same batch available to make new measurements also with WI5 specimens.
Both WR and WI steels show roughly the same dependence between wear and work, as indicated by the slopes of the drawn lines. Figure 5.31 contains also the results of QT100 and XT710 tested with similar parameters, as well as the results of the S355 steel from tests with the feed size of 12.5-14 mm. Compared to QT100, the larger rock size used in the S355 tests lead to a higher value of E_0. Both softer steels show a significantly steeper slope than the tool steels. XT710, on the other hand, has a slope closer to the slopes of the tool steels.

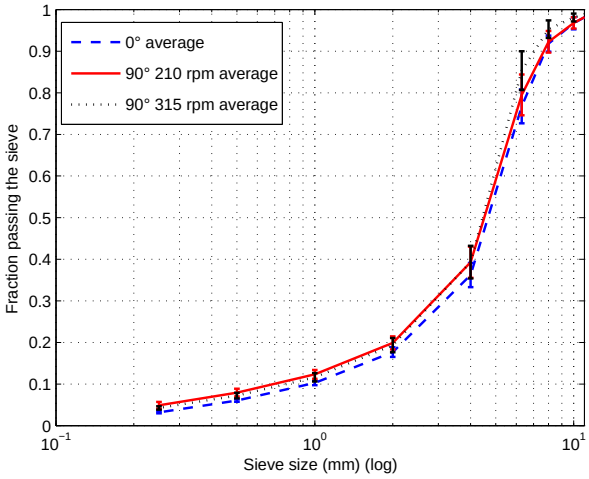

Figure 5.30: *Average product size distributions from the tests on tool steels. The error bars show the $2\sigma_{st}$ limits. Feed: 10 mm - 12.5 mm granite.*

Figure 5.31 b) shows the wear rate compensated by μ and the hardness of the deformed surface, where the slopes of the drawn lines are the dimensionless wear coefficient K from equation 2.44. This approach groups XT710 with the WI and WR steels with a definite difference to the softer steels.

The difference between the harder and softer steels is most likely arising from the fact that the contact forces between the rocks and the specimen remain more or less constant independent of the test material, whereas the wear depends highly on the test material properties. The contact forces are presumably limited by the mechanical properties of the rocks, which seem to be affected also by the amount of sliding work produced in the test. When a rock particle is brought into contact with the specimen and the approach is controlled by the displacement of the jaws, the rock particle penetrates or ploughs into the specimen material until the mechanical strength of the particle is overcome. The penetration depth and the possible volume of the removed material is dependent on the capability of the specimen material to resist the deformation, which is also measurable as the hardness. The softer the material, the more wear occurs as the rock properties are the limiting factor. The results of Figure 5.31 support the assumption that the rocks need a certain amount of energy E_0 to be crushed. This energy could be approximated from the compression test results. The addition of sliding movement causes an increase of work consumed in the test, where the work beyond E_0 shows a linear relation to the increased amount of wear due to sliding. The increase of work is most likely related to the sliding friction and other plastic and elastic interactions between the rock particles and the specimen materials, but only a tiny portion of this kind of deformation actually leads to material removal as wear debris. The probability of material removal depends highly on the contact geometry. The tests also show that the speed of the test affects the wear rate, which implies that the probability of material removal is dependent on the dynamic properties of the rock and especially of the test specimen, which manifests itself for example as localized shear banding of the wear debris.

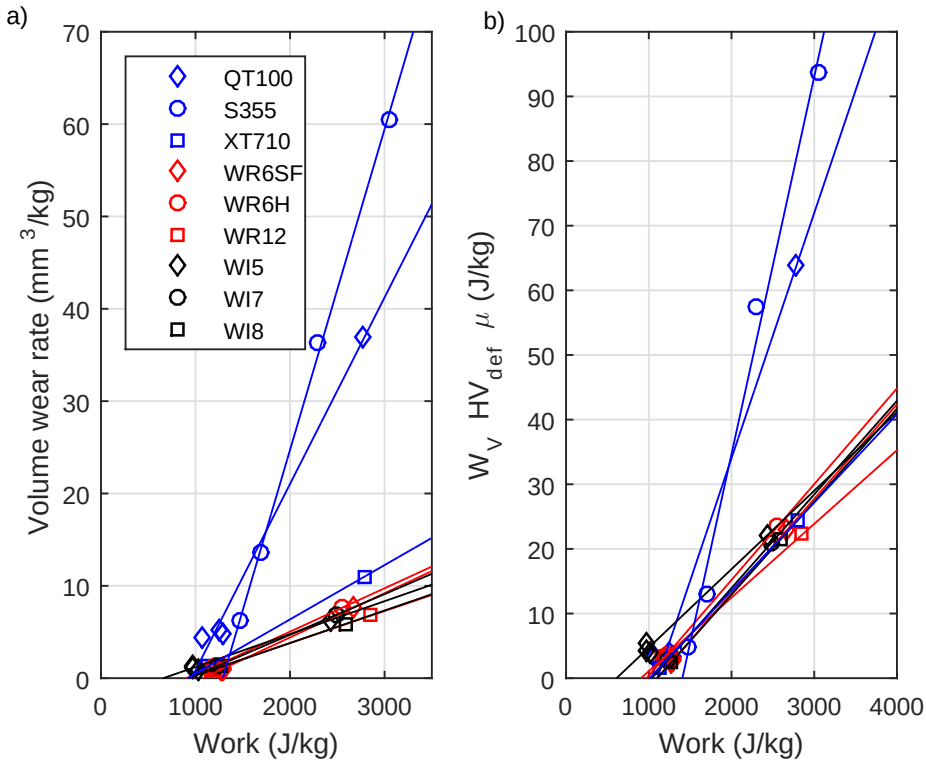

Figure 5.31: *a) Correlation between the wear rate and work of the test materials, b) correlation between the adjusted wear rate and the work of the test materials. Feed in QT100 test: 12.5 mm - 14.5 mm granite, in other tests 10 mm - 12.5 mm.*

5.2 Wear surface analysis

The wear surfaces of the jaw specimens were studied in order to determine the effect of the change in the test parameters, such as the β angle, on the surface topography and microstructure of the wear surface layer. The analysis also covers the examination of the wear debris from the tool steel test series.

5.2.1 S355 steel

Figure 5.32 shows the wear surfaces of the S355 steel specimens. The stereo microscope images were taken with two light sources positioned almost parallel to the left and right hand sides of the images. The method increases the contrast caused by the surface roughness. The centers of the images are approximately 30 mm from the minimum gap end of the specimen, which is towards the bottom of the images. The specimens from the $\beta = 0°$ tests showed the smoothest surfaces, which were almost identically rough and contained mostly elongated indentations instead of scratches. The $\beta = 45°$ tilt lead to similarly rough surfaces of the specimens with some longer elongated indents. The increased sliding movement of the jaws may have produced some indications of increased sliding wear in the Jaw2 wear surface, but no difference could be observed in the Jaw1 specimen, when compared to

the specimens of the tests with the $\beta = 0°$ tilt. The specimens tested with the $\beta = 75°$ tilt showed a clear difference between the roughness of Jaw1 and Jaw2 specimens, where the Jaw2 specimen showed more grooves on the wear surface. There was also a significant difference in the roughness of the surfaces, when compared to the wear surfaces produced in the tests with smaller amounts of sliding movement. The amount of wear in the Jaw2 specimen was intense enough to remove material from the wear surface to produce a shallow concavity to the most heavily worn region. The specimens from the tests with $\beta = 90°$ showed even a rougher surface with definite grooves on both Jaw1 and Jaw2 specimens, and also the concave shape of the Jaw2 specimen wear surface was increased.

The microstructures of the wear surface cross-sections were examined with SEM using 10° taper sections. Figure 5.33 shows the SEM images from a taper section close to the wear surface, which is seen in the top part of images a) and b). The rock particles have penetrated quite deep into the material and formed an intermixed layer, which has a depth of over 100 μm as calculated from the angle of the taper section using trigonometry. The rock particles and the steel matrix can form a lamellar-like structure, which is caused by the ploughing movement and eventual burial of the rock particles in the surface. Figures 5.33 c) and d) show cut sections of a larger rock particle still attached to the wear surface containing ploughed material and a formed lamellar structure in front of the particle. The ploughing direction in the images is from the right to the left.

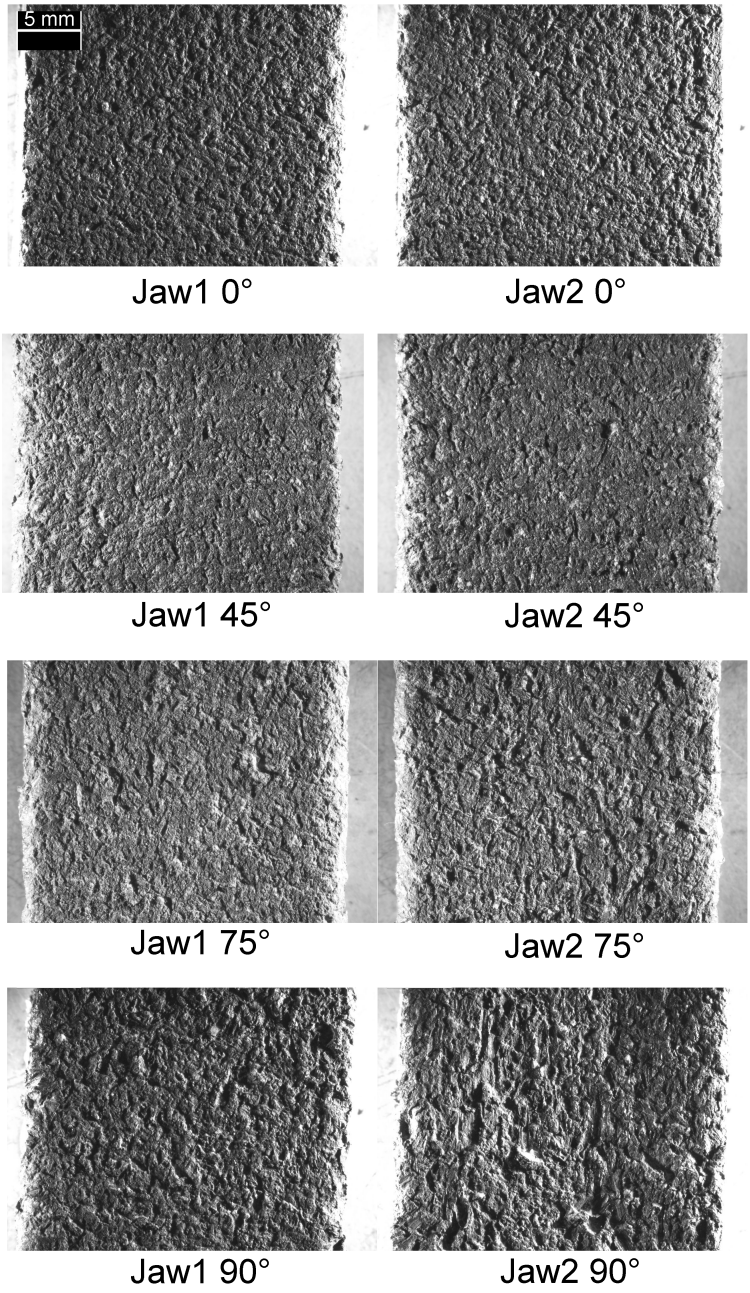

Figure 5.32: *Stereo microscope images of the wear surfaces of Jaw1 and Jaw2 S355 steel specimens at different β angles. Feed: 12.5 mm - 14 mm granite.*

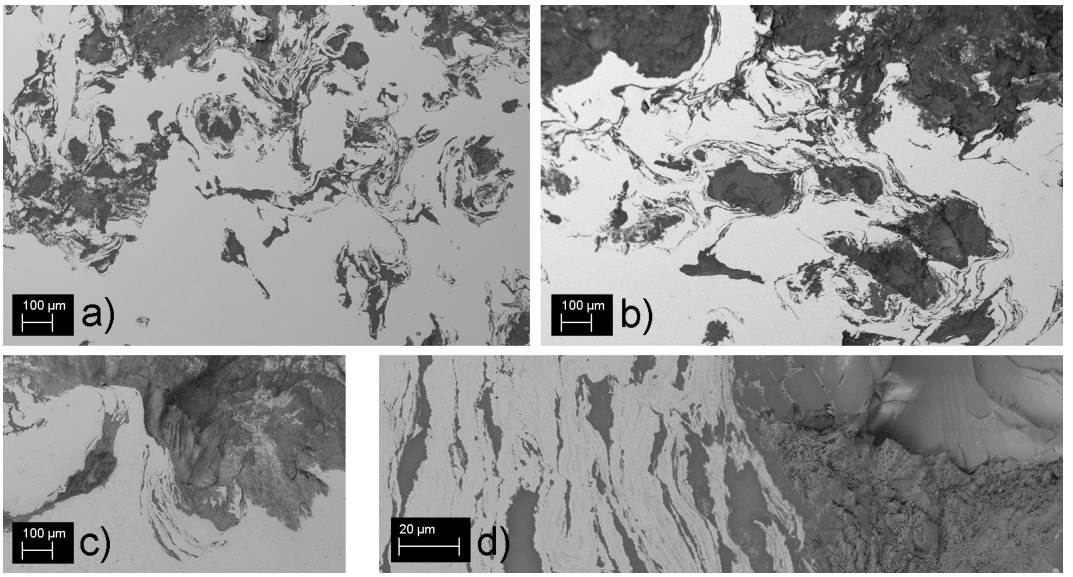

Figure 5.33: *SEM images from 10° taper sections of the wear surfaces, a) and b) intermixed layers of the wear surface at the top of the images, Jaw1 specimens with $\beta = 0°$ and 90°, respectively; c) and d) cut sections from a Jaw2 specimen tested with the $\beta = 90°$ tilt: a rock particle has been ploughing the surface from the right to the left. Feed: 12.5 mm - 14 mm granite.*

Figure 5.34 a) shows the original microstructure of the S355 steel before deformation and b) the lamellar microstructure after deformation. The surface has been etched with 2 % nital to reveal the pearlite and ferrite grain boundaries. Figure 5.34 c) is a close-up from b), showing that there are no gaps between the rock particles and the steel. The grain boundaries of the steel matrix flow around the elongated regions of the rock particles. There are no separate grains visible in the rock particles and the polished surface shows no visible cracks.

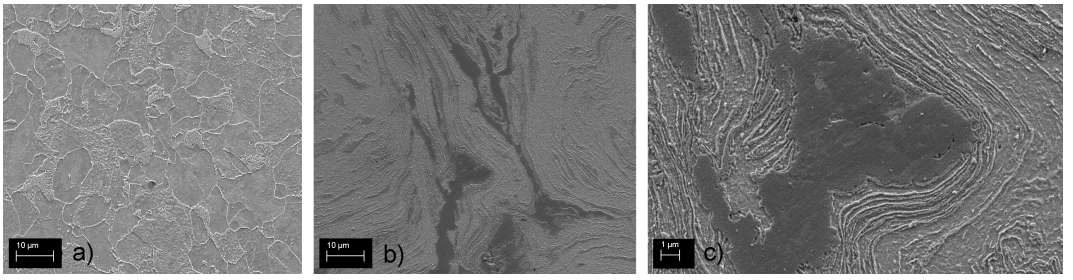

Figure 5.34: *SEM images from a) undeformed bulk microstructure of the S355 steel, b) etched microstructure of a Jaw2 specimen after deformation in a test with $\beta = 90°$, c) close-up from b), showing trapped rock particles in the steel matrix. Feed: 12.5 mm - 14 mm granite.*

The surface hardness was measured before the tests from the bulk material, and after the tests from the taper sections at locations, where the taper section meets the wear surface. The hardness measured from the taper sections was in average 279 ±19 HV1, 301 ±26 HV1,

294 ±29 HV1 and 315 ±35 HV1 for the Jaw2 specimens tested with $\beta = 0°$, 45°, 75° and 90°, respectively. The increase of hardness from the bulk value of 190 HV1 was moderate, but the hardness differences caused by the different amounts of sliding were quite small.

5.2.2 Manganese steels

Figures 5.35 and 5.36 show the $\beta = 90°$ tilt and Figure 5.37 the $\beta = 0°$ comparison of the specimen wear surfaces after the tests. The images are taken with a stereo microscope with a light source close to the plane of the wear surface and illuminating the surface from the right hand side of the image. The two images next to each other show the different ends of the specimen, leaving only a 1 mm region in the center of the specimen uncovered. Both Jaw1 and Jaw2 specimens are positioned so that the minimum gap end of the specimen is on the right hand side of the image. The indentations increase in size, also increasing the roughness of the wear surface towards the left hand side of the images. This is due to the opening angle of the jaws that allows only rocks with a size big enough to be crushed at the higher sections of the specimen. Also the number of rock contacts decreases towards the left hand sides of the images.

In Figures 5.35 a) and 5.36 a), the left hand sides of the specimens from Jaw1 with $\beta = 90°$ have an area where no severe contacts with the rocks have occurred. With the 10° opening angle, the gap between the specimen surfaces on the left hand side of the specimen in the images is from 16 mm to 19 mm with a 3 mm - 6.5 mm minimum gap, and 13 mm to 16 mm with 0 - 3 mm gap. This indicates that the marks on the left hand side of the images have been produced by several rocks being compressed together at the same time.

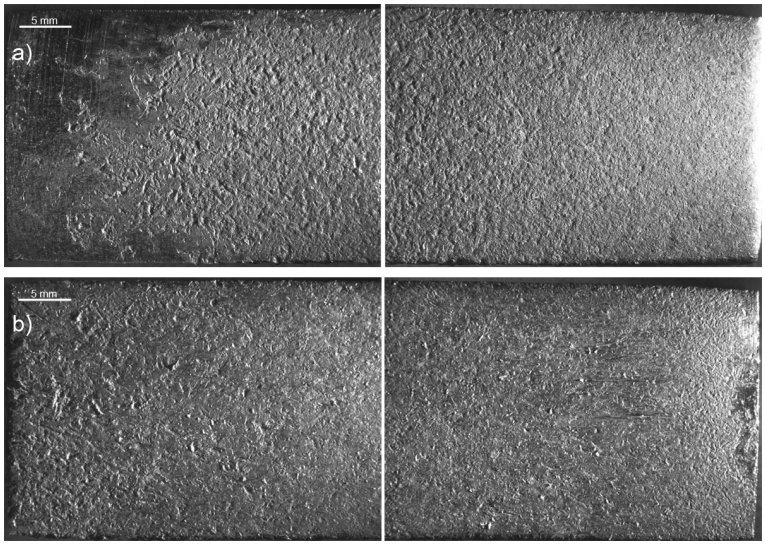

Figure 5.35: *Stereo microscope images of specimens tested with 5°+5° specimen angles and $\beta = 90°$ tilt, a) wear surface of the specimen in Jaw1, and b) wear surface of the specimen in Jaw2. The minimum gap ends of the specimens are on the right hand side of the images. Feed: 10 mm - 12.5 mm granite.*

A severely abraded region can be noticed in the specimens in Jaw 2 with the β =90° tilt.

Figure 5.35 b) shows that the region starts at about 10 mm from the minimum gap end of the 5°+5° specimen. Figure 5.36 b) shows the 12.5°+12.5° specimen, where the heavy sliding region begins at about 15-20 mm from the minimum gap end. During the tests it was noticed that the sliding region depends on the size of the rock as well as on the opening angle of the jaws. These factors determine where the most abrasive contacts occur.

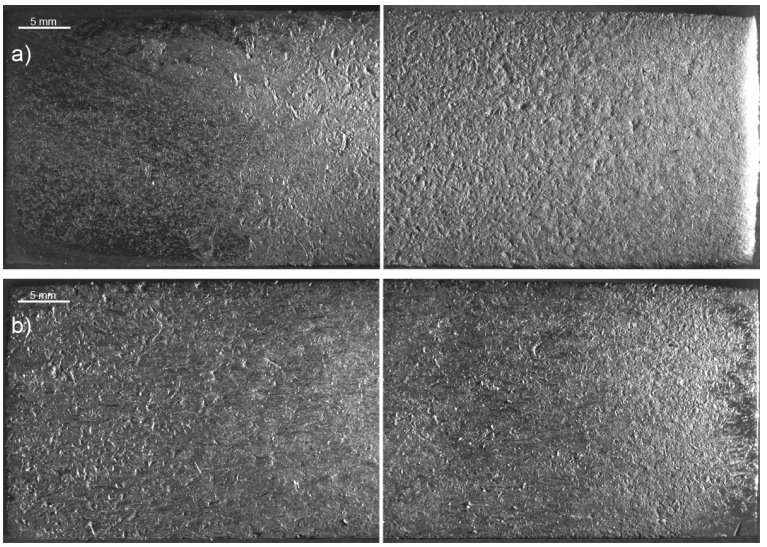

Figure 5.36: *Stereo microscope images of specimens tested with 12.5°+12.5° specimen angles and $\beta = 90°$ tilt a) wear surface of the specimen in Jaw1, and b) wear surface of the specimen in Jaw2. The minimum gap ends of the specimens are on the right hand side of the images. Feed: 10 mm - 12.5 mm granite.*

Jaw1 specimens in the tests with $\beta = 90°$ show rounded edges on the right hand side of the images, which is also the side of the minimum gap of the specimens. The other sides show edges with indentations, but the deformation is not sufficient to remove extensive amounts of material. The Jaw1 specimen edge roundness is caused by the movement of the jaws, where the specimen in Jaw1 lifts the rock along the specimen in Jaw2. This movement can cause rocks to become crushed with the edge of the specimen and sliding of the rocks over the edge. In contrast, the specimen in Jaw 2 has a region at the bottom of the specimen, where no wear has occurred. The roughening of the surface increases by a factor of 2-3 from the right hand side edge of the specimen towards the left hand side in Figures 5.35 b) and 5.36 b).

5.2.2.1 Surface hardness and microstructural examination

To examine the microstructural changes, taper sections with a 10° angle to the wear surface were prepared by grinding and polishing. The hardness profile along the prepared surface was measured 6-8 times up to 30-40 mm from the minimum gap edge of the specimens in 5 mm intervals. Figure 5.38 shows the depth profile for a 5°+5° specimen pair tested with the $\beta = 90°$ tilt and for a specimen in Jaw1 tested with the $\beta = 0°$ tilt. The 0.5 mm depth was reached at a distance of 2.87 mm from the intersection of the wear surface and the polished taper section. The intersection is parallel to the sliding direction of the jaws with a distance

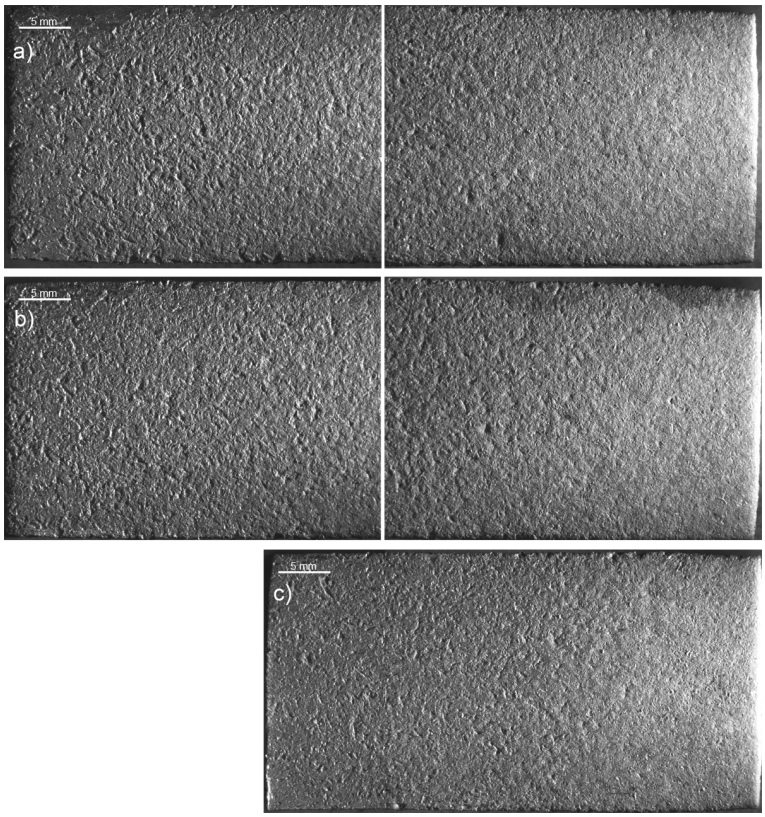

Figure 5.37: *Wear surfaces of specimens in Jaw2 tested with the $\beta = 0°$ tilt and jaw angles of a) 5°+5°, b) 10°+0°, and c) 12.5°+12.5°. The minimum gap ends of the specimens are on the right hand side of the images. Feed: 10 mm - 12.5 mm granite.*

of about 7 mm from the side edge of the specimen. The area closer to the side edge of the specimen can be of lower hardness compared to the middle of the specimen due to a smaller amount of contacts with the rocks, which can result in a lower amount of work hardening in the profile. However, the measured 0.5 mm depth of the deformed layer is sufficient to confirm that the DPJC device is capable of deforming the manganese steel. All specimens in Figure 5.38 show a hardness of over 600 HV5 near the wear surface. The Jaw2 specimen tested with the $\beta = 90°$ tilt shows a shallower hardness profile with the bulk hardness being reached at the depths of 0.3 mm. In contrast, the Jaw1 specimens tested with both test tilts show similar hardness profiles irrespective of the difference in the sliding movement between the jaws. The wide scatter of hardness in Figure 5.38 is caused by combining the results of several depth profiles with 5 mm intervals from the heavily worn region of the specimen. The lines show fitted average values of the depth profiles. The hardness of the Jaw2 specimen with 5°+5° specimen angles and the $\beta = 90°$ tilt was also measured with a 1 kg load from the sectioned surface from locations very close to the surface. The average surface hardness of 12 measurements was 702±56 HV1, indicating that at very shallow depths the surface hardness was high even in the Jaw2 specimen tested with the $\beta = 90°$ tilt.

The microstructures were examined with optical and scanning electron microscopy. Figures

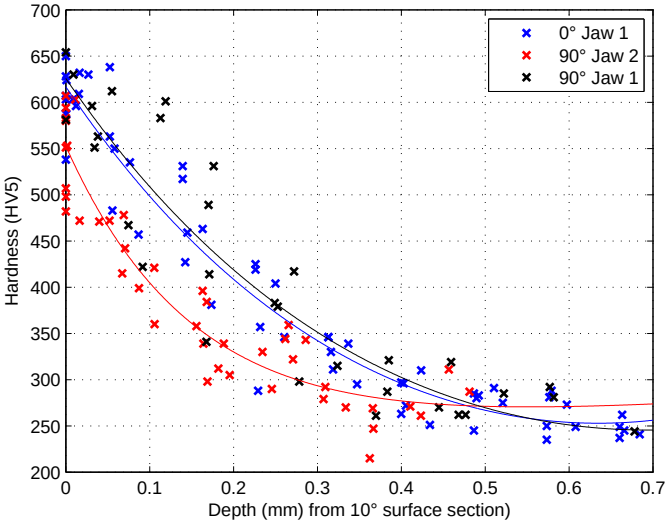

Figure 5.38: *Hardness profiles of the XT710 specimens from tests with 5°+5° specimen angles along the polished 10° wedge.*

5.39 and 5.40 show differential interference contrast images taken with an optical microscope. The dark areas on the right hand side are from the unpolished wear surface. The images show mechanical twinning inside the austenitic grains of the manganese steel. The grain boundaries of the large austenitic grains are also visible. In addition to twinning, another type of localized deformation can also be seen in the images. This deformation was identified to be macroscopic shear banding, which produces wider structures than the narrow twins. Electron Backscatter Diffraction (EBSD) was used to identify the possible phase transformation and deformation mechanisms. The examination found no signs of phase tranformation from austenite to martensite. Figure 5.41 contains an inverse pole figure EBSD map, which shows the orientation of the microstructure with colors denoted in the stereographic basic triangle on the right. The areas in the map where the EBSD identification was not successful are shown in gray color. The unidentified thin lines can be caused by mechanical twinning or by a packet of slipbands, and some parts of the lines where the EBSD-system has managed to acquire the actual orientation information are identified as twins with around $>55°$ misorientation to the surrounding lattice. A misorientation profile was taken along the line in the image that crosses the zig-zagging structure boundary. The profile shows quite sharp changes in the orientation with an angle close to 30°. The deformation is within one austenitic grain, and the grain returns to its original orientation with a long gradient on both sides of this feature. The profile also shows one $>55°$ twin boundary. The twins and the dark lines show bending at the point where the misorientation profile was taken, which suggests that twinning occurred prior to the saw-tooth shaped macroscopic shear band structure with 30° misorientation to the original lattice.

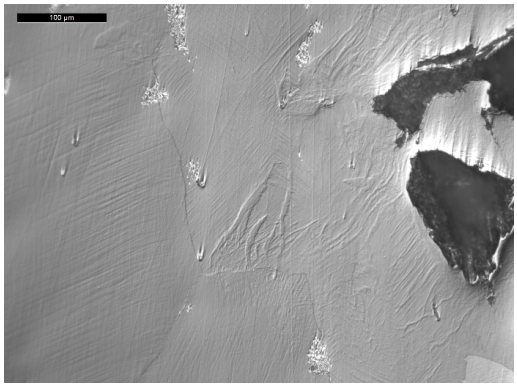

Figure 5.39: *Differential interference contrast microscopy image of a wide and twisted deformation mark in a Jaw2 specimen of XT710 steel tested with 5°+5° specimen angles using the $\beta = 90°$ tilt.*

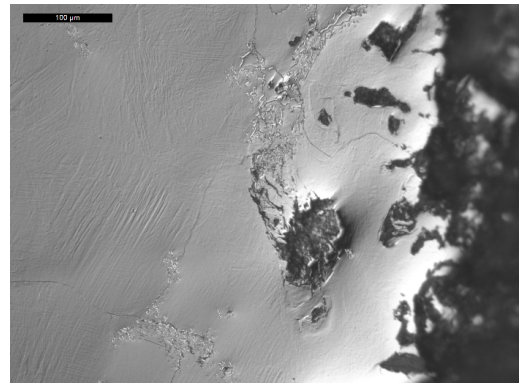

Figure 5.40: *Differential interference contrast microscopy image showing twinning of the microstructure in a Jaw1 specimen of XT710 steel wear surface tested with 5°+5° specimen angles using the $\beta = 0°$ tilt.*

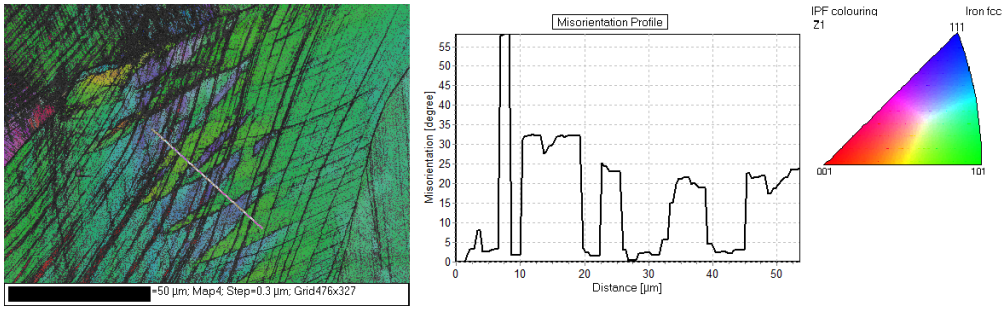

Figure 5.41: *EBSD Inverse pole figure map from a Jaw2 specimen tested with 5°+5° specimen angles and the $\beta = 0°$ tilt. The misorientation profile was taken along the white line drawn in the EBSD map.*

5.2.3 Tool steels

Several methods were used to obtain comparable information about the wear behavior of the tool steels. The wear surface hardness measurements were conducted after the higher speed tests on the specimens worn in the Jaw2 position using the $\beta = 90°$ tilt. The comparison also includes measurements taken from the stationary jaw specimens of the G81 tests. Surface profilometry was used to compare the wear surface roughness between the tool steels and between different DPJC and G81 tests. The wear surfaces and the wear debris were also examined with SEM to better reveal the geometrical and microstructural response of the test materials.

5.2.3.1 Surface hardness

The hardness of the wear surface was measured at various depths making use of the 10° taper section prepared on the specimens. The hardness was measured with 1 kg and 5 kg weights. Figure 5.42 shows the hardness depth profiles of the test materials measured at a 25 mm distance from the release end of the Jaw2 specimens. The hardness values measured with a 1 kg load in Figure 5.42 show higher values than the values measured with a 5 kg load, when taken from the same depth. The higher values with 1 kg are assumed to be due to the large hardness difference between the matrix and the carbide phase and the smaller indentation volume of the HV1 measurement, leading to a higher influence of the carbides on the measured values. The smaller indentation size also allowed the measurements to be taken much closer to the surface. The hardness profiles indicate noticeable deformation up to the depths of approximately 200 μm.

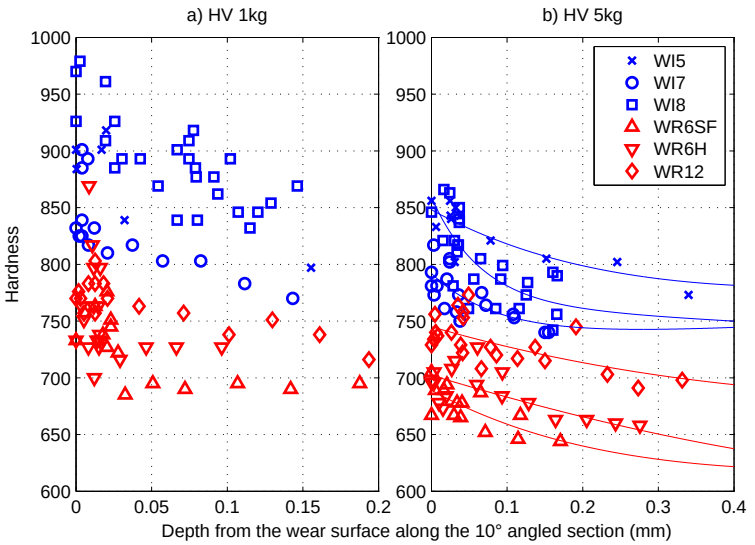

Figure 5.42: *Hardness profiles of Jaw2 tool steel specimens from the tests with $\beta = 90°$ measured with a) 1 kg load and b) 5 kg load.*

Table 5.2 shows the average hardness of the wear surfaces at the depth of 50 μm. The roughness and concavity of the wear surface, however, cause slight uncertainty in the depth measurements. Table 5.2 and Figure 5.42 show that the deformation increases the hardness of studied tool steels. WI8 showed the highest work hardening, increasing the hardness close

to the surface hardness of WI5, which had the highest bulk hardness of the studied steels. The high surface hardness of WI8 could also explain the lowest wear rate of the material. The comparison between the hardness of specimens tested with the $\beta = 0°$ and 90° tilt shows that the surface hardness of most steels is similar regardless of the sliding component. Only with the QT100 and WI5 steels the surface hardness differences of specimens was large enough to have significance with the change of the amount of sliding component.

Table 5.2 lists also the deformed hardness values of the wear surfaces from the G81 tests. The measurements were taken from the most worn region of the stationary jaw. The measurements with 1 kg and 5 kg loads yield quite similar wear surface hardness values for the Jaw2 specimens tested with the $\beta = 90°$ tilts and G81 tests, especially with the 5 kg load. The 1 kg load showed lower hardness for the WI5 and WI8 steels and higher for all WR steels, when the G81 test hardness values were compared with the DPJC test values. The differences may come from several reasons, in addition to natural variations. For example, the movements of the jaws are different, which could lead to different contact forces. In addition, the G81 test crushes larger sized morainal rock, which could introduce higher contact forces. Also the choked feed of G81 allows additional support for the rock particles from the adjacent particles, which could increase the compressive forces on the specimen surface. The temperature of the specimens was noticed to increase in both tests, which can have some influence on the resulting hardness. The rock was stored outside and was moist in the G81 tests, which could cause additional cooling of the specimen surfaces in the test. The warm specimens dried almost instantly after the G81 test was finished. The obtained results, however, cannot directly explain what is the true effect of all these factors. Nevertheless, the comparison shows that both wear test methods produce similar hardness values for the deformed surface of tool steels, especially when measured with the larger 5 kg load.

Table 5.2: *Average hardness and standard deviation of the deformed tool steel surfaces at the depth of 50 μm measured with 5 kg and 1 kg loads. The indentations were done at 10 mm and 25 mm from the release side end of the Jaw1 and Jaw2 specimens of the DPJC tests with $\beta = 0°$ and 90° tilts, respectively. The G81 specimen measurements were done on the most worn region of the stationary jaw.*

Material	Average HV1		Average HV5		
	DPJC 90°	G81	DPJC 90°	DPJC 0°	G81
QT100	399±27		353±21	300±29	
WR6SF	738±26	781±26	681±14	685±23	705±18
WR6H	756±43	777±32	694±15	665±19	715±9
WR12	774±14	798±16	743±15	734±30	749±10
WI5	915±70	880±23	840±17	802±17	832±10
WI7	843±33	866±22	781±20	767±16	790±16
WI8	927±34	884±26	825±30	816±25	841±16

5.2.3.2 Profilometry and roughness of the surfaces

The DPJC specimen wear surfaces were measured with Alicona Infinite Focus G5 profilometer as a 10 mm wide map over the full length along the centerline of the longer face of the specimens. Figure 5.43 shows the height maps for the WR6SF specimens in both jaws with the $\beta = 90°$ tilt. The right hand side is the release end of the jaws. The Jaw1 wear surfaces

showed mostly indentations that intensified towards the release end of the specimens. The wear in the Jaw2 specimen was localized to a region located 20 mm - 40 mm from the lower end of the specimen. The shape of the region was roughly spherical with the depth of concavity of around 300 μm - 400 μm. In comparison to the S355 steel specimens, the wear surfaces of the tool steels show similar features, but the concavity of the tool steel specimens in Jaw 2 was not visually as detectable as with the S355 steel.

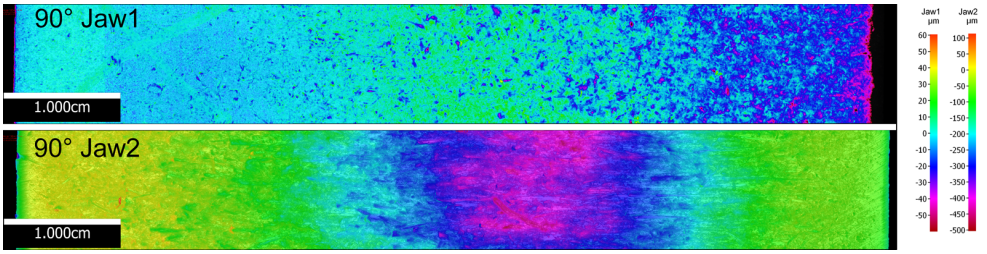

Figure 5.43: *Height maps of the WR6SF Jaw1 and Jaw2 specimens along the centerline of the specimen from a test with the $\beta = 90°$ tilt. The lower ends of the jaws are on the right hand side of the images.*

The overall shape or the primary shape of the Jaw2 specimen dominates the coloring of the height map, showing only the concave shape of the wear surface. With the primary shape all grooves have similar coloring. The primary shape yields information about the overall volume change of the specimen from a flat to a concave surface, as does the mass loss of the specimens. The primary shape can be used to assess where the wear has localized in the specimen. The roughness of the specimen is also interesting, as it yields information about the changes in the specimen surface in a microscopic scale. For the roughness of the test surfaces to be comparable, the specimen wear surfaces should be in the steady state wear region and the roughness value should not change with time. The primary shapes of the height maps were filtered in order to show the differences in the roughness of the specimens. The primary shape of the map was removed with the L_c filter value of 2500 μm, so that the sharp changes in the surface height remained. Figure 5.44 shows the filtered height maps of the WR6SF specimens from the tests conducted with the $\beta = 0°$ and 90° tilts.
Both the Jaw1 and Jaw2 specimens from the test with $\beta = 0°$ showed similar indentations of the rock particles. Also the Jaw1 specimen from the $\beta = 90°$ test was similar, whereas the Jaw2 specimen showed deep and long scratches. The height range of indentations in the Jaw2 specimen was twice the height range of the other maps. The deepest scratches shown in purple were almost 100 μm deep with the length of over 5 mm. The longest scratch on the surface near the lower end was over 12 mm in length, which is close to half of the 26 mm total sliding movement during the crushing cycle.

Figure 5.45 presents a comparison of the filtered height maps of WR and WI tool steel Jaw2 specimens tested with the $\beta = 90°$ tilt at about 30 mm from the lower end of the specimen. Overall, the WI steels exhibit shallower penetrations, shown with the purple color, than the WR steels. The direction of the grooves in the images is from right to left. The grooves usually become deeper when moving towards the left hand side of the image. The grooves can stop suddenly to a burr, where abrasion has been halted. Some burs in the WR6SF steel show heights of up to 50 μm, rising in front of the groove that is 100 μm deep from the L_c filtered zero level of the specimens. The WR6H steel shows multiple short and deep grooves. The green colored areas are above the zero level of the filtered surface. These regions have

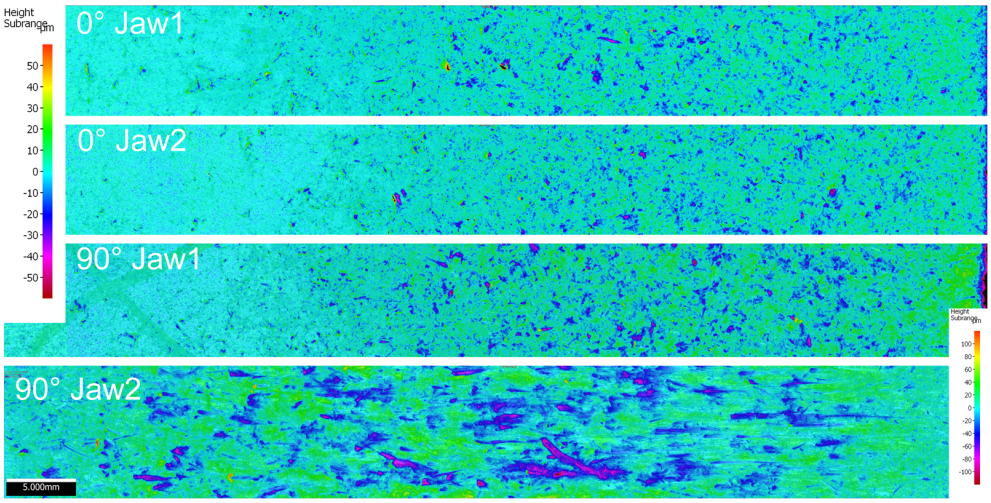

Figure 5.44: *Height maps of the WR6SF Jaw1 and Jaw2 specimens along the centerline of the specimen from tests with the $\beta = 0°$ and $\beta = 90°$ tilts. The lower ends of the jaws are on the right hand side of the images. The primary shape of the surface was removed to show the depth of individual scratches and indentations.*

more irregularly shaped profiles and contain also attached rock particles.

The visual surface height map comparison is at best only qualitative. Therefore, statistical measures need to be used for more accurate comparison. The roughness of the surface can give some useful information about the extent of interactions between the steel and the abrasives. The mean heights of the surfaces S_a were calculated from the surface maps after the L_c filter of 8 mm was used to remove the overall (primary) form from the maps. The S_a values were calculated from a 10 mm wide and 20 mm long area along the centerline of the DPJC specimen located between 15 mm and 35 mm from the release end of the specimens. The location was chosen as it represents the area showing highest wear in Jaw2 specimens in the tests with the $\beta = 90°$ tilt. The same location was also used for the Jaw1 specimens and for the specimens in the tests with the $\beta = 0°$ tilt. An area of the same size was also mapped from the stationary jaw specimens of the G81 tests along the centerline between 25 mm and 45 mm from the release end of the specimen. This location was selected as it represents a heavily worn concave region higher and wider than in the DPJC tests. Figure 5.46 shows a comparison of the S_a values between the Jaw1 and Jaw2 specimens of both axle tilt angles β, and the roughness of the stationary jaw in the G81 tests.

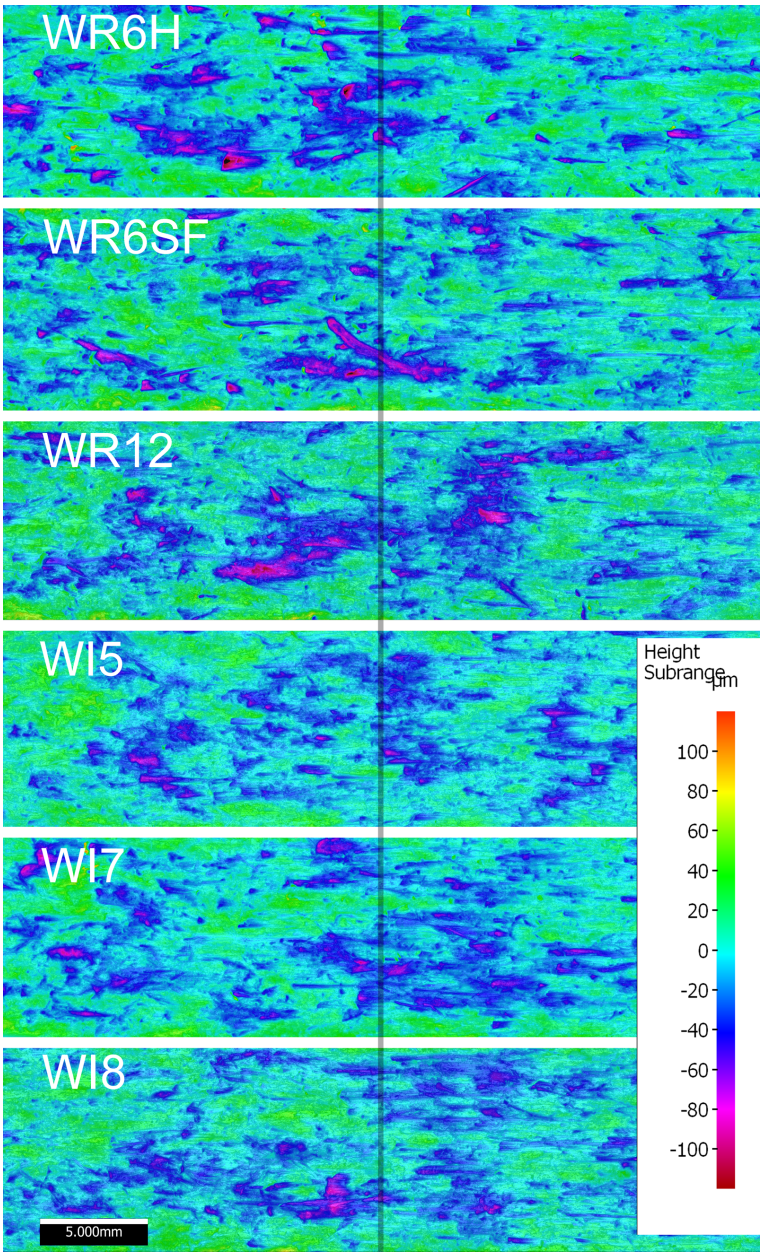

Figure 5.45: *Height maps of the Jaw2 tool steel specimens along the centerline of the specimen from the tests with the $\beta = 90°$ tilt. The lower ends of the jaws are on the right hand side of the image. The primary shape of the surface was removed to show the depth of individual scratches and indentations. The black line marks the 30 mm distance from the lower end of Jaw2.*

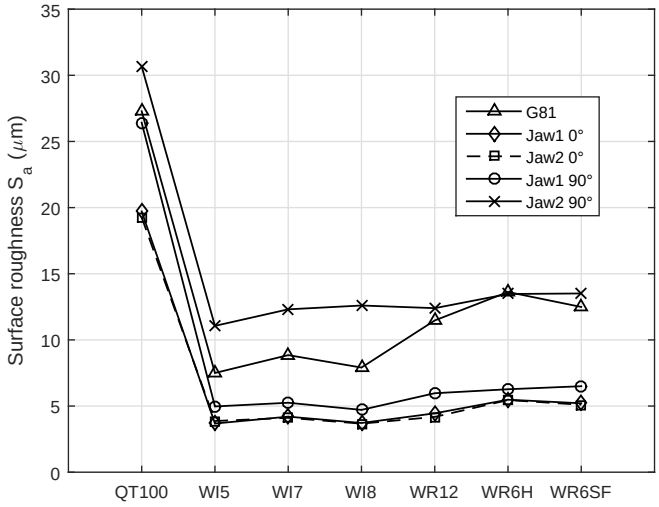

Figure 5.46: *Average surface roughness S_a of a 10 mm wide and 20 mm long area between 15 mm and 35 mm from the release end of the tool steel specimens in the DPJC tests, and from the most worn location of the stationary specimens in the G81 tests. The long wave components were cut with the L_c filter value of 8 mm.*

The Jaw1 and Jaw2 specimens yielded the same roughness values in the DPJC tests with the $\beta = 0°$ tilt, which are overlapped in Figure 5.46. The softer QT100 reference steel has a much higher average roughness than the harder steels. However, the increase in the roughness of the Jaw2 specimens in the tests with $\beta = 0°$ and 90° from 20 μm to 31 μm was only slightly higher than that with the harder steels, i.e., from 5 μm to 13 μm. Comparison of the tool steels shows highest roughness values for the WR6H and WR6SF steels of all DPJC test specimens. The roughness of WR12 was either at the same level or slightly lower than that of the WR6 steels. The WI series steels had a slightly lower surface roughness than the WR series steels. The WI5 steel had the lowest roughness of the Jaw2 specimens in the tests with the 90° tilt, being also the hardest steel of the test series. However, in more compressive crushing with the $\beta = 0°$ tilt, including also the Jaw1 specimens in the tests with the 90° tilt, the WI8 steel shows the lowest average roughness.
The stationary jaw specimen roughness of the G81 tests can be best compared to the Jaw2 specimens of the DPCJ tests with the 90° tilt. The roughness of the WI series steels was much lower than that of the WR steels, which were at the same level as the roughness of the Jaw2 specimen in the DPJC tests. The lower roughness of the WI steels could be explained by the higher hardness of the steels, but the effect of higher hardness on the surface roughness was not as big in the DPJC tests. The lower wear ratios of the WR steels in the G81 tests indicate better wear resistance than for the WI steels, which is in contrast to the measured roughness values.

All Jaw1 specimens tested with the $\beta = 90°$ tilt show higher roughness than the specimens tested with the $\beta = 0°$ tilt, where the relative increase was around 30 % with all steels. The higher roughness can be correlated to the overall higher wear rate of the specimens when compared to the tests with the $\beta = 90°$ tilt. Similarly, the higher wear of the Jaw2 specimens in the tests with the $\beta = 90°$ tilt correlate with the higher roughness. The relative increase

of roughness between the Jaw2 specimens tested with $\beta = 90°$ and $\beta = 0°$ is higher with the tool steels than with QT100, which showed a high roughness also in the compressive tests. Figure 5.47 presents the correlation between roughness and volumetric wear rate of the WR, WI and QT100 steels.

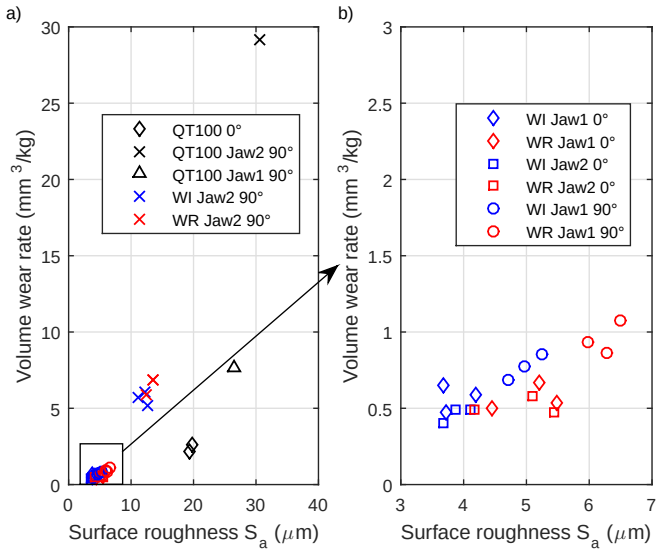

Figure 5.47: *Relation of the wear rate and the average surface roughness Sa measured from a 10 mm wide and 20 mm long area between 15 mm and 35 mm from the release end of the tool steel specimens tested with the DPCJ. The long wave components were removed with the L_c filter value of 8 mm. Comparison of Jaw1 and Jaw2 specimens of the QT100, WI, and WR steels tested with the $\beta = 0°$ and $\beta = 90°$ tilts, where b) is a close-up from the highlighted square in a).*

Figure 5.47 a) shows that the QT100 markers differ quite much from the WR and WI series markers, which are grouped closer together. The locations of the QT100 markers indicate exponential relationship between the increasing wear and roughness. Thus, the increase of roughness due to the increase of sliding movement may not be linear, but the roughness of the surface saturates to some level. In that respect, the amount of sliding does not seem to be as important to the measured surface roughness, whereas the increase of load on the indenting particle of higher strength could produce deeper indentations and further roughen the surface. Therefore, both the roughness and wear can be seen to depend on the load and mechanical properties of the feed. Figure 5.47 b) shows a linear increase of wear with increasing roughness for both WR and WI steel specimens receiving compressive crushing. The Jaw2 specimens in the tests with $\beta = 90°$ showed a much higher wear rate when compared to the results shown in Figure 5.47 b).

The WR series steels show higher roughness and higher wear rate values compared to the steels of the WI series. It is reasonable to expect that higher hardness and lower wear rate of the WI series cause also lower surface roughness on the specimens. Figure 5.48 compares the surface roughness and wear of the WR and WI steels normalized with the results of the QT100 reference steel tests with the same axle tilts and jaw angles. The G81 test results are also shown using the wear ratio defined in Equation 4.1, and alternatively as the relative

wear and surface roughness of the stationary jaw test and reference specimens used in the same test. This comparison of stationary jaws is not directly comparable to the Jaw2 specimen wear conditions, as the amount of jaw movement was different and the counterbody of the opposite plate was not of similar material. The direct comparison of stationary jaws produces higher relative wear for the WR and WI steels with the exception of WR12 steel.

The Jaw1 and Jaw2 specimens of the DPJC tests with $\beta = 90°$ seem to follow linearity with a slope value of 0.5, whereas the tests with $\beta = 0°$ show much higher relative wear with respect to their surface roughness because of the relatively low wear of the QT100 reference samples in the tests. The grouping of the results is close to unity, where the relative increase of roughness correlates to the amount of relative wear. The comparison of the G81 test results shows the controversial behavior of the WI and WR series steels, where the decrease of wear causes an increase of the surface roughness.

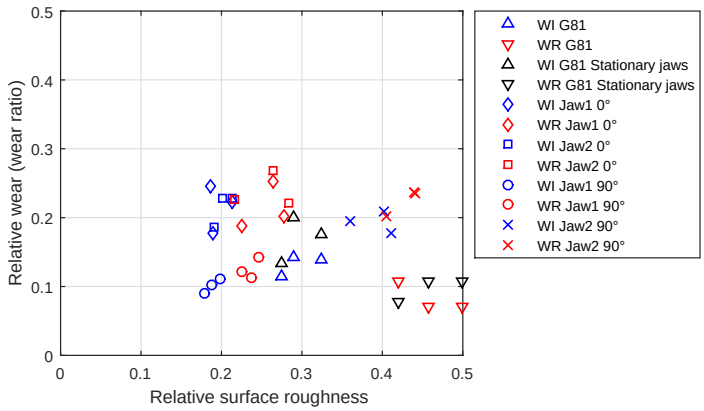

Figure 5.48: *Relative wear and surface roughness with QT100 as the reference of Jaw1 and Jaw2 specimens of the WI and WR series steels from the DPJC tests with the $\beta = 0°$ and $\beta = 90°$ tilts and of the stationary jaw specimens from the G81 tests.*

5.2.3.3 Wear surface examination

A scanning electron microscope was used to examine the wear surfaces of the tool steel specimens tested in the Jaw2 position. Figure 5.49 shows the compo-mode backscatter electron images (BSE) of the wear surfaces of WI test series samples. The 10° taper sectioned surface is shown at the top of Figures 5.49 a), b), d), g), and i). The sliding direction of the rocks in all images is from the right to the left. Figure 5.49 shows the wear surface of the WI5, WI7 and WI8 steels. The compo-mode of the BSE detector reveals the darker chromium carbides in the whiter metal matrix. The darkest contrast is produced by the rock particles that are adhered to the wear surface with a force high enough so that the surface cleaning was not able to remove them. In all WI steel samples the carbides were fracturing, especially the larger carbides in the WI5 steel. Also the metal matrix showed fracturing along and through the chromium carbides, as shown in Figure 5.49 i) for the WI8 steel specimen.
Figure 5.49 c) shows a shallow sliding groove on the wear surface of a WI5 steel specimen with broken carbides. The bottom of the groove is quite smooth with a couple of irregular

steps that are perpendicular to the sliding direction of the rocks. In this image there are no visible cracks, whereas there are plenty of cracks in Figure 5.49 b). The marks indicate a high degree of plasticity in the materials while being abraded by the rock particles.

Figure 5.49 h) shows a wear surface with protruding carbides. This surface shows that the carbides could protect the material from penetrations, but presumably the matrix is worn between the carbides due to the contacts with the rock particles. The hardness of the chromium carbides is higher than that of the mineral phases of the Sorila granite, which can cause abrasion and dulling of the protrusions of the rock particles. Figure 5.49 e) is a BSE image of a WI7 steel wear surface, showing a groove with broken carbides at the same level as the matrix. Apparently, the higher hardness of the chromium carbides is not sufficient to protect the matrix in every contact with the abrasives.

The wear surfaces showed some interesting marks of interactions with the sliding rock particles. Figure 5.49 f) is a BSE image with topographic contrast, showing a groove with a repeating wavy pattern. A closer examination revealed no fracturing of the surface between the undulations, which begin to occur after the rock particle has travelled a distance of approximately 50 μm on the wear surface.

Figure 5.50 shows the specimen surfaces of WR series steels after being worn in the Jaw2 position in a test with $\beta = 90^\circ$ and speed of 315 rpm. The polished taper section of the wear surface is seen at the top side of images b), c), d), f), g) and h). The sliding direction of the rock particles is from the right to the left similar to Figure 5.49. The images are compositional contrast mode BSE images with an exeption of Figure 5.50 i), which is a topographic contrast image showing also the wavy pattern on the surface of a groove similar to 5.49 f). The wavy pattern repeats itself with a distance of 20 μm. The larger sized vanadium carbides in WR6SF show marks of fracturing in Figures 5.50 b) and c), and the matrix shows small cracks progressing from one carbide to another. However, the surface deformation appears plastic and ductile, and the steel matrix can form prows and push material to the sides of the grooves, as in Figures 5.50 g) and h). Fracturing of the surface can be found at the bottom of the groove in Figure 5.50 e). There are also brittle fracture marks in the steel matrix in the center and the left hand side of the image. Figure 5.50 f) shows an extensive scratch mark that is 3 mm long and 600 μm wide. The scratch is quite shallow and ends to a fractured rock particle still attached to the steel surface.

Images of wear surfaces of the QT100 steel are shown in Figures 5.51 c), f) and i). The wear surface is rough, similar to the S355 steel. The deformation hardening of QT100 was higher than that experienced by the S355 steel, but the surface hardness was still much lower than the hardness of most of the mineral phases of Sorila granite. Figure 5.51 c) is a compo-type BSE image showing the attached rock particles as a darker color and the steel matrix as a lighter color. In the middle of the image there is an attached rock particle in a deep indentation. Supposedly the scratch marks on the left hand side of the particle are produced by the remaining protrusions of a larger rock particle after the smaller particle has broken off. Figure 5.51 f) shows the polished section at the bottom of the image. The upper side of the image shows a groove mark that has the same dimensions as in Figure 5.50 f). The groove seems to exist higher on a surface than the indentation marks at the center of the image. Figure 5.51 i) shows intermixing of the rock particles and steel, also having a lamellar structure similar to the rock interaction in the S355 steel. In contrast, the tool steels did not show definite deep intermixing of rock particles with the steel matrix.

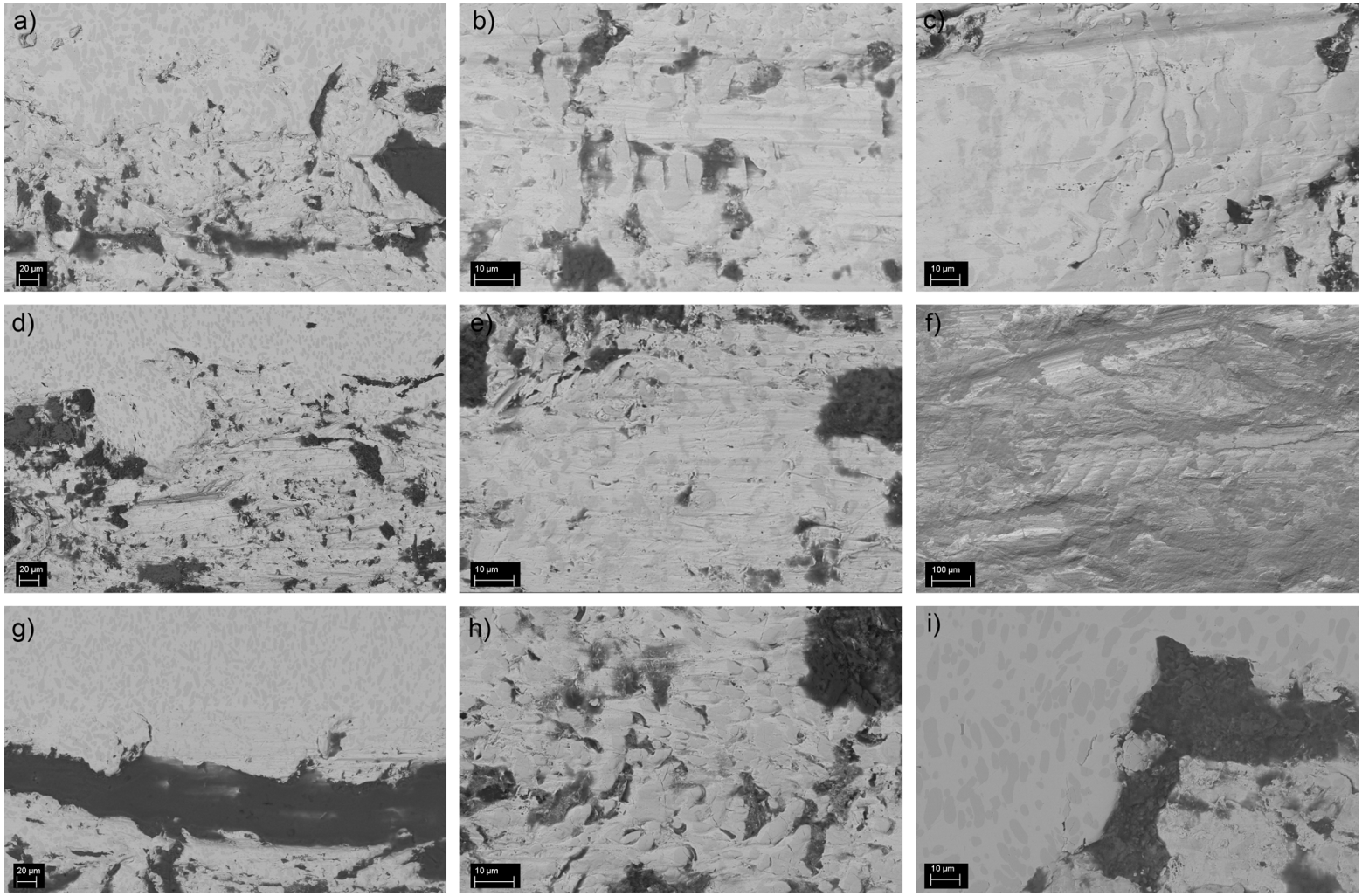

Figure 5.49: *BSE SEM images of the Jaw2 specimen wear surfaces of WI5 (a), b), c)), WI7 (d), e), f)), and WI8 (g), h), i)) from the tests with the* $\beta = 90°$ *tilt.*

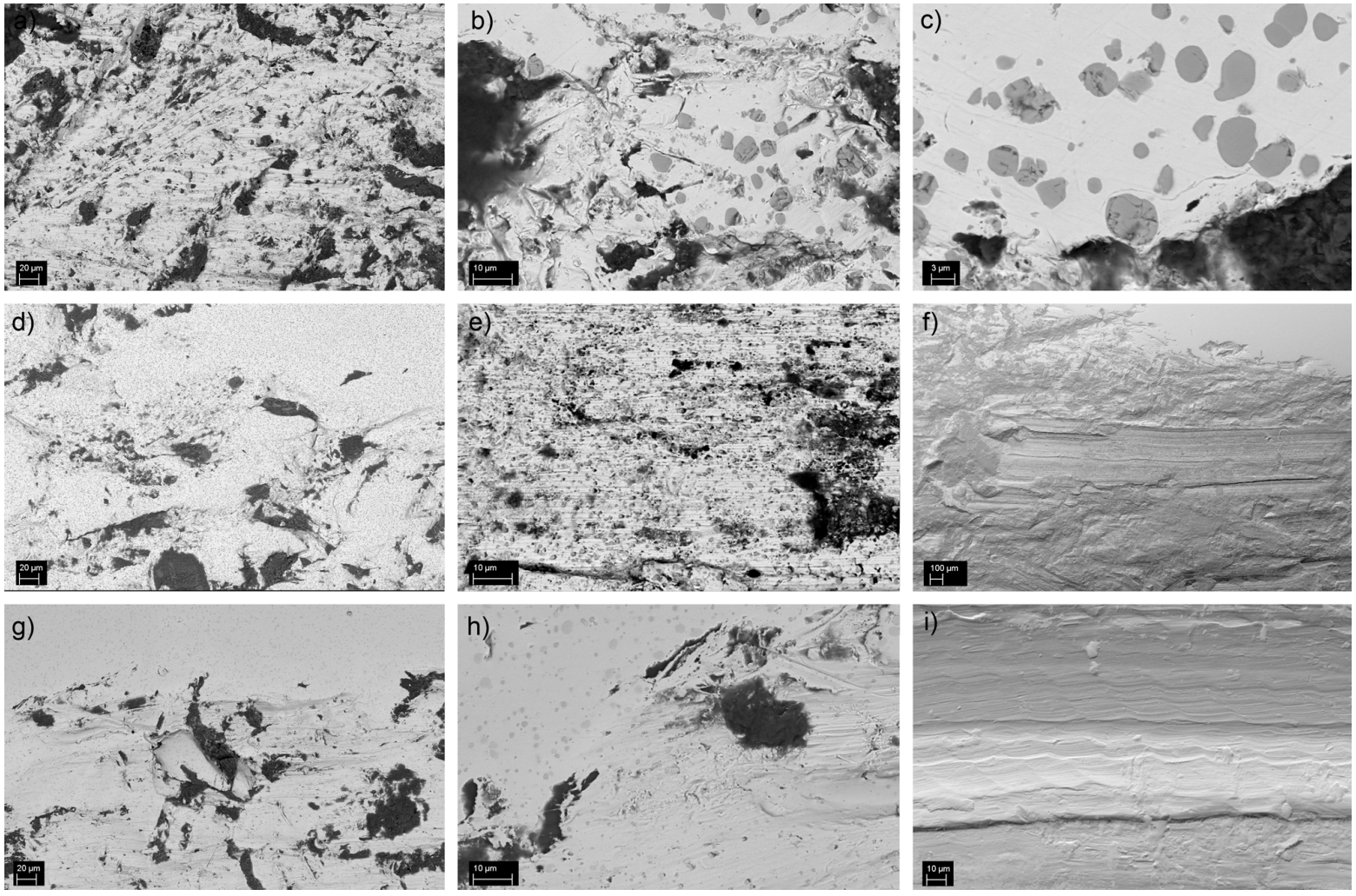

Figure 5.50: *BSE SEM images of the Jaw2 specimen wear surfaces of WR6SF (a), b), c)), WR6H (d), f), g)), and WR12 (g), h), i)) from the tests with the* $\beta = 90°$ *tilt.*

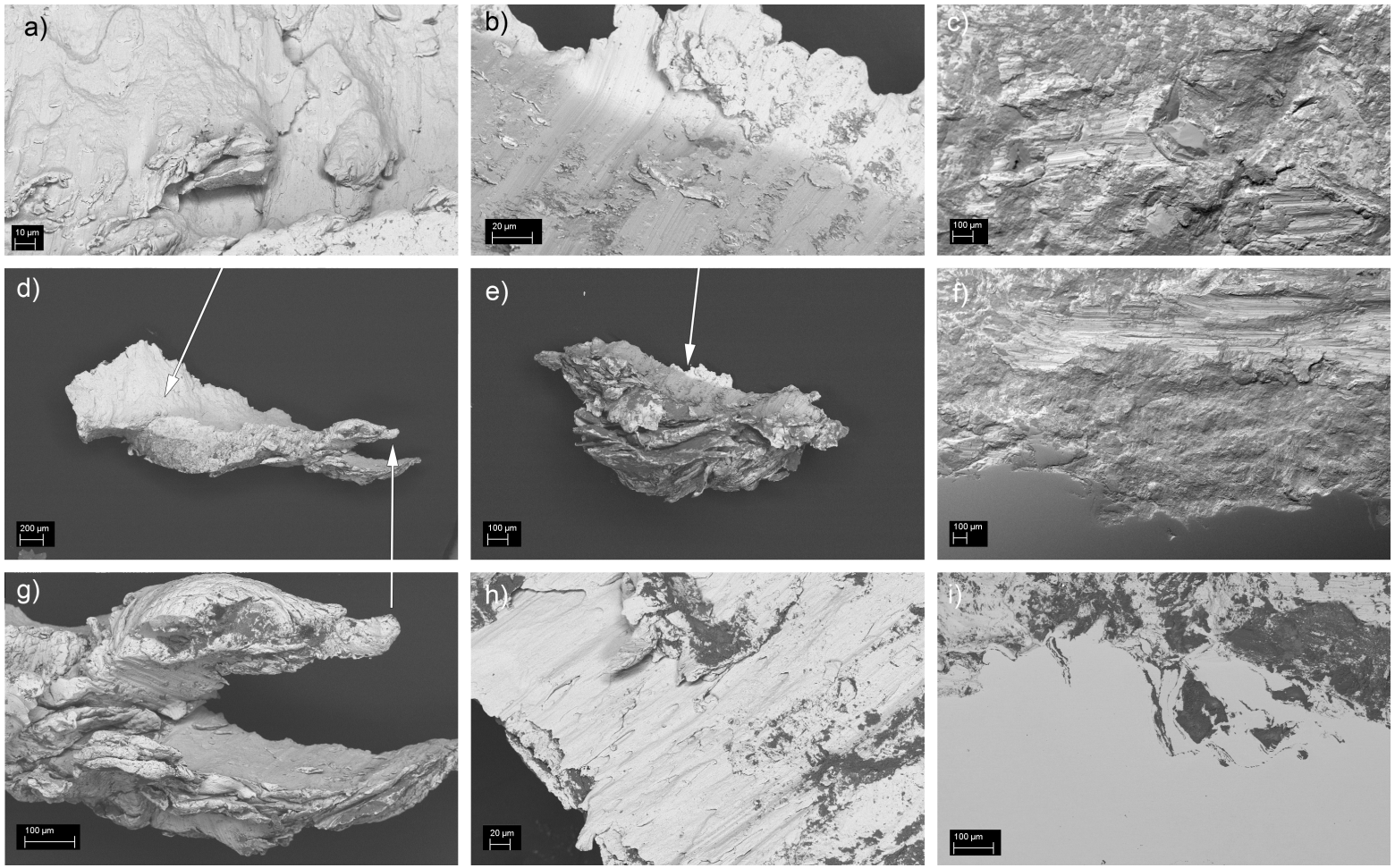

Figure 5.51: *Wear debris originated from the QT100 specimens in a DPJC test with the $\beta = 90°$ tilt and speed of 315 rpm (a), b), d), e), g), h)). Wear surface of the Jaw2 specimen is shown in c), f), and i).*

5.2.3.4 Wear debris examination

A magnet placed under the specimen holders was used to collect the falling debris during the tests. The wear debris were examined by SEM, showing particles that were mostly small and flaky. Figure 5.52 a) shows a sample of small sized wear debris collected from a test with WR6SF specimens. The debris consists of small metallic flakes and irregular shaped metallic particles, as well as of rock particles with an adhered layer of steel. Not all metallic debris originates from the specimens. The rock particles could also contain metallic debris from the previous events of crushing in the quarry. Also, the metallic particles can wear out from the specimen holders and from the metallic side plate of the testing device. For this reason, the SEM energy dispersive spectroscopy (EDS) analysis was used to identify the chemical composition of the wear debris. Figure 5.52 b) shows a larger sized rock particle with a layer of metal on the surface from a test with WI8 steel specimens. The close-up image from the edge of the metal layer shows that there appear to be no gaps between the metal and the rock particle. The surface of the rock particle contains groove marks with a width corresponding to the size of the carbides in the WI8 steel.

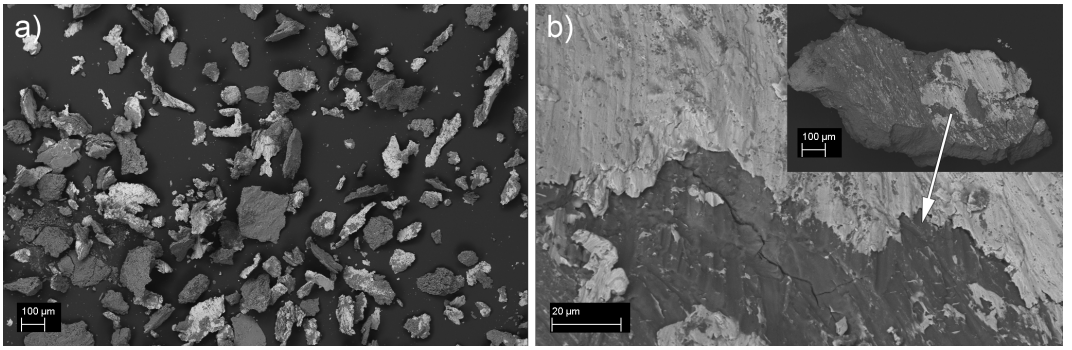

Figure 5.52: *a) small wear debris collected with a magnet during the DPJC tests with the $\beta = 90°$ tilt and WI8 steel specimens, b) a larger rock particle with adhered layer of steel.*

The sliding movement of the jaws in the tests with $\beta = 90°$ produced also wear chips originating from the cutting movement. Some of the chips were oxidized, showing tempering colors of steels. Figure 5.53 shows a chip from a WR6SF specimen that exhibits tempering colors from yellow to blue due to the varying thickness of the oxide layer. In tempering, the yellow to blue colors are produced in the range of 200-300°C, respectively. However, the thickness of the oxide layer is also dependent on the time and the composition of the steel. In tempering, the time of forming the oxidation layer is usually tens of minutes, which is much longer than the rapid heating and cooling time of a small chip. Therefore, it can be assumed that the colors are produced at higher temperatures than the corresponding colors produced in the tempering process.
Figures 5.51 d) and e) show some larger wear debris from the tests with QT100 specimens. Usually the debris was irregularly shaped, as in Figure 5.51 d), and only one definite cutting chip shown in Figure 5.51 e) was found. However, both of these debris particles show an oxide layer build-up, which are more visible in the close-up images in Figures 5.51 g) and b). The oxide layer shows as a darker colored surface in the BSE image. The close-up images in Figures 5.51 a) and h) show extensive plastic flow and shear marks.

Figure 5.54 shows a selection of wear debris from the tests on WI steels. Only the chips

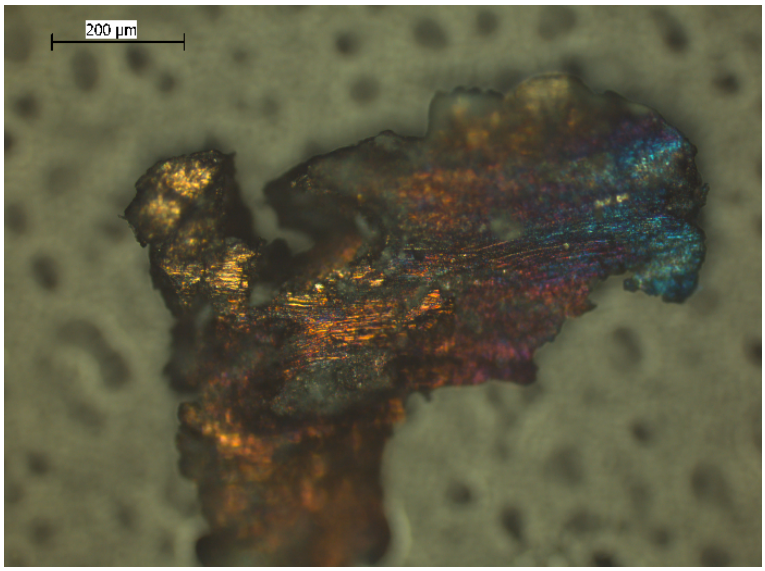

Figure 5.53: *Wear debris originating from the WR6SF steel in a test with $\beta = 90°$. The oxide layer build-up at a high temperature from of the chip cutting process is coloring the metal surface similar to the colors occurring in the steel tempering process.*

showing tempering colors were selected for the comparison. These chips are also the largest wear particles that could be recognized to originate from the WI steels. Figure 5.54 shows the debris from the WI5 steel. The chips have a serrated profile, where the inner surface of the curving chip has a sawtooth-like profile. The serrated look is caused by the deformation localizing in shear bands due to adiabatic heating [86]. At slow speeds the chips usually have a uniform thickness and also the deformation is uniform. The appearance of the chip depends on several factors such as the cutting speed, the mechanical and thermal properties of the material, as well as the geometry and depth of the cut [140]. Figure 5.54 b) shows also cracks on the surface of the chip, found frequently in the chips of the WI5 steel. The wear debris of the WI7 and WI8 steels are shown in Figure 5.54. Although cracks appeared in the WI7 and WI8 chips, as can be seen in Figure 5.54 h), their number was much smaller than in the chips of the WI5 steel. Figure 5.54 e) shows flakes of the saw tooth profile with quite sharp edges and slightly curved surfaces. Figures 5.54 c), d) and g) show that individual flakes can be several hundreds of micrometers wide. The chip can also have a quite irregular width with one chip splitting to several ends. This can partly be caused by the brittleness of the chips, where some parts of the chips are broken off. The chips can easily fracture during the specimen handling. The fracture surface of a cooled chip shows a much more fragile profile, which supports the assumption that the plastic deformation of the chip has occurred at higher temperatures. Figure 5.54 e) shows a brittle fracture surface at the end of the chip on the left hand side of the image.

Some of the chips, for example in Figures 5.54 f) and i), show a wavy profile on the smooth outer surface with a roughly same distance of repetition as the saw tooth profile found on the opposite side of the chip. Also the width of the undulations is in the same range found on the Jaw2 specimen wear surfaces, i.e., in Figure 5.49 f). The outer surface of the chip in Figure 5.54 g) shows a quite irregular surface profile. A line of darker contrast is also visible, which could be caused by the build-up of an oxide layer due to high temperatures

in the same manner as in Figure 5.51.

Figure 5.55 shows chips cut from the WR6SF, WR6H and WR12 steels. The chips have a size and shape similar to the chips from the WI steels. There are, however, very few visible cracks on the surfaces of the WR steel chips. Figures 5.55 d) and e) show the same chip at two different magnifications. The right hand side of the chip is narrower and contains smaller serrations. The darker contrast of the opposite surface shows the oxide layer on this side of the chip. The oxide layer is again deposited on certain areas of the surface, where for example the wider left hand side of the chip shows surfaces with lighter contrast indicating much less oxidation. Figure 5.55 d) shows a close-up of the image in Figure 5.55 c) with quite thin steps of deformation. The deformation of the chip has caused several small and thin layers to form steps. Between the steps there is one very long deformation step which also has a shifting contrast, indicating a change in the thickness of the oxidation layer. Presumably the small steps indicate more uniform deformation, which might be in the limit of causing localized shearing, while the large step is already caused by shear localization. Figure 5.55 i) shows the outer surface of a WR12 steel chip. The otherwise smooth surface contains steps occurring along the sliding direction of the chip. These steps could have been formed either by interaction with the rock surface, or by the interaction between the shearing planes, where the increase of temperature causes shear between metal surface instead of sliding of steel along the surface of a rock particle.

The scratch marks on the wearing specimen surfaces were several hundreds of micrometers wide, which could indicate that the thin and wide chips are formed in front of the sliding rock particle with a face perpendicular to the sliding direction. The original size of the rock particles is much larger than the size of the grooves, as only a small part of a rough particle can interact with the specimen surface. The thinner chips can be caused either by smaller rock particles or by protrusions in the rock particles with the cutting face making an angle with the sliding direction. The ploughing or cutting movement of the particle is moving the steel material more towards the sides of the rock faces, which can cause side wall removal by cutting or fracturing. Figures 5.55 a) and g) show narrower chips that could have been formed by the rock particle cutting the material towards the sides.

Some of the chips cut from the WR6SF steel were cross-sectioned to determine the changes in the microstructure. Figures 5.56 a) and b) show optical images of two cross-sectioned chips, while d), e) and f) are SEM BSE close-up images from the chip in a). Both chips were etched with 2 % nital to show the effects of deformation on the microstructure. The specimens were coated with gold by sputtering before SEM examination. Figure 5.56 c) shows the bulk microstructure of WR6SF at the same magnification as in Figure 5.56 f). The image is obtained with EBSD, and the contrast of the matrix is from the quality of the EBSD pattern (Band Contrast), revealing the individual tempered martensite laths.

The cross-sections show the irregular saw-tooth profile of the chips. Each of the teeth is produced by localized shearing instead of fracturing. Figure 5.56 d) shows the deformed microstructure, where etching has attacked the grain boundaries of the ferritic steel matrix. The flow marks of the material appear to evade the vanadium carbides that are mostly intact. Presumably the flow marks show the elongation of the grain boundaries of the tempered martensite laths. The thinner the width of the deformed lath is, the higher the strain has been. The thinnest flow marks appear between the teeth in bands where the shearing has been strongest. The higher the deformation of the shear band, the closer the flow marks are and the less details can be seen. Figure 5.56 f) shows a narrow shear band, which ends in the gap between two teeth. The microhardness of the matrix was measured from the chips with a 0.1 N load. The average hardness of 17 measurements was 1068±146 HV0.01,

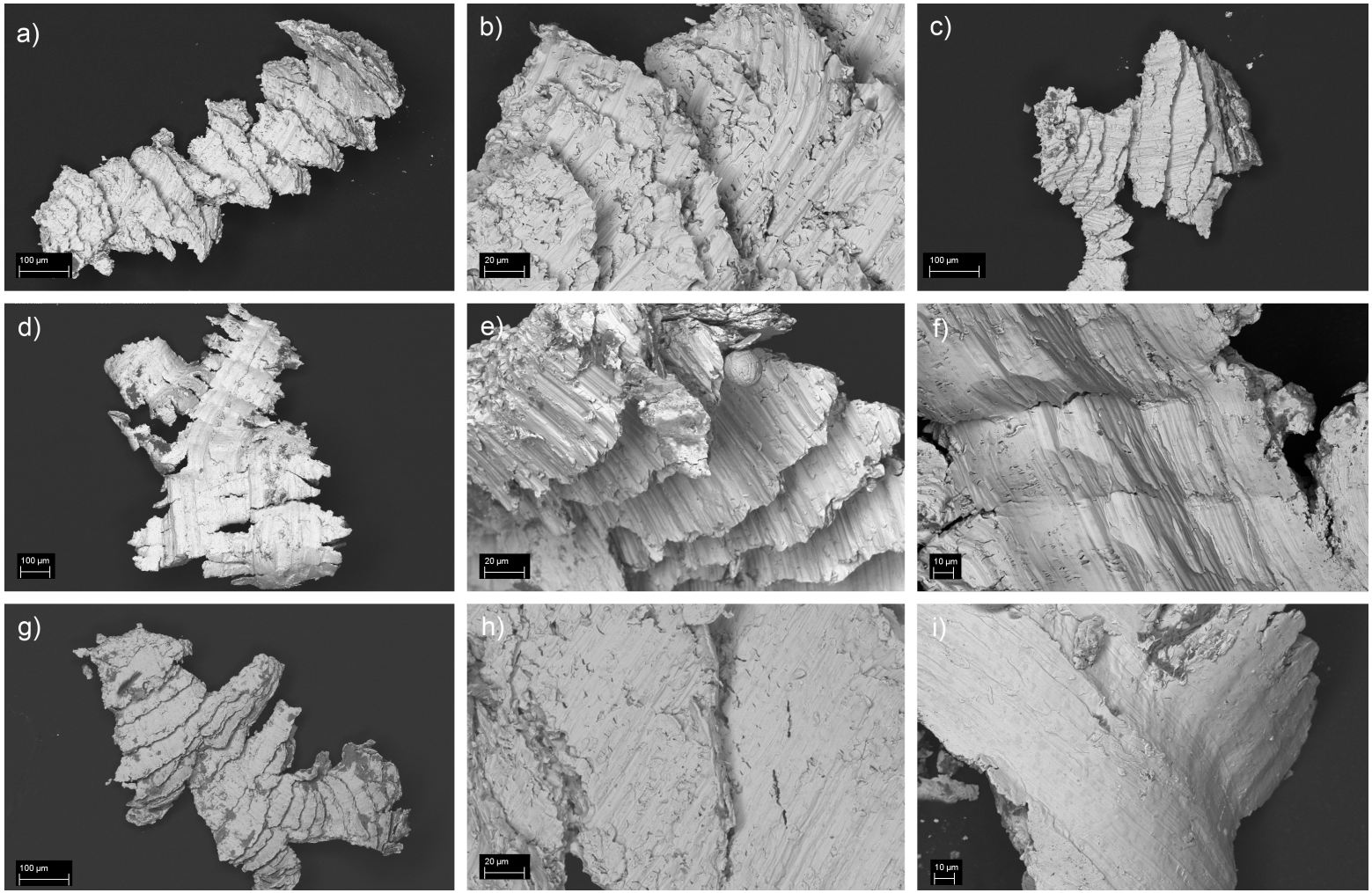

Figure 5.54: *Wear debris chips due to sliding abrasion from the tests with* $\beta = 90°$ *on WI5 (a - c), WI7 (d - f) and WI8 (g - i) specimens.*

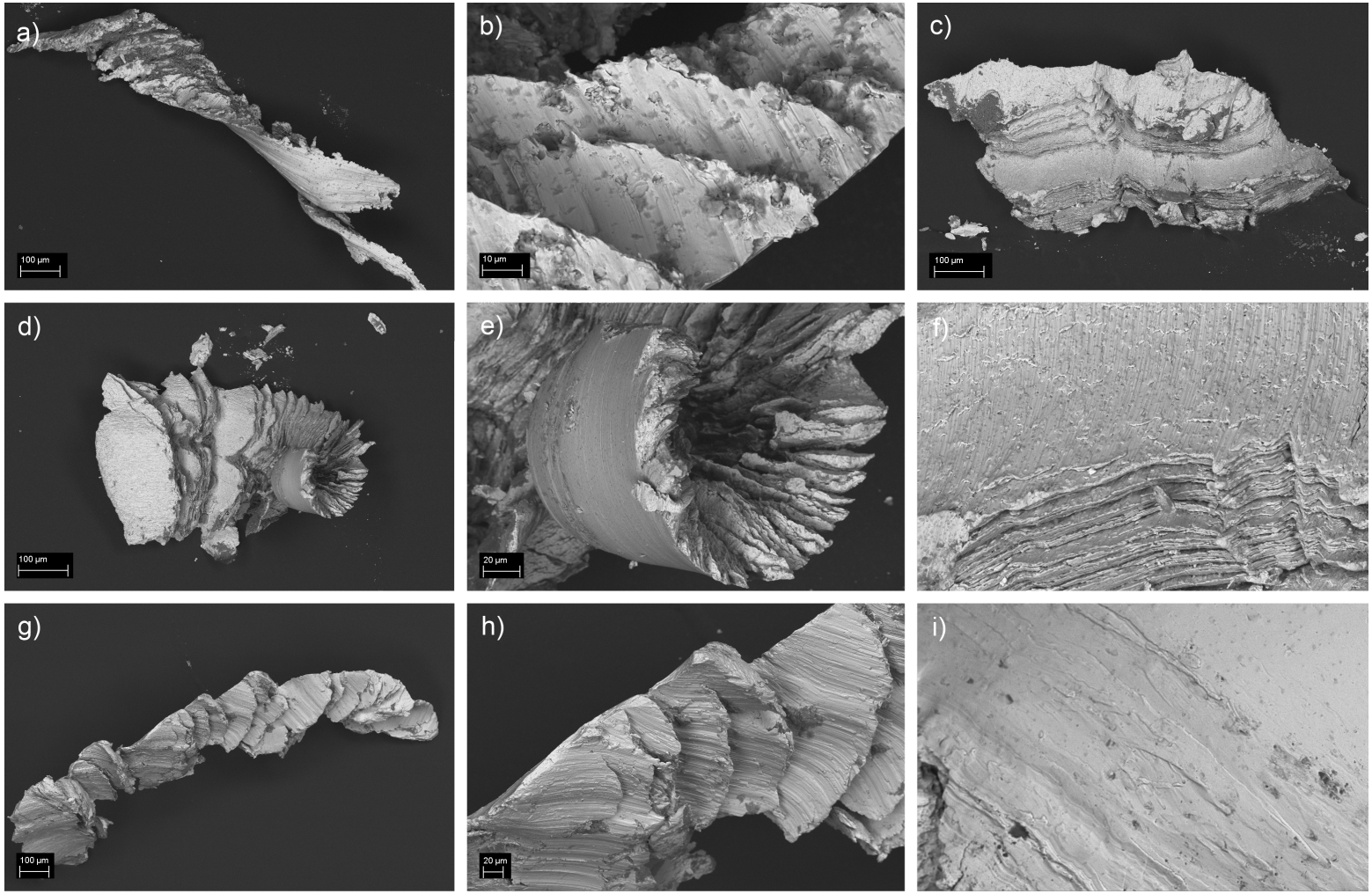

Figure 5.55: *SEM images of the wear debris chips due to sliding abrasion from the tests with $\beta = 90°$ on WR6SF (a and b), WR6H (c - f) and WR12 (g - i) specimens.*

whereas the average bulk hardness of the WR6SF steel matrix was 618±28 HV0.01 after 10 measurements.

The wear debris was also briefly examined from the S355 and manganese steel test series. The debris of S355 was found to be similar to the QT100 debris, and no definite serrated cutting chips were found from the debris. The amount of debris collected from the manganese steel tests was much lower than from the other tests. The larger size debris from the manganese steel XT710 apparently remained austenitic, which is not ferromagnetic and therefore could not be collected by a magnet. Also EDS- analysis from the smaller debris did not show chips with high manganese content. Some of the tests on the tool steels with the $\beta = 0°$ tilt were also inspected, and in most cases only few colored cutting chips were found. The increasing speed of the tests with the $\beta = 90°$ tilt resulted in an increasing amount of colored cutting chips. This indicates that the increased speed affects the sliding velocity of the particles on the wear surface, and consequently the probability of adiabatic shear banding of the chip. However, the collection method was manual and as such not accurate. The chip detection method was refined, however, by demagnetizing the debris to prevent agglomeration of the particles by magnetic attraction, which can also increase the amount of manually detected chips.

5.3 Reliability of data

The reliability of data can be examined from many perspectives. Avery [141] gives three stages of evaluation of a successful wear test: establishment of reliability, establishment of the ranking ability, and establishment of validity.

The reliability of the equipment means the ability to produce similar wear situations that are comparable between the wear tests. The random variations in the tests need to be overcome either by repeating the test, or increasing the repetitions within the test in order to minimize the effect of low probability events. These steps help only with the random variations. In addition, possible systematic variations need to be taken into account. In wear tests, the systematic variation could come for example from the variations in the movement or the geometry of the test settings. In this work, the systematic variations were minimized by using a controlled method to set the jaw geometry, the jaw movement, and the measurement system. The systematic variations could be reduced even further, as the equipment was in the prototype phase during the tests and was not adjusted between the test series.

From the statistical point of view, the amount of tests conducted in wear testing is quite low, which is caused by the vast amount of work needed to conduct a test. The standard deviation from three or five measurements does not have the same accuracy as several thousands of individual tests. However, a single DPJC wear test crushes thousands of individual rocks between the jaws, which causes the interactions to remove with a varying probability a varying amount of material from the wear surface. The high number of events in one test helps to reduce the variation of the average wear rate.

The reliability of the test can be examined by using the standard deviation 2σ value of the test, which gives the 95 % confidence interval, or a 5 % chance for the test result to fall outside the $\pm 2\sigma$ range of the normal distribution. Avery [141] suggested a simple method to calculate the confidence limits of a wear test with the number of test observations n_o being less than 10. The range of the tests is the deviation of the largest and the smallest measurement, which is multiplied by the 95 % confidence factor. For n_o=3 ,4 and 5, the 95 % confidence factors are 1.3, 0.72, and 0.51, respectively [141]. Another statistical measure

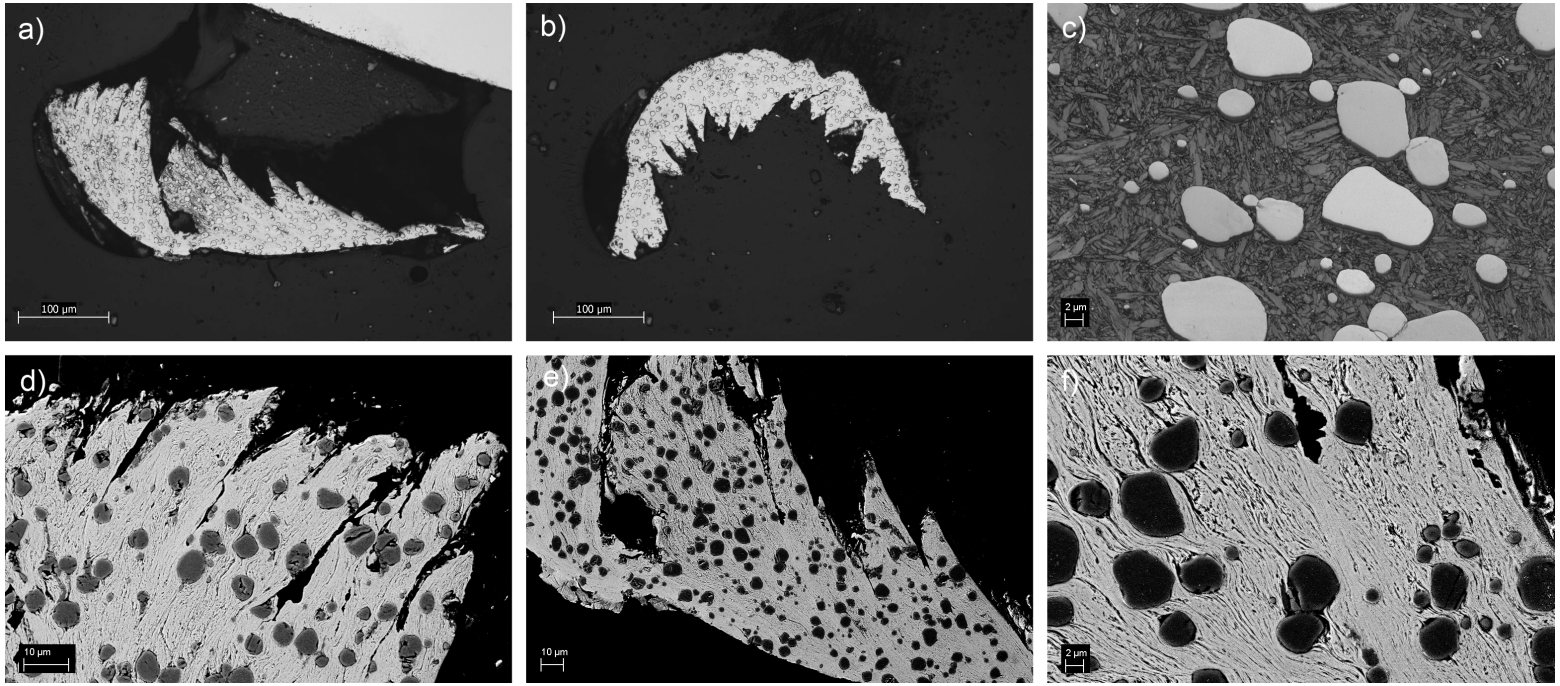

Figure 5.56: *Cross-sections of the wear debris chips from the WR6SF Jaw2 specimens tested with 5°+5° specimen angles and the β = 90° tilt. The overall images of the chips are shown in a) and b), whereas d) and e) and f) show the images with higher magnification. The microstructures of the chips show extensive elongation compared to bulk microstructure c), etch resistant (featureless) shear band in f) at the locations where serration has occurred.*

is to calculate the required number of samples n_s for the maximum allowable error e (%), as suggested by Tucker et al. [142]

$$n_s = \left(\frac{3V_0'}{e} \right)^2 \tag{5.1}$$

where V_0' (%) is the coefficient of variation that is the ratio of the standard deviation of the test and the average value of the test. Table 5.3 shows the average results and the standard deviations $\pm 2\sigma$ for the above mentioned statistical measures for the S355 reference tests and for the tool steel test series.

Table 5.3: *Reliability of the test data calculated from the sum wear of the specimens in the test*

Test	n_o	St. Dev. 2σ (%)	Avery 95 % conf. lim. (%)	n_s, e = ± 5 %
S355				
$\beta = 0°$	4	9.1	24.3	30.0
$\beta = 90°$	3(2)	3.32±2.62	4.24±3.42	5.20±6.26
Tool steels				
$\beta = 0°$	3(7)	9.31±4.93	23.1±12.5	38.7±30.4
$\beta = 90°$	5(8)	9.57±3.54	6.36±2.38	9.23±6.40

The data is calculated from the sum wear of the specimens in the test. n_o is the number of observations in the tests. The wear test results are considered as one series in the case of the reference tests with $\beta = 0°$. Due to the high amount of wear of the S355 material in the tests with the $\beta = 90°$ tilt, the two consecutive tests conducted on each of the three specimens are compared separately. The tests with $\beta = 0°$ show much higher 2σ variation than the tests with the $\beta = 90°$ tilt. The low 3.32 % variation of the test with $\beta = 90°$ shows that the equipment is capable of repeating the wear test quite reliably, when the amount of wear is high. In the tool steel series, each of the seven specimen pairs was tested three times with $\beta = 0°$. The S355 material is also included in the tests with the $\beta = 90°$ tilt, and each specimen pair is tested five times. The lower amount of wear causes higher variation in the test results, but the average 2σ is under 10 % in each test series. The confidence limits of Avery show much higher values of around 23 % in the tests with the $\beta = 0°$ tilt. Also the n_s value, i.e., the number of specimens needed for the ± 5 % error, is over 30, which in turn is much less with the $\beta = 90°$ tilt. In conclusion, the reliability of the tests is better with the $\beta = 90°$ tilt, which produces higher amount of wear.

The reliability of the DPJC tests with the $\beta = 0°$ tilt can be seen to increase with the amount of crushed rock in one tests. The reference tests with the $\beta = 90°$ tilt showed that the wear rate can change due to the increased gap between the specimen plates, if the removal of material is extensive. Therefore, the increased amount of rock in each test can cause changes in the wear rates of softer samples. The satisfactory method would be to equalize the amount of wear between the softer and harder materials by increasing the amount of rocks used in the wear tests of the harder materials until the set level of volume wear has occurred on the surfaces.

The establishment of the ranking ability is best shown in the tests with the tool steels in Figure 5.23. The volume wear rates with 2σ error bars show that the ranking of the materials can be established in the tests with the $\beta = 90°$ tilt, whereas it is more difficult to do

for the tests with the $\beta = 0°$ tilt. The ranking of the materials becomes more logical if also other relevant factors such as surface hardness are included in the comparison, as in Figure 6.3. The variations in the tests with the $\beta = 0°$ tilt need to be lower in order to be able to confidently rank similar materials with the test.

Establishment of the validity of the DPJC test results was studied by comparing the obtained results to the results of previous tests with other jaw crushers, as shown in Figures 6.1 and 6.3, where wear is compared to the hardness of the deformed surface. The test results show a slightly higher wear ratio for the DPJC test with a reference specimen, but in general the wear ratios in the DPJC tests are comparable with the other jaw crusher tests. The work hardening in the DPJC test has a linear relationship with the material's relative wear resistance, which is different especially from the tests on white cast iron by Borik [26]. However, the microstructure and the mechanical properties of the tool steels differ highly from the cast iron, which can affect the comparison.

6 Discussion

The results of this study show that the dual pivoted jaw crusher is a versatile new test method for wear testing and that its repeatability is also reasonably good. However, several factors have to be considered in a wear test before such a claim can be made. Wear results need to be reliably comparable within a test method, and ideally also comparable to the results obtained by using other similar test methods. The discussion part compares the results of the wear tests and focuses on the understanding of the relation between the wear and work done in the DPJC test.

6.1 Comparison of jaw crusher wear test methods

Several important parameters can affect the comparison of jaw crusher wear tests. The size of the jaw crusher defines the size of the applicable feed and what kind of compressive forces are obtained in the crushing process. Other parameters are the type of the feed, the geometry of the jaw crusher, and the actual method how the wear of the jaw plates are compared.

6.1.1 The size and mechanical properties of the feed in the jaw crusher wear test

In a crushing test, the possibility to use the amount of feed as a comparison method has several advantages, whereas for example the use of time or travel distance can have serious drawbacks. Figures 5.2 (p.55) and 5.4 (p.56) show that the wear and work outcomes are linearly related to the amount of rock crushed in a test, when no other parameters are changed. The time relationship of work accumulation in Figure 5.4 (p.56) shows linear increase but is also largely affected by the choking of the jaw crusher, which shows as horizontal parts in the data where no work has accumulated. The size of the feed is important for the test outcomes, but the amount of wear and work done in the tests are affected more by the reduction ratio of the rock during the tests than the selected feed size.

The disadvantage of using only the feed mass for test normalization in a jaw crusher test is that the size distribution of the feed can also affect the outcome of the wear process. Most of the feed with a wide size distribution is usually of the finer end of the distribution, which can affect the reduction ratio and the wear result of the test. Flakiness of the feed is another factor that can have a major influence on the wear outcome of the test. The flakiness of the rocks used in the tests discussed in this thesis were not measured, but visually the feed shape was the same. Also the tests were mainly conducted with Sorila granite from the same batch. However, the DPJC has also been used with highly flaky feed, which resulted in relatively low amount of wear and work, as the jaw crusher geometry is prone to align the flaky particles so that the compression of the particles occurs along their narrowest dimension. Nevertheless, the flakiness is a another factor that can influence the comparison of different rock batches.

The mechanical properties of the rocks affect the amount of wear and work produced in a test, but the relation of wear and work, as shown in Figure 5.13, is similar with similar types

of rocks such as granite, gneiss and tonalite. On the other hans, quartzite produces higher amounts of wear relative to the work done in the DPJC tests, which is due to the quartzite's higher quartz content causing high abrasivity but low fracture toughness. Also the amount of pre-existing cracks in the feed material can affect how easily the particles fracture, which shows as lower forces needed to crush the rock and results in both lower amount of wear and work done in the test. Such pre-existing cracks can originate for example from the previous crushing cycles [15].

6.1.2 Comparison of the wear ratio with different jaw crusher test methods

Figure 6.1 shows a comparison of the G81 and DPJC test data together with the results from the previous tests conducted by Borik with a jaw crusher [143]. The wear ratio of the materials is shown as a function of the carbon content of the material. The G81 tests show a small wear ratio in this comparison. This is partly affected by the manner how the wear ratio is calculated. Borik calculated the wear ratio as the mass loss of the test specimen in the stationary jaw divided by the mass loss of the reference specimen in the moving jaw, as only one specimen plate was used in each jaw. The ASTM G 81-97 test uses two plates in each jaw and the wear ratio is calculated as

$$W_R = \frac{\frac{X_s}{R_s} + \frac{X_m}{R_m}}{2} \tag{6.1}$$

where X_s, R_s, X_m, and R_m are the volume losses of the stationary test and reference specimens, and the moving test and reference specimens, respectively. Equation 6.1 is the same as Equation 4.1, but is presented here again to ease the comparison. This formula yields the average wear ratio of the specimens in each jaw, which evens out the increased wear in the stationary jaw due to the sliding movement. The sum wear ratio W_{RS} used to present the DPCJ results was calculated from the sum of the volume wear of both jaws as

$$W_{RS} = \frac{X_s + X_m}{R_s + R_m} \tag{6.2}$$

where X_s and R_s are the test and reference specimens in Jaw2 and X_m and R_m the test and reference specimens in Jaw1. In this formula, the wear ratio is not calculated using the reference data obtained from the same test with the specimen but using data from separate tests on the reference material. Therefore, the wear ratio of Equation 6.2 gives the wear ratio of the entire system. As the wear of the Jaw2 specimen is higher than the wear of the Jaw1 specimen in the DPJC tests with $\beta = 90°$, the wear ratio W_{RS} depends more on the Jaw2 specimen wear.

If the wear ratio is calculated using Equation 6.1, it will depend equally on the wear of the specimens in both jaws. This again means that the lower wear of the Jaw1 specimens becomes as significant as the higher wear of the Jaw2 specimens. When the DPJC wear ratio is calculated using Equation 6.1, the value of the wear ratio is lower than when calculated using Equation 6.2. Figure 6.1 shows both wear ratios for the DPJC tests with $\beta = 90°$. The difference is caused by the different wear rates between the jaws, where the relative performance of the material is worse in one jaw and better in the opposite jaw. Harder steels have a smaller Jaw1/Jaw2 ratio of the wear rates of around 0.13-0.16 compared to the 0.26 Jaw1/Jaw2 ratio of the QT100 reference steel. This means that harder steels experience more wear caused by sliding. The wear ratio of the harder tool steels and the QT100 reference material is lower between the Jaw1 specimens than between the Jaw2 specimens. This indicates that the tool steels have better wear resistance in Jaw1 than in Jaw2, when the test is conducted with the $\beta = 90°$ tilt. The wear ratios in the $\beta = 0°$ tilt

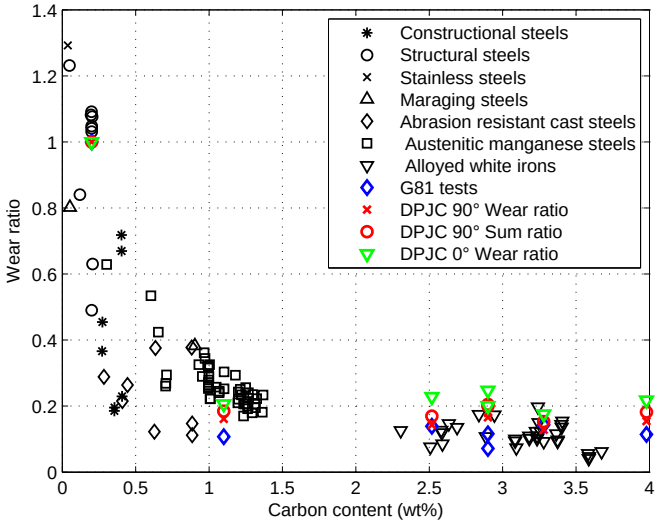

Figure 6.1: *Relation between the wear ratio and carbon content for several materials from the gouging abrasion tests with jaw crushers. The original data from Borik [143] is shown with black markers and the G81 and DPJC data with colored markers.*

are also shown in Figure 6.1, and they appear to be almost the same when calculated with both Equations 6.1 and 6.2. The wear of the specimens in both jaws is now also more or less the same. Without sliding movement of the jaws, the wear ratio of the tool steels shows higher values compared to the wear ratios with the $\beta = 90°$ tilt and the G81 tests. This means that in compression QT100 has a relatively better wear ratio than when there is a sliding movement between the jaws. The tool steels tested with the $\beta = 0°$ tilt show wear ratios of 0.17-0.25, which are almost twice as high as with the $\beta = 90°$ tilt. The difference is presumably caused by the high wear of the QT100 Jaw1 specimen.
It is not straightforward to determine, which of the wear ratios is better to use. Equation 6.1 leads to a better wear ratio for the tool steels in the DPJC tests, because the wear of the specimen in Jaw1 is as significant as the higher wear of the Jaw2 specimens. The wear ratio W_R could be better in the comparison where the wear of both jaws is equally important. However, if the wear ratio is used to examine the effect of the sliding movement, which causes uneven wear between the jaws, the emphasis should be more on the wear of the Jaw2 specimen. W_R is also sensitive to fluctuations in the wear of the reference steel, as in the case of the WI8 steel in the G81 tests. The wear ratio between the test and reference specimens in Jaw2 could also be used, but it loses some information about the whole test, as there is an increase of wear also in the specimens of Jaw1. Equation 6.2 could be better in the comparison of the tests where the sliding movement is investigated. It could also yield a better comparison between the wear ratios obtained with the $\beta = 0°$ and $\beta = 90°$ tilts.

6.1.2.1 Use of dissimilar specimens in the jaws

In the comparison of the wear ratios of the tests of Borik [143] in Figure 6.1, the ratios are again calculated with another method. The relative wear ratio comparison could benefit from the use of a reference specimen as the jaw opposite to the test specimen instead of

using a pair of test specimens. This method is also used in the ASTM G81 tests. One preliminary test was conducted with the $\beta = 90°$ tilt, where the Jaw1 specimen was S355 and the Jaw2 specimen was WR6SF. This test was not included in the test matrix, as the minimum gap used in the test was 6 mm and the maximum gap 8 mm. The used rock was the same Sorila granite of size 10-12.5 mm. The amount of wear was lower because the reduction ratio of the rock was lower. However, the wear ratio comparison can still be used. The wear ratio of a S355 specimen in Jaw1 and a WR6SF specimen in Jaw2 was 0.33 for the dissimilar pair, whereas in the tests with a similar specimen pair the wear ratio of the S355 specimen in Jaw1 to the WR6SF specimen in Jaw2 was 0.62. In comparison, the wear ratio of a WR6SF test specimen in the stationary jaw and a QT100 reference specimen in the moving jaw of the G81 test was 0.28, when the ratio was calculated with only one pair of the test plates. The ratio is close to the dissimilar pair test with the DPJC, and is significantly different from the wear ratio W_R of 0.07 in the ASTM G81 test. Therefore, the lower wear ratio values from the G81 tests in Figure 6.1 are expected when compared to the tests of Borik [143].

The differences in the wear ratios between dissimilar pairs can be explained by the influence of surface hardness on the contact mechanisms. A softer specimen of the dissimilar pair in Jaw1 increased the wear of the Jaw2 specimen relative to the specimen in Jaw1, when compared to the situation where both specimens are of a similar material. Most likely the change is due to the increased sliding of the rock particles on the harder tool steel surface and decreased sliding on the S355 surface. Similar results were found in the tests with the crushing pin-on-disk [139], where the change of the counterbody hardness had an effect on the pin wear. Also Axén et al. [47] concluded that the hardness of the counterbody is an important factor in three-body abrasion. Other factors can also influence the relative wear of the jaws, e.g., the use of corrugated specimens instead of flat specimen surfaces has been reported to cause higher wear in the moving jaw instead of the stationary jaw [28]. Sare and Hall [27] conducted tests by circulating three test materials, A, B, and C, using the method shown in Table 2.3. Their results are shown in Table 6.1. The corrugated jaw surface is presumed to be the cause for the higher wear of the moving jaw in the tests with specimen pairs B/A, C/A and C/B, which causes the relative wear to be lower than unity. Table 6.1 shows that the wear rate of material A is 0.42 times the wear rate of B, when inserted in the stationary jaw, and 0.86 when the jaw selection is the opposite. Similarly, the wear ratios of material C are 0.27 and 0.65 in relation to material B, depending on which material is in which jaw.

Table 6.1: *Jaw crusher wear ratios of three test specimens when tested against each other.*

Stationary/Moving	Jaw wear relation	1/x
A/B	0.42	
B/A	1.16	0.86
A/C	1.65	0.6
C/A	0.88	
B/C	3.67	0.27
C/B	0.65	

Another possible problem when using the ASTM G 81-97 test is the possibility that the left hand side jaw plates are more efficient in crushing than the right hand side plates, or vice versa. Ideally, both sides of the crusher have the same 50 % share of the total capacity. Uneven capacity causes a situation where for example the left hand side jaws could crush

60 % of the rock material, leaving 40 % of the material to be crushed by the other pair. The resulting factors for the stationary jaw relation X_s/R_s and for the moving jaw relation X_m/R_m would be 1.5 and 0.66 with the above mentioned percentage of unequal crushing. A calibration test of ASTM G 81-97 is used to detect such variations, but as it uses similar reference pairs, the effect of hardness difference of the surfaces is not taken into account.

6.1.3 Summary of the discussion on wear testing

The observed differences in the wear resistance of the WR series steels in the G81 and DPJC tests cannot be directly explained by the current results. Possible reasons for the different test outcomes could be the counterbody hardness affecting the sliding movement of the rocks on the test faces, or that the size or the amount of the feed are different. The extent of wear in the G81 tests is higher because of the larger size of the rock batch and because the gap needs to be adjusted during the test to compensate for the dimensional changes of the jaw plates, whereas the test geometry of the DPJC remains the same throughout the test.
The tool steels showed a lower relative wear resistance in the compressive crushing tests with the DPJC than in the tests containing also a sliding movement between the jaws. This could indicate that the reference steel was less wear resistant in the tests with the sliding movement. The wear ratio comparison could show better correlation if the reference specimen in the tests with harder steels had similar hardness values, which could negate the changes in the friction coefficients and the reference steel would also better retain its shape.

6.2 Relationship between wear, comminution and crushing work

The DPJC results allow to study the interdependence between wear of the specimens and the consumed energy. There are many investigations about the correlation between comminution and energy consumption of the jaw crushers [144, 145], or between comminution and work [30]. The whole system of a large jaw crusher has also been modeled with the discrete element method, which predicted 12.5 % and 9.6 % of the energy to be consumed on the wear of the fixed and moving jaws [146], giving a total energy consumption of 22 % on wear. However, the abrasive wear in the model concentrated on the upper section of the jaw plates, which was opposite to the tests with a smaller sized jaw crusher, where the abrasive wear attacked mainly the lower section of the jaws [30]. Similar results were also found with the DPJC and G81-97 tests of this work.

It is better to begin understanding a crushing situation from the possible outcomes of an individual crushing event. Firstly, a rock particle inserted between the jaws falls until it finds support from both jaws. The approach phase of the jaws closes the gap between the jaws and pushes the rock upwards until the friction between the rock and the jaw faces overcomes the resultant upwards pushing force. This movement can cause abrasion on the jaw surfaces, and can also result in fracturing of the abrading particle's protuberances. Further closing of the gap causes elastic deformation of both the jaw plates and the particle, and plastic deformation when the yield strength of the materials are reached. Both jaw surfaces experience the same load in the compressive situation, whereas the amount of contacts, the contact area, and the direction of load may vary. Most likely the contact area on both jaws is adequate to produce plastic deformation. The size of the indentation continues to grow with increasing load, until 1) the approach part of the cycle is finished, 2) the upward force overcomes the frictional force due to plastic deformation and the rock slips between the jaws, or 3) the load is high enough to fracture the rock particle.

In Case1, the load and the work stored in the elasticity is released, and work is done only on the plastic deformation of the indentations and on the growth and initiation of cracks in the rock. An example of this kind of compression is presented as the first compression cycle in Figure 4.7 (p. 50). The amount of wear caused by the event can be estimated from the amount of wear of a similar material in a surface fatigue wear test. Saarna et al. [147] conducted indentation wear tests where a 6 mm x 6 mm area was deformed by 30 000 indentations with a force of 1.5 kN. The amount of wear of a Hadfield steel under those circumstances was 2.3 mm^3. The lowest amount of wear of XT710 steel was around 2.5 mm^3 for a single specimen in a S1-C1 DPJC test, which is done with a 4 kg rock batch and needs around 2000 to 4000 compression cycles to crush the batch. If the cycles of the tests are normalized, the amount of wear caused by the surface fatigue wear test was 10 % from the amount of wear caused by the DPJC test. This comparison can be used to estimate how much wear the Case1 situation can produce. The amount of accumulated work from mostly elastic compression should also be very low. Figure 5.7 (p. 57) can be used to estimate that after the 1300 J/kg of work needed for crushing is substracted from the measured 1500 J/kg, the remaining 200 J/kg of work is spent on the indentation and wear of both specimens. Using the 10 % relation between the fatigue wear test and the DPJC test, we can estimate that around 10 J/kg per specimen of the total work of 1500 J/kg is spent on making indentations, which is around 0.7 % of the total work.

In Case2, the particle remains intact and only slides along the jaw plates, as the elastic energy stored in the jaws and in the particle are used to push the particle upwards. No work, or in the case of fracture of the protuberances only a minor amount of work, is done in comminution, and the work can be seen to be spent on the deformation of the jaw plate surfaces due to abrasion, on the remaining kinetic energy of the particle, and partly on the elastic vibrations of the equipment when the particle is detached from the jaw surfaces. Slipping of the particle is most likely to cause more wear than the pure indentations in Case1.

In Case3, the load cycle is interrupted by the fracture of the rock. An example of this kind of an event is shown as the third and fifth cycles of compression in Figure 4.7 (p. 50). The fracturing of the rock occurs in tension on a plane parallel to the load direction [7]. In the case of an ideally round particle the fracture occurs in the middle of the particle, causing the two partials to separate rapidly. The elastic rebound of the jaw frame adds kinetic energy to the partials, and their movement can cause abrasion against the jaw plates. In essence, the elastic energy stored in compression is released partially in the case of a smaller fracture or totally in the case that the rock does not anymore have contact with the jaws after the fracture. The released energy from the compression is most likely transferred to kinetic energy of the fractured rock and to vibrations of the jaws, and only a small portion of energy is used to create new fracture surface in the particles. In some cases the rock fractures during the unloading phase, which can be seen as a sudden drop in the compressive force measured in the DPJC test, also accumulating work. A high speed camera was used to measure the velocity of the fractured particles after the crushing, reaching values up to 1 - 2 m/s. The upper limit of the kinetic energy of a rock weighing 2 g can be estimated to be around 0.001 J - 0.002 J in the case when all fracture partials have the same velocity after the fracture. In the case of slipping, the particles have enough kinetic energy to reach around 0.5 m higher elevation from the jaws, which yields 0.01 J of potential energy against the pull of gravity. If a 4 kg batch with 2000 particles experiences similar 1 - 2 m/s particle velocities after the crushing situation, the upper limit for the total amount of kinetic energy of the particles in a test is from 2 J to 40 J, which is a negligible (less than 1 %)

amount of the total work measured in a DPJC test. The elastic energy stored in compression is then most likely mainly transferred to vibrations of the crusher and the particles, which eventually results in a small increase of the temperature of the particles and the jaw crusher.

In a fully compressive situation the load produces indentations and pushes material to form sidewalls. The size of indentations and sidewalls depends on the hardness of the surface. The introduction of lateral movement between the jaws causes a change in the direction of the compressive force by deviating it more from the normal of the jaw plate surfaces. This increases the possibility and the amount of sliding of the particles, which increases mainly the proportion of Case2 interactions. As the test is controlled by the Case3 interactions, which involve the actual comminution of the feed, it is reasonable to assume that the amount of Case3 interactions remains roughly the same between the tests. A single work cycle of the crusher can involve both Case2 interactions, where the rock slides upwards along the Jaw2 specimen before it is crushed in the Case3 interaction. Case1 interactions are shown to have a minor influence on wear, work and comminution, which means that the changes mainly in the amount of work and wear are influenced by the Case2 interactions. Parameters such as jaw angles and the amount of sliding due to the axle tilt setting β are directly related to the possibility of Case3 interactions to occur. The reduction ratio and the size of the feed are more related to the amount of Case2 interactions needed for comminution, which are also related to the overall amount of Case3 interactions.

From the above example it is reasonable to assume that the wear in a jaw crusher depends on the comminution of the rock, but the comminution of the rock does not depend on the wear of the jaw plates. Slipping of rock particles on the jaw faces is easier with higher hardness of higher wear resistance jaw plates and consequently due to the reduced friction coefficient. Increased slipping can cause slower throughput and reduced capacity of the crusher, but the size distribution results show that the the size reduction of the feed is mainly controlled by the gap settings of the jaw crusher.

6.2.1 Relationship between wear and work

Equation 2.44 (p. 29) shows that the relationship of wear and work depends on the friction coefficient μ, deformed surface hardness H_{def}, and a dimensionless wear coefficient K. The amount of comminution is not part of the equation, which is reasonable if the crushing work is independent of the sliding work involved in the wear of the specimens. According to Equation 2.44 (p. 29), the increase of the friction coefficient and the deformed surface hardness in the test means decreased amount of wear relative to the work done. The frictional force and wear have in some cases been found to be proportional to each other [106, 122]. The frictional force in abrasion is dependent also on the attack angle of the particle, as shown in Equation 2.37 (p. 27). Fore example Figure 5.20 (p. 65) show that the increase of sliding with the XT710 manganese steel specimens with specimen angles of $5°+5°$ increases the friction coefficient from 0.25 to 0.45. The hardness profiles of the specimens in Figure 5.38 shows that the Jaw2 specimen from the $\beta = 90°$ test has a lower surface hardness than the specimen from the test with the $\beta = 0°$ tilt. The decreasing hardness and increasing friction coefficient compensate for each other (in Equation 2.44 (p. 29)) leading to the linear relationship between wear and work when the sliding component is increased.

For better understanding of the relationship between wear and work, it is advisable to examine separately the effects of the individual components of Equation 2.44 (p. 29), i.e., the hardness, friction coefficient and wear coefficient K, on this relationship.

6.2.1.1 Material's wear (resistance) and deformation hardness

Several authors [43, 106] have shown that the hardness of the deformed surface greatly affects the wear resistance of a material and that the use of the bulk hardness for the estimation of the wear resistance can be misguiding. The level of hardness reached by the deformed wear surface depends on the material's mechanical properties, wear environment, wear mechanisms, and the contact forces with the counterbody. The best way to determine the level of work hardening is to measure the hardness directly from the worn surface. Other means have also been suggested, for example by Zum-Gahr [2] to measure the hardness of the wear debris, or by measuring the hardness of a surface deformed to a high degree, e.g., by trepanning [75]. In this work, the surface hardness was measured from the Jaw2 specimen wear surface using the taper section technique. Figure 6.2 shows the relative wear resistance of the studied materials as a function of the wear surface hardness in the DPJC tests with the $\beta = 90°$ tilt. As seen, the dependence is quite linear for all materials. For the XT710 manganese steel with a relatively lower bulk hardness, the surface deformation increases the hardness considerably to a level fitting the linear dependence of the other test materials. The use of the wear surface hardness instead of the bulk hardness can also better explain the different wear results obtained for the tool steels. The best wear resistance is generally found for materials that show the highest wear surface hardness.

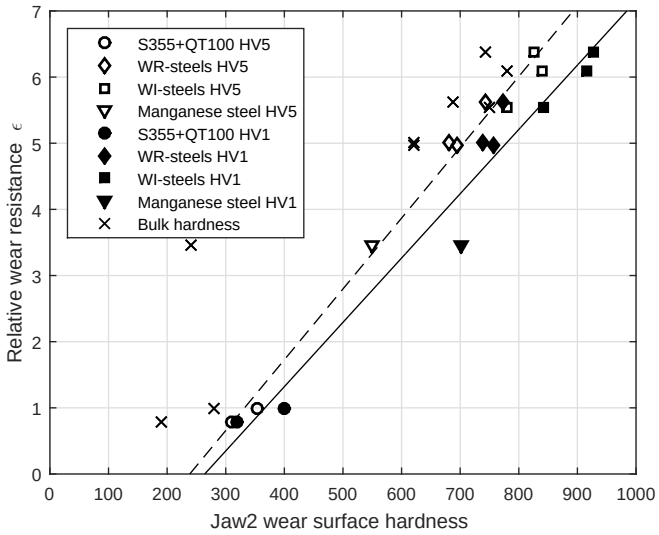

Figure 6.2: *Relative wear resistance of the test materials as a function of the measured wear surface hardness after DPJC tests with the $\beta = 90°$ tilt. The bulk hardness of the materials are shown as black x-markers.*

The surface hardness comparison based on the HV1 loads is shown in Figure 6.2 in addition to the surface hardness determined with the HV5 load. The use of HV1 and HV5 loads in the comparison of the WR and WI steels produces values that fit quite well on a straight line, although the slopes of the HV5 and HV1 are slightly different, as seen in Figure 6.2. A closer look, however, reveals that the WR steels are positioned more on the left hand side of the plotted linear fits, indicating a slightly higher relative wear resistance ϵ than the WI steels that are positioned more to the right hand side of the linear fits. The hardness

measurements with 5 kg load (HV5) show better linear fit than the measurements with 1 kg load (HV1).

The highest compressive forces in the DPJC tests were several kilonewtons, and the abrasion grooves on the test specimen wear surfaces were several hundreds of micrometers wide. Therefore, the total contact area of the rock particles with the wear surface can be estimated to be much larger than the indentations produced by a hardness test with a 5 kg load. However, the total contact area is divided into several protrusions that interact with the wear surface. The hardness tests conducted with the higher 5 kg load could be more reliable for estimating the flow strength of the deformed material, whereas the HV1 and microhardness tests could better relate to the smaller abrasive size of the indenting rock particles.

Figure 6.3 shows the relation between the relative wear resistance and the deformation hardness in the tests of Borik and Scholtz [26] and their comparison with the DPJC test results with the $\beta = 0°$ and 90° tilts. The hardness values of Borik and Scholtz [26] were converted from Brinell to Vickers to ease the comparison. Only the constructional steels are close to the linear fit of the DPJC tests with the $\beta = 90°$ tilt. Both the manganese steels and white cast irons show higher wear resistance than the materials tested with the DPJC. However, there are differences in the test methods. Borik and Scholtz used 30 mm - 50 mm rock and dissimilar specimens in the jaw crusher. Also the low alloy steel reference material is not exactly the same as QT100, although they work harden similarly from 270 HV bulk hardness to 356 HV measured from the Jaw2 specimen after the test with the $\beta = 90°$ tilt. The manganese steel tested with the DPJC fits fairly well into the group of manganese steels tested by Borik and Scholtz [26]. However, the white cast irons have a significantly higher relative wear resistance than for example the WI steels. The microstructure of the cast iron could contain larger carbides that are beneficial, but this cannot be confirmed as the information was not available.

Also the moraine rock used in the tests of Borik and Scholtz [26] could yield different results, especially when the hardness of the test material is closer to the hardness of the abrasive minerals. The results of the G81 tests are also shown in Figure 6.3. These tests show much higher relative wear resistance for both WR and WI steels. The relative wear resistance of the WI steels in the G81 tests is closer to the white cast iron results of Borik and Scholtz [26], whereas the WR steels show much higher wear resistance than expected from the hardness of the wear surface. The same trend was visible in the surface roughness S_a values shown in Figure 5.48 (p. 89), where the surface roughness S_a of the WR steels in the G81 tests was higher than that of the WI steels.

The results show that the relative wear resistance in the DPJC tests increases linearly with the increase of the measured surface hardness of the specimens after the tests. The tests with $\beta = 0°$ show lower relative wear resistance for the tool steels, whereas the austenitic manganese steel shows a clear improvement when compared to the tests with the $\beta = 90°$ tilt. Either the tools steels perform relatively better, when there is a significant lateral movement between the jaws, or the QT100 reference steel performs worse in the sliding abrasion situation. The effect of hardness on the measured work is difficult to estimate, as the friction coefficient and hardness are interrelated. Therefore it is better to compare both the hardness and the friction coefficient to the work done in the tests.

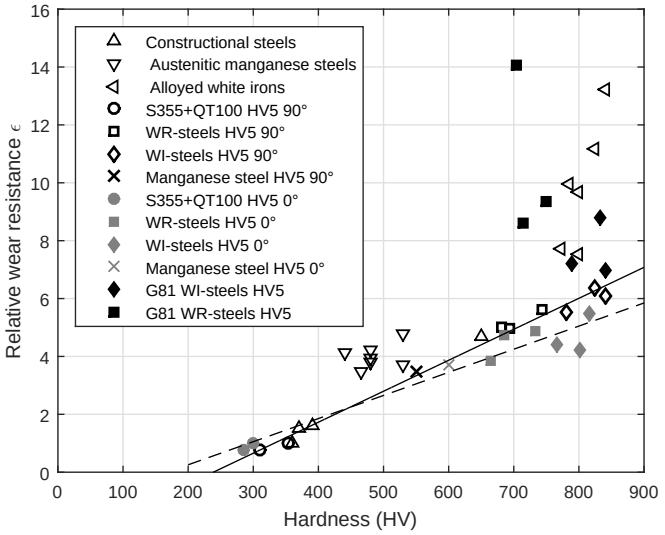

Figure 6.3: *Relative wear resistance of the materials in the DPJC tests with $\beta = 0°$ and $90°$ compared to the results of Borik and Schultz [26] (triangular markers) and the tests performed according to the G81-97 standard.*

6.2.1.2 The effect of friction coefficient on wear and work

Figure 5.20 (p. p.65) showed how the friction coefficient μ varies with the movement and geometry of the jaw crusher, increasing when the jaw angle of the Jaw2 specimen increases. Also the increase in the sliding movement increased μ and decreased the effect of the Jaw2 angle on μ. The size of the rock had a smaller influence on the measured μ values. Figures 6.4 and 6.5 show histograms of the accumulated work as a function of the friction coefficient for $\beta = 0°$ and $90°$, respectively. The friction coefficient is calculated from the force components F_{Z2} and F_{Y2} aligned normal and parallel to the surface of the Jaw2 specimen. The Figures do not show the actual amount of contacts but rather the amount of work accumulated from the contacts. Therefore there are less contacts with higher friction coefficients and a higher number of contacts with low friction coefficients, even though the amount of work of the histogram categories are the same. The histogram is calculated from the total work of 4 kJ - 5 kJ done in the tests with a 4 kg batch of rock. The peaks in the friction coefficient histograms in the tests with $\beta = 90°$ in Figure 6.5 show values of 0.45 for the WR steels and slightly lower values from 0.4 to 0.45 for the WI steels, whereas QT100 had a higher μ peaking at a value of 0.5. The small differences between the tool steels mean that the friction coefficient and work behave similarly between the tests, when the sliding component is large. Equation 2.37 (p. 27) indicates that increasing H_{def} of the surface decreases the friction coefficient in a grooving situation [2], which occurs in the DPJC crusher test with the $\beta = 90°$ tilt. In the compressive situation of Figure 6.4, the friction coefficient histogram shows interesting differences between the steels. The peak of QT100 has the lowest μ value between 0.2 and 0.25, whereas in the sliding movement situation in Figure 6.5 QT100 has the highest μ values. Also WI7 and WI8 steels show low μ values of 0.25 and 0.3. The WR6 steels show similar values of 0.4, and WR12 peaks at 0.45. The highest peak value of μ is with WI5 steel at 0.5. WI5 also shows a different shape of the histogram compared to the

other steels, which could be originating from the faulty bearing affecting the measurement. This makes the μ comparison of the WI5 steel with other steels unreliable.

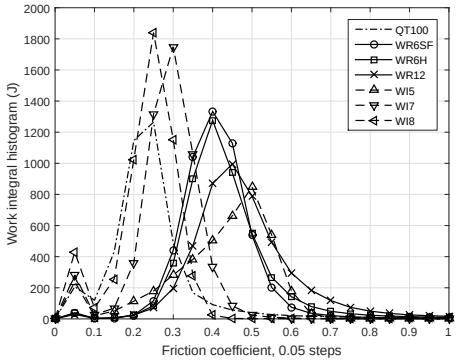

Figure 6.4: *Histogram of work as a function of the friction coefficient of the tool steels in the tests with $\beta = 0°$ tilt.*

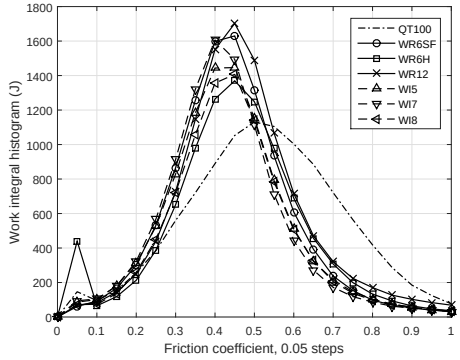

Figure 6.5: *Histogram of work as a function of the friction coefficient of the tool steels in the tests with $\beta = 90°$ tilt.*

High friction coefficient μ of the contact can originate from a static situation, which usually shows higher friction than the sliding (dynamic) situation, or from highly abrading contacts, which penetrate deeper into the material and can also produce higher friction coefficients. Highly abrading contacts most likely require also high contact forces. Figure 6.6 shows a contour map of QT100 and WR series steels in the tests with $\beta = 0°$ tilt, where the colored areas show the fraction of the total work accumulated at certain contact force and friction coefficient values. The Figure shows, for example, that the high friction coefficient peak of WR12 at 0.5 occurs mainly at lower contact forces below 1.5 kN, and contacts with higher contact forces generally have lower friction coefficients. This could indicate that the high friction coefficients stem from static compression contacts. High μ could also indicate how easily the particle can move or slip on the surface under compression, as the lower friction coefficients could originate from the sliding and rolling of particles even at higher loads [119].

Both QT100 and WI8 show the peak value of accumulated work done at the same values of the friction coefficient in the tests with $\beta = 0°$ tilt. On the other hand, they also show the worst and the best wear results, respectively. Therefore it is really difficult to estimate what is the relationship between the friction coefficient and wear. The linear estimation of minimum crushing energy E_0 divides the work so that wear related work from the total work done in compressive crushing is around 17 %, which is close to the 22 % value obtained numerically for larger jaw crushers [146]. One explanation for the variations in the friction coefficient could be the difference between the wear of Jaw1 and Jaw2, as the WR12 specimens were the only ones wearing evenly, whereas other steels showed higher wear of the Jaw1 specimens. If the rock particles prefer to slip on the Jaw1 surface, it could show as a decreased friction coefficient in Figure 6.4. The measured surface roughness of the WR steels was slightly higher than that of the WI steels in the tests with $\beta = 0°$, which could also indicate generally a higher friction coefficient. The increasing H_{def}/H ratio has also been linked to an increase in the friction coefficient [120], which in the case of compression crushing does not seem to hold, as for the XT710 steel μ 0.25 in the compressive test with the highest H_{def}/H ratio. It is therefore difficult to come to a conclusion on how the material

properties, wear, and the friction coefficient are related in the compressive crushing, without more extensive studies.

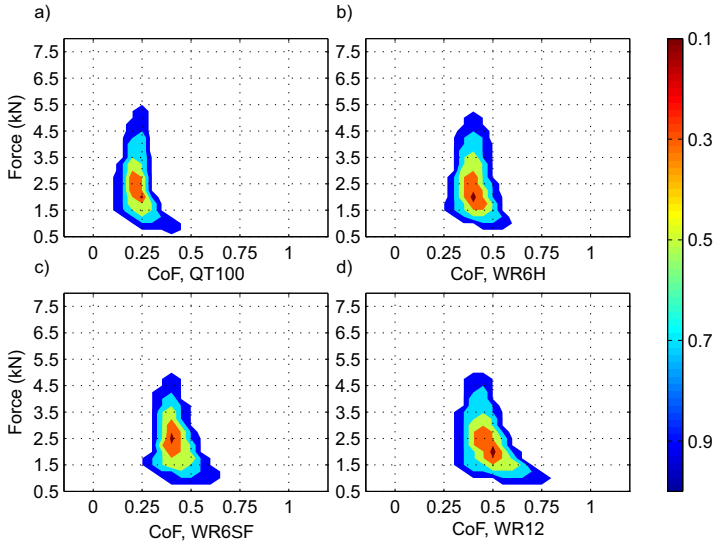

Figure 6.6: *Contour maps of accumulated work as a function of contact force and friction coefficient for the QT100 and WR steel series in the tests with $\beta = 0°$ tilt. The color of the region depicts the fractions 0.1, 0.3, 0.5, 0.7 and 0.9 of how much of the total work has been conducted inside the colored region.*

6.2.1.3 Correlation between measured tangential forces and wear

Atkins [140] divides the interactions during cutting of the material according to the depth of cut. A shallow cut leads to rigid-plastic continuous chips that show a smooth force curve as the cutting tool travels along the workpiece. The mode changes to elasto-plastic behavior with discontinuous chips when the depth of cut increases. The discontinuity of cutting shows as peaks in the force data, which occur at a certain frequency if the cutting process is stable.

A Fast Fourier Transform (FFT) spectral analysis was conducted with Matlab® on the DPJC force sensor signals in order to detect the wave frequencies existing in the signal. Two distinct peaks were found from all tests at around 400 Hz and 1650 Hz. To determine the origin of these waves, the elastic wave signals of the jaw frame configuration were measured by hitting the jaw frame with a hammer. The tests were conducted using a 2 MHz sample frequency of the oscilloscope with and without compression subjected to the stone between the jaws. The resonance frequencies of the jaw frame were mostly 1.6 kHz and 4 kHz. However, blows with a hammer in the direction of the compressive load resulted in low amplitude vibrations at around 400 Hz. Therefore, the frequency peaks in the FFT-spectrum were identified to be mainly caused by the vibration of the jaw frame during the elastic springback after the rock is crushed.

The successive elastic wave amplitudes in the hammer blow tests decreased greatly after the initial peak, and no condition was found where the succeeding amplitude would be greater

than the initial. Figure 6.7 shows a test with a 400 Hz vibration at the beginning of the compressive cycle, which started before significant compressive forces were achieved. The test was conducted with the WR6SF steel using $\beta = 90°$ tilt with 5°+5° jaw angles and the speed of 315 rpm. The blow tests do not explain the rising amplitude of the lateral force when the compressive load is smaller than the lateral force, yielding a friction coefficient of oscillation above 1. The oscillation occurs when the lateral speed of the jaws is at maximum and after the compressive displacement Z_2 has been initiated. As the vibration occurs at the beginning of the contact, it could contain information about the sliding contact between the rock and the steel surface. The maximum lateral velocity at the point of vibration is 425 mm/s, which yields a travel of around 100 μm between each oscillation at the frequency of 400 Hz. When the cutting chips are compared, the longest serrations in the chips are about 100 μm, which indicates that the vibrations could come also from the chip formation. Atkins [140] mentions that continuous chip formation in turning can show serrations, which can be attributed to oscillations in the depth of cut caused by the deflection of the cutting tool under the cutting forces. In DPJC, the jaws are not entirely rigid but can elastically bend under compression, which can cause oscillations. Also the low elastic modulus of silicon based minerals can cause oscillations, as the stone can act as a spring between the jaws. There is also a possibility that the jaw frame assembly resonates at around 400 Hz when subjected to compression, which can amplify the formation of cutting chips under correct circumstances. To summarize, the detection of wear related signals from the dynamic tests is difficult as the vibrations of the equipment are also recorded with the force sensors, bringing uncertainty to the identification of the sources of the vibrations.

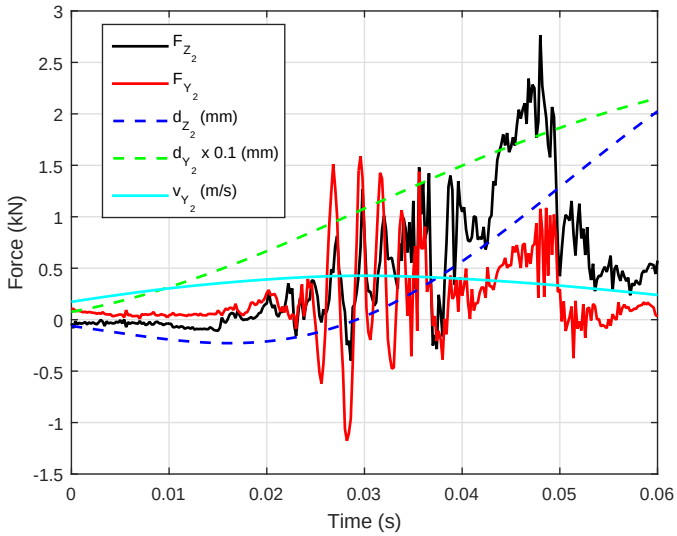

Figure 6.7: *Calculated compressive and lateral forces in the Z_2 and Y_2 coordinates in a compressive cycle of a WR6SF steel test with $\beta = 90°$ tilt at the speed of 315 rpm. The displacements d_{Y_2}, d_{Z_2} and the velocity v_{Y_2} between the jaws in the Y_2 direction are also presented.*

6.2.1.4 Effect of wear coefficient K on wear and work

The wear coefficient K contains the other possible factors related to the relationship between wear and work in Equation 2.44 (p. 29). The linearity of the slope in Figure 5.7 (p. 57) indicates that the right hand side of the equation remains at a constant value when the sliding component is changed. The increase of the friction coefficient doubles from 0.25 to 0.5 with the increase of sliding movement, whereas H_{def} of the Jaw2 specimen increased from 285 HV1 to 310 HV1, which is only a 8.7 % increase. Figure 5.31b (p. 73) shows the K slope for the tested materials with different sliding to compression ratios, where the S355 steel markers scatter more from the linear fit compared to the linear fit in Figure 5.31a (p. 73), but still show quite a good correlation.

The volume wear rate comparison of QT100 and the tool steels in Figure 5.31a (p. 73) shows higher values for the QT100 with accumulated work around 1000J - 1300J, whereas the $W_V H V_{def} \mu$ comparison in Figure 5.31b (p. 73) shows similar values for all steels. This includes also the S355 steel, which shows higher work values due to the larger feed size used in the tests. Therefore it can be reasoned that the wear coefficient K in compression is similar for all tested steels, and the relation of Equation 2.44 (p. 29) holds true for compressive crushing wear in general. However, the average 2σ deviation of the results in the tests with $\beta = 0°$ was around 9 %, which causes some inaccuracy in the determined K values.

The introduction of sliding movement causes a change in the abrasive situation, and the K value of softer steels is much higher than with the tool steels and the XT710 manganese steel. The main difference between the tests with the $\beta = 0°$ and $\beta = 90°$ tilts is the length of the grooves and the possible strain rate of plastic deformation.
Sundarajan [90] describes K in Equation 2.29 (p. 23) in a chip forming wear condition. The equation was developed for a situation where a pin slides against an abrasive paper in a steady state wear condition. The flow stress parameter contains several possible variables, which could be used to explain the different K values between the steels. The examination of wear debris showed evidence that the tool steels have a higher chip formation temperature T_c than the other tested steels. The effect of this can be estimated by substituting C_{min} by the thermal coefficient C, which causes the factor $(1 - (\frac{4.5}{T_m{}^{1.3}}(T_c - 300))$ to have smaller values with an increase in the chip formation temperature (1 for $T_c = 300$ K, and 0.75 when $T_c = 1400$ K), which increases the value of K. This should show as a decrease in the wear resistance of the tool steels.
The tool steels also have lower strain hardening exponents and presumably require smaller strains for chip formation. Equation 2.32 (p. 24) can be used to estimate the effect of ${e_c}^{n+1}$ in Equation 2.29 (p. 23). Typical n values for low carbon steels are around 0.25, 0.15 for alloyed steels, and around 0.5 for highly strain hardening steels [115]. The value of n for tool steels can be estimated to be below 0.1, which with the H_{def}/H ratio of around 1.1 leads to e_c values of 0.2. Similarly, the H_{def}/H ratios of XT710 and QT100 are around 2.5 and 1.5, and an estimation of n as 0.5 and 0.2 leads to e_c values of 0.5 and 0.6. Sundarajan [90] mentioned that the n values at high strains and high strain rates are significantly lower. Halving the n values yields e_c of 0.54, 3.1 and 4.6 for the tool steel, QT100 steel, and XT710 steels, respectively. This difference between the steels continues to increase with decreasing n. The example shows that the critical strain component should be lower with tool steels, which decreases the K value. The flow stress coefficient S_0 of the tool steels can be expected to be significantly higher than that of the softer steels, and should also be expected to decrease the K value. The other parameters in Equation 2.29 (p. 23) are expected to be similar for all steels.

6.2.1.5 Comparison of wear specific energies in DPJC, grinding, and milling

Figures 5.18 (p. 64), 5.19 (p. 64), and 5.31 (p. 73) can be used to obtain the wear specific energies of the tests. This energy varies from 28 J/mm^3 for the S355 steel up to 250 J/mm^3 for the WI-8 steel. The energy required to melt material is considered as the lowest possible energy to remove a unit volume of material, which for steels is around 10.3 J/mm^3 [130]. In grinding and cutting the depth of the cut is reported to affect the wear specific energy, where increasing cutting depths decrease the required specific energy until at sufficiently large cutting depths the wear specific energy saturates near the energy levels required for melting [130]. In grinding of a steel with a hardness around 330 HV (34 Rockwell C), the 30 J/mm^3 level was reached at the 10 μm depth of cut before saturating close to the melting energy at the cutting depth of 40 μm [130]. Similar specific energies have been reported in turning, where the specific energy of material removal (mm^3/s) varies from 200 J/mm^3 to 15 J/mm^3 with the material removal rate [148].

The collected cutting chips in the DPJC tests show that the larger chips can have a thickness from tens of micrometers for the tool steels to over hundred micrometers for the S355 and QT100 steels. Therefore it is reasonable to assume that the cutting events with the S355 steel can produce penetrations deep enough to reach the wear specific energies close to the 10.3 J/mm^3 limit, and that the higher wear specific energy of 28 J/mm^3 is caused by the natural variation of the contacts, as not all contacts cause cutting wear. The effect of the material removal rate could be related to the higher wear coefficient of the tilted Jaw2 specimens in the DPJC tests on the manganese steel shown in Figure 5.21 (p. 66), where the initial lateral speed between the jaws at the start of the compressive cycle had presumably been higher than in the tests with the 10° + 0° jaw angles.

6.2.2 Effect of jaw geometry and rock properties on the relationship between wear, comminution, and work

The tests with the manganese steel showed several interesting results. Firstly, doubling the approximate reduction ratio from RR = (2:1) to (4:1) also roughly doubled the estimated minimum energy of crushing. This supports the assumption that the minimum crushing energy E_0 could be obtained by extrapolation from the zero wear level. Figure 5.22 also showed that the normalization of the wear and work results with the measured reduction ratio RR could improve the accuracy of the estimation of the E_0 value. Another rock property related result was that the relationship of wear and work was quite similar between several igneous rock types containing volume fractions of plagioclase between 36 % - 45 % and quartz between 25 % - 40 %. Similar results indicate that this relationship can be used for normalizing the wear test results rather than for example the amount of feed used in the test. This approach would also reduce the effect of the variations in the crushability of the rock, which can originate for example from the changed crack density.

The jaw geometry of the DPJC was shown to affect the relationship between wear and work, and in some cases also the amount of comminution of the feed. The tests with the $\beta = 90°$ tilt and tilted Jaw2 specimens showed high wear relative to the work. Figure 6.7 shows that the lateral speed between the jaws reaches a maximum when the compressive contact initiates in the test with the 5°+5° specimen angles and $\beta = 90°$ tilt. The speed tests in Figure 5.28 (p. 70) show increasing wear with increasing speed of the crusher, and correspondingly lower wear for WI5 steel with decreased speed of the crusher. Supposedly in the tests with sliding movement and tilted Jaw2 specimens the strain rates are high enough to

change the wear mechanism. The reduction ratio of the rock was unfortunately not measured after the speed tests, which would have been an important piece of information for the wear and work outcomes, assuming that the speed affects the reduction ratio of the feed.

6.2.3 Summary of the discussion on the relationship between wear and work

The main target of this discussion was to examine whether the observed relationship between the wear and work is consistent and logical. This target was approached in several ways, which all seem to support the conclusion that the measurements are in the expected range, comparable to the other tests methods, and are logically explainable.

7 Conclusions

The aim of this thesis was to examine the effect of varying sliding movement in jaw crusher tests while keeping the compressive movement the same. A new jaw crusher design, called the dual pivoted jaw crusher or DPJC, was needed in order to control the movement of the jaws in the desired manner. The repeatability of the DPJC tests was found satisfactory with the $\beta = 90°$ axle tilt giving the maximum lateral or sliding movement between the jaws even when low amount of rock was crushed. Tests with the $\beta = 0°$ axle tilt with almost pure compression requires larger amount of rock per test to achieve satisfactory repeatability.

The research questions of the thesis were formulated as follows:

1. Are the wear of the jaw plates, the comminution of the rock, and the crushing work related?

2. Do the jaw geometry and the rock properties affect the relationship between wear, comminution, and work?

3. Does the increase in the sliding movement of the rock particles on the jaw plates affect the relative wear resistance of the selected materials?

The results brought forth the following conclusions to the research questions:

1. The amount of work done in a test is a sum of compressive work done to comminute rock, which is mainly related to the reduction ratio of the feed and the product, and work done to slide the rock on the jaw plates, which causes friction, deformation, and wear of the plates. The compressive work also causes small amount of wear by indenting the jaw plates. As the increase of sliding movement was found to linearly increase the wear and work, the minimum energy E_0 required to crush the rock in the test could be obtained. The reduction ratio RR of the rock was found to be important for the actual value of E_0, as well as to the amount of both wear and sliding work.

2. The reduction ratio was influenced by the jaw geometry of the tests, but in general the amount of comminution was found to have a minor effect on wear by proper selection of the geometry of the jaws, which means that the relationship between wear and work is easier to compare. The rock properties affect the amount of both wear and work, but the relationship between wear and work was found to be similar with fairly similar kind of minerals (granite, gneiss, tonalite) but to vary for example with quartzite. The increasing jaw angles causes increased amount of wear and work, which in most cases were found to be linearly related with the selected high manganese steel specimens. The angled Jaw2 specimen in the DPJC equipment, which is comparable to the stationary jaw in a normal jaw crusher, was found to affect the relationship between wear and work, causing higher amount of wear in relation to the work done in the test. This was assumed to be caused by the higher lateral speed between the jaws at the initiation of compression, which in turn was assumed to cause increased amount of sliding wear due to a change in the wear mechanism.

3. The increased sliding movement caused minor variations in the relative wear resistance of the WR-series tool steels, whereas the WI-series was found to have better relative wear resistance when the test was only compressive with $\beta = 0°$ axle tilt. The Jaw1 specimens in the tests with the $\beta = 90°$ axle tilt showed highest wear resistances with all steels relative to the reference steel. The change of the axle tilt from 0° to 90° tripled the Jaw1 wear of the reference, while the increase of wear of the tool steels was minimal.

Compared with the ASTM G81-97 test, the DPJC test seems to produce a differing order of wear resistance for the tested materials, where WR series steels performed better than the WI series steels. Judging from the roughness and wear surface hardness, the DPJC test can produce a similarly rough wear environment as the normal laboratory sized single toggle jaw crusher. The main difference between the tests was the size and material of the feed. The DPJC test gave a reasonable relative wear resistance even for the manganese steel XT710, which means that the DPJC device can work harden also manganese steel specimens.

The analysis of the wear surfaces and wear debris showed that in the tool steels cutting chip formation is a dynamic event and may include localization of deformation into adiabatic shear bands. The increasing lateral speed of the jaws was shown to increase the wear of the test materials and that the increase of the work occurred due to the increase of the lateral force along the steel surface. The wear debris of the softer materials did not show serrated chip formation, indicating that the deeper depth of cut did not lead to shear localization.

In conclusion, the DPJC tests reveal the effect of several test parameters on the resulting wear and work. The test method seems rather simple, but it also shows the complexity of the crushing wear test. The geometry, i.e., the jaw angles and their approach path have a huge impact on the obtained results of the wear test. The basic principle in the designing of the DPJC method and test device was to create a crushing environment, where observations and measurements can be done as early and widely as possible to support the scientific understanding of the wear processes in jaw crushing environments.

Suggestions for the future work

The results of this thesis show that the DPJC test can provide a lot of new information about the crushing environment. However, several parameters were not yet thoroughly examined, and further work is therefore needed to bring out all the possibilities that this testing method has to offer. For example, several other types of minerals not included in this work could be examined to better understand their effect on the wear resistance of the jaw plate materials. Another example is that the jaw angles and the β angle, which were shown to have a significant effect on the wear of the specimens, could in the DPJC tests be adjusted similar to the movement and geometry of the single-toggle jaw crusher to ease the comparison for example with the ASTM G81-97 test. Also a DPJC test series with dissimilar specimens in the same test could further explain the differences between the G81 and DPJC tests.
The design of the equipment proved to be reliable and functional for most parts. However, some modifications could be useful. For example, the feed system turned out to be a bit too narrow to accept feed sizes larger than 12.5 mm, which restricts the use of standard aggregate sizes, e.g., 0 mm - 16 mm as feed. The 25 mm wide jaws of the DPJC works well in the comminution studies with smaller feed sizes, but it would be beneficial if the

modular structure allowed also the use of wider, e.g., 50 mm jaws, which could be used to crush feed with a larger size. This would, however, increase the crushing forces and might require modifications in the semi-open structure of the DPJC, for example use of axles on both sides of the jaw for additional support.

Bibliography

[1] ASTM G81-97a, standard practice for jaw crusher gouging abrasion test. *ASTM International, West Conshohocken, PA, (2013).*, 2013.

[2] K.-H. Zum-Gahr. *Microstructure and wear of materials, Tribology series; 10.* Elsevier, New York, 1987.

[3] K. Viilo. *Crushing and screening handbook 5th edition.* Metso, 2011.

[4] T. Napier-Munn. Preface to 7th edition. In Barry A. Wills and Tim Napier-Munn, editors, *Wills' Mineral Processing Technology (Seventh Edition)*, pages ix –. Butterworth-Heinemann, Oxford, seventh edition edition, 2005.

[5] J. De la Vergne. *Hard Rock Miners's Handbook.* Stantec Consulting Ltd., 5th edition, 2008.

[6] A. Gupta and D.S. Yan. *Mineral Processing Design and Operation.* Elsevier Science, Amsterdam, 2006.

[7] Desmond Tromans. Mineral comminution: Energy efficiency considerations. *Minerals Engineering*, 21(8):613 – 620, 2008.

[8] B.P. Numbi, J. Zhang, and X. Xia. Optimal energy management for a jaw crushing process in deep mines. *Energy*, 68:337–348, 2014.

[9] R.T. Hukki. Proposal for a solomonic settlement between the theories of von rittinger, kick and bond. *Transactions on AIME*, 220:403–408, 1961.

[10] A. Mwanga, P. Lamberg, and J. Rosenkranz. Comminution test method using small drill core samples. *Minerals Engineering*, 72:129–139, 2015.

[11] F.C. Bond. Lab equipment and tests help predict metal consumption in crushing and grinding units. *E &. MJ*, 67:169–176, 1964.

[12] T. Korman, G. Bedekovic, T. Kujundzic, and D. Kuhinek. Impact of physical and mechanical properties of rocks on energy consumption of jaw crusher. *Physicochemical Problems of Mineral Processing*, 51(2):461–475, 2015.

[13] A. L. Tonge, J. Kimberley, and K. T. Ramesh. The mechanism of compressive unloading failure in single crystal quartz and other brittle solids. *International Journal of Solids and Structures*, 49(26):3923 – 3934, 2012.

[14] J. Kimberley, K. T. Ramesh, and O. S. Barnouin. Visualization of the failure of quartz under quasi-static and dynamic compression. *Journal of Geophysical Research: Solid Earth*, 115(B8):n/a–n/a, 2010. B08207.

[15] A. Tosun and G. Konak. Development of a model estimating energy consumption values of primary and secondary crushers. *Arabian Journal of Geosciences*, 8(2):1133–1144, 2015.

[16] G. Unland and Szczelina P. Coarse crushing of brittle rocks by compression. *International Journal of Mineral Processing*, 74, Supplement:S209 – S217, 2004. Special Issue Supplement Comminution 2002.

[17] L.M. Tavares and R.P. King. Single-particle fracture under impact loading. *International Journal of Mineral Processing*, 54(1):1–28, 1998.

[18] L. Workman and J. Eloranta. The effects of blasting on crushing and grinding efficiency and energy consumption. volume I, pages 131–140, 2003.

[19] E.W. Blake. Machine foe, June 15 1858. US Patent 20,542.

[20] M.B. Peterson and W.O. Winer. *Wear Control Handbook.* The American Society of Mechanical Engineers, New York, 1980.

[21] I.R. Sare and A.G. Constantine. Development of methodologies for the evaluation of wear-resistant materials for the mineral industry. *Wear*, 203-204:671–678, 1997.

[22] R. Blickensderfer. Design criteria and correction factors for field wear testing. *Wear*, 122-2:165–182, 1999.

[23] J.H. Hall. Proceedings, american society for testing and materials. *astea*, 28 part II:236–331, 1929.

[24] V.P. Ksenofontov. Russian castings production. *RTCPA*, No. 7:310–312, 1966.

[25] F Borik and D.L. Sponseller. Gouging abrasion test for materials used in ore and rock crushing- 1. *J Mater*, 6(3):576–589, 1971.

[26] F Borik and W.G. Scholz. Gouging abrasion test for materials used in ore and rock crushing- 2. *J Mater*, 6(3):590–605, 1971.

[27] R. Sare and W.B. Hall. The determination of gouging abrasion resistance by jaw crusher tests. *Conf. on Lubrication Friction & Wear in Engineering*, 01(80-12)):1–2, 1980.

[28] I.R. Sare and B.K. Arnold. Gouging abrasion of wear-resistant alloy white cast irons. *Wear*, 131(1):15–37, 1989.

[29] I.R. Sare and A.G. Constantine. Design and analysis of jaw crusher gouging abrasion tests. *Journal of Testing and Evaluation*, 19(2):115–122, 1991.

[30] M. Lindqvist and C.M. Evertsson. Linear wear in jaw crushers. *Minerals Engineering*, 16(1):1–12, 2003.

[31] M. Lindqvist and C.M. Evertsson. Prediction of worn geometry in cone crushers. *Minerals Engineering*, 16(12):1355–1361, 2003.

[32] M. Lindqvist and C.M. Evertsson. Development of wear model for cone crushers. *Wear*, 261(3-4):435–442, 2006.

[33] I. M. Hutchings. *Tribology, Friction and Wear of Engineering Materials.* Edward Arnold, London, 1992.

[34] S. Kivioja, S. Kivivuori, and P. Salonen. *Tribologia, kitka, kuluminen ja voitelu.* Hakapaino, Helsinki, 2004.

[35] European committee for standardization. Geometrical product specifications (GPS) - surface texture: Profile method - terms, definitions and surface texture parameters (ISO 4287:1997(E/F)). , 1997.

[36] J.F. Song and T.V. Vorburger. *Friction, Lubrication, and Wear Technology, Vol 18, ASM Handbook*. Asm International, 1992.

[37] European committee for standardization. Geometrical product specifications (GPS) - surface texture: Areal - part 2: Terms, definitions and surface texture parameters (ISO 25178-2:2012(E)). , 2012.

[38] D. Tabor. The physical meaning of indentation and scratch hardness. *British Journal of Applied Physics*, 7(5):159–166, 1956.

[39] J.A. Greenwood and J.B.P. Williamson. Contact of nominally flat rough surfaces. *Proc. Roy. Soc. Lond.*, A295:300–319, 1966.

[40] F. Bowden, A. Moore, and D. Tabor. The ploughing and adhesion of sliding metals. *J. Appl. Phys.*, 14:80–91, 1943.

[41] A.G. Atkins. Toughness in wear and grinding. *Wear*, 61(1):183–190, 1980.

[42] J.F. Archard. Contact and rubbing of flat surfaces. *Journal of Applied Physics*, 24(8):981–988, 1953.

[43] M. M. Khruschov. Principles of abrasive wear. *Wear*, 28:69–88, 1974.

[44] A. Misra and I. Finnie. Some observations on two-body abrasive wear. *Wear*, 68(1):41–56, 1981.

[45] A.P. Mouritz and I.M. Hutchings. The abrasive wear of steel during rolling-sliding contact with rock counterfaces. *Wear*, 134(1):99–113, 1989.

[46] A. Misra and I. Finnie. A classification of three-body abrasive wear and design of a new tester. *Wear*, 60(1):111–121, 1980.

[47] N. Axn, S. Jacobson, and S. Hogmark. Influence of hardness of the counterbody in three-body abrasive wear - an overlooked hardness effect. *Tribology International*, 27(4):233–241, 1994.

[48] G.H. Yang and W.M. Garrison Jr. A comparison of microstructural effects on two-body and three-body abrasive wear. *Wear*, 129(1):93–103, 1989.

[49] J.D. Gates. Two-body and three-body abrasion: A critical discussion. *Wear*, 214(1):139–146, 1998.

[50] L. Fang, Q. Zhou, and Q. Li. An experimental simulation of cutting wear in three-body abrasion. *Wear*, 219(2):188–194, 1998.

[51] Y. Wang and Z. Wang. Analysis of the influence of plastic indentation on three body abrasive wear of metals. volume 2, pages 619–625, 1987.

[52] J.D. Gates, G.J. Gore, M.J.-P. Hermand, M.J.-P. Guerineau, P.B. Martin, and J. Saad. The meaning of high stress abrasion and its application in white cast irons. *Wear*, 263(1-6 SPEC. ISS.):6–35, 2007.

[53] E. Rabinowicz, L.A. Dunn, and P.G. Russell. A study of abrasive wear under three-body conditions. *Wear*, 4(5):345–371, 1961.

[54] J. Larsen-Badse. Influence of atmospheric humidity on abrasive wear-i. 3-body abrasion. *Wear*, 31:373–379, 1975.

[55] M. A. Moore. A review of two-body abrasive wear. *Wear*, 27:1–17, 1974.

[56] M.S. Bingley and S. Schnee. A study of the mechanisms of abrasive wear for ductile metals under wet and dry three-body conditions. *Wear*, 258(1-4 SPEC. ISS.):50–61, 2005.

[57] B. Bohloli and E. Hoven. A laboratory and full-scale study on the fragmentation behavior of rocks. *Engineering Geology*, 89(1-2):1–8, 2007.

[58] E. Rabinowicz and Mutis A. Effect of abrasive size on wear. *Wear*, 8:381–390, 1965.

[59] J.M. Challen and P.L.B. Oxley. An explanation of the different regimes of friction and wear using asperity deformation models. *Wear*, 53(2):229–243, 1979.

[60] J.M. Challen, P.L.B. Oxley, and E.D. Doyle. The effect of strain hardening on the critical angle for abrasive (chip formation) wear. *Wear*, 88(1):1–12, 1983.

[61] T. R. Bates, K. C. Ludema, and Brainard W. A. A rheological mechanism of penetrative wear. *Wear*, 30:365–375, 1974.

[62] K. Hokkirigawa, K. Kato, and Z.Z. Li. The effect of hardness on the transition of the abrasive wear mechanism of steels. *Wear*, 123(2):241–251, 1988.

[63] H. Kitsunai, K. Kato, K. Hokkirigawa, and H. Inoue. The transitions between microscopic wear modes during repeated sliding friction observed by a scanning electron microscope tribosystem. *Wear*, 135(2):237–249, 1990.

[64] A.A. Torrance. A new approach to the mechanics of abrasion. *Wear*, 67(2):233–257, 1981.

[65] W.M. Garrison Jr. and R.A. Garriga. Ductility and the abrasive wear of an ultrahigh strength steel. *Wear*, 85(3):347–360, 1983.

[66] K.H. Zum Gahr. Formation of wear debris by the abrasion of ductile metals. *Wear*, 74(2):353–373, 1981.

[67] K.H. Zum Gahr. Modelling of two-body abrasive wear. *Wear*, 124(1):87–103, 1988.

[68] N.P. Suh. An overview of the delamination theory of wear. *Wear*, 44(1):1–16, 1977.

[69] H.R. Shetty, T.H. Kosel, and N.F. Fiore. A study of abrasive wear mechanisms using diamond and alumina scratch tests. *Wear*, 80(3 , Sep. 1982, p.347-476.), 1982.

[70] Y. Xie and J.A. Williams. The generation of worn surfaces by the repeated interaction of parallel grooves. *Wear*, 162-164(PART B):864–872, 1993.

[71] X. Yin and K. Komvopoulos. A slip-line plasticity analysis of abrasive wear of a smooth and soft surface sliding against a rough (fractal) and hard surface. *International Journal of Solids and Structures*, 49(1):121–131, 2012.

[72] A. Misra and I. Finnie. On the size effect in abrasive and erosive wear. *Wear*, 65(3):359–373, 1981.

[73] V. Jardret, H. Zahouani, J.L. Loubet, and T.G. Mathia. Understanding and quantification of elastic and plastic deformation during a scratch test. *Wear*, 218(1):8–14, 1998.

[74] A.G. Atkins and J.H. Liu. Toughness and the transition between cutting and rubbing in abrasive contacts. *Wear*, 262(1-2):146–159, 2007.

[75] R. C. D. Richardson. The maximum wear of strained surfaces and the abrasive wear of metals and alloys. *Wear*, 10:353–382, 1967.

[76] R. C. D. Richardson. The wear of metals by hard abrasives. *Wear*, 10:291–309, 1967.

[77] R. C. D. Richardson. The wear of metals by relatively soft abrasives. *Wear*, 11:245–275, 1968.

[78] A.A. Torrance. Correlation of abrasive wear tests. *Wear*, 63(2):359–370, 1980.

[79] K.-H.Z. Gahr. Wear by hard particles. *Tribology International*, 31(10):587–596, 1998.

[80] E. Hornbogen. The role of fracture toughness in the wear of metals. *Wear*, 33(2):251–259, 1975.

[81] M. A. Moore. Preliminary investigation of frictional heating during abrasive wear. *Wear*, 17:51–58, 1971.

[82] T. S. Eyre and A. Baxter. The formation of white layers at rubbing surfaces. *Tribology*, 5(6):256–261, 1972.

[83] Y.Y. Yang, H.S. Fang, and W.G. Huang. A study on wear resistance of the white layer. *Tribology International*, 29(5):425–428, 1996.

[84] Y. Xu, L. Fang, Q. Cen, and J. Zhu. Nano structure and transformation mechanism of white layer for AISI1045 steel during impact wear. *Wear*, 258(1-4 SPEC. ISS.):537–544, 2005.

[85] S.B. Hosseini, U. Klement, Y. Yao, and K. Ryttberg. Formation mechanisms of white layers induced by hard turning of {AISI} 52100 steel. *Acta Materialia*, 89:258 – 267, 2015.

[86] B. Dodd and Y. Bai. 1 - introduction. In Bradley Bai and Yilong Dodd, editors, *Adiabatic Shear Localization (Second Edition)*, pages 1 – 20. Elsevier, Oxford, second edition, 2012.

[87] S.V. Kailas and S.K. Biswas. Strain rate response and its effect in plane strain abrasion of metals by a wedge. *Wear*, 184(1):23–32, 1995.

[88] O. Vingsbo and S. Hogmark. Single-pass pendulum grooving - a technique for abrasive testing. *Wear*, 100(1-3):489–502, 1984.

[89] S. Söderberg, U. Bryggman, and A. Canales. Influence of precipitation and solution strengthening on abrasive wear resistance. *Wear*, 105(1):1–17, 1985.

[90] G. Sundararajan. A new model for two-body abrasive wear based on the localization of plastic deformation. *Wear*, 117(1):1–35, 1987.

[91] T. H. Courtney. *Mechanical behavior of materials, Second edition.* MacGraw-Hill Book Co, Singapore, 2000.

[92] M. A. Meyers. *Dynamic behavior of materials.* John Wiley & Sons Inc., 605 Third Avenue, New York, 1994.

[93] X. Xu, S. van der Zwaag, and W. Xu. The scratch and abrasive wear behaviour of a tempered martensitic construction steel and its dual phase variants. *Wear*, 358-359:80–88, 2016.

[94] X. Xu, F.H. Ederveen, S. van der Zwaag, and W. Xu. Correlating the abrasion resistance of low alloy steels to the standard mechanical properties: A statistical analysis over a larger data set. *Wear*, 368-369:92–100, 2016.

[95] W.M. Garrison Jr. Khruschov's rule and the abrasive wear resistance of multiphase solids. *Wear*, 82(2):213–220, 1982.

[96] W. Simm and S. Freti. Abrasive wear of multiphase materials. *Wear*, 129(1):105–121, 1989.

[97] R. Colao and R. Vilar. Abrasive wear of metallic matrix reinforced materials. *Wear*, 255(1-6):643–650, 2003.

[98] R. Colao and R. Vilar. A model for the abrasive wear of metallic matrix particle-reinforced materials. *Wear*, 254(7-8):625–634, 2003.

[99] K.S. Al-Rubaie. Equivalent hardness concept and two-body abrasion of iron-base alloys. *Wear*, 243(1-2):92–100, 2000.

[100] E. Albertin and A. Sinatora. Effect of carbide fraction and matrix microstructure on the wear of cast iron balls tested in a laboratory ball mill. *Wear*, 250-251(PART 1):492–501, 2001.

[101] J. Hu, D.Y. Li, and R. Llewellyn. Computational investigation of microstructural effects on abrasive wear of composite materials. *Wear*, 259(1-6):6–17, 2005.

[102] R. Llewellyn. Gouging abrasion resistance of materials for oil sand service. *Austrib, Brisbane*, 2006.

[103] X. Liujie, X. Jiandong, W. Shizhong, Z. Yongzhen, and L. Rui. Investigation on wear behaviors of high-vanadium high-speed steel compared with high-chromium cast iron under rolling contact condition. *Materials Science and Engineering A*, 434(1-2):63–70, 2006.

[104] S. Wei, J. Zhu, and L. Xu. Effects of vanadium and carbon on microstructures and abrasive wear resistance of high speed steel. *Tribology International*, 39(7):641–648, 2006.

[105] A.A. Torrance. An explanation of the hardness differential needed for abrasion. *Wear*, 68(2):263–266, 1981.

[106] B.W.E. Avient, J. Goddard, and H. Wilman. An experimental study of friction and wear during abrasion of metals. *Proc. R. Soc. Lond. A.*, 258(1293):159–180, 1960.

[107] M. Woldman, E. Van Der Heide, T. Tinga, and M.A. Masen. The influence of abrasive body dimensions on single asperity wear. *Wear*, 301(1-2):76–81, 2013.

[108] G. K. Nathan and W. J. D. Jones. The empirical relationship between abrasive wear and the applied conditions. *Wear*, 9:300–309, 1966.

[109] D.A. Kelly and I.M. Hutchings. A new method for measurement of particle abrasivity. *Wear*, 250-251(PART 1):76–80, 2001.

[110] M.A. Verspui, P. Van Der Velden, G. De With, and P.J. Slikkerveer. Angularity determination of abrasive powders. *Wear*, 199(1):122–126, 1996.

[111] A.-L. Persson. Image analysis of shape and size of fine aggregates. *Engineering Geology*, 50(1-2):177–186, 1998.

[112] M.G. Hamblin and G.W. Stachowiak. A multi-scale measure of particle abrasivity, and its relation to two-body abrasive wear. *Wear*, 190(2):190–196, 1995.

[113] G.W. Stachowiak. Numerical characterization of wear particles morphology and angularity of particles and surfaces. *Tribology International*, 31(1-3):139–157, 1998.

[114] G.B. Stachowiak and G.W. Stachowiak. The effects of particle characteristics on three-body abrasive wear. *Wear*, 249(3-4):201–207, 2001.

[115] W.D. Jr. Callister. *Materials Science and Engineering, An Introduction, 5th Edition.* John Wiley & Sons Inc., 605 Third Avenue, New York, 2000.

[116] M. Yao and N.W. Page. Influence of comminution products on abrasive wear during high pressure crushing. *Wear*, 242(1-2):105–113, 2000.

[117] V. Heino, K. Valtonen, P. Kivikytö-Reponen, P. Siitonen, and V.-T. Kuokkala. Characterization of the effects of embedded quartz layer on wear rates in abrasive wear. *Wear*, 308(1-2):174–179, 2013.

[118] A.L. Yurkov, V.N. Skvortsov, I.A. Buyanovsky, and R.M. Matvievsky. Sliding friction of diamond on steel, sapphire, alumina and fused silica with and without lubricants. *Journal of Materials Science Letters*, 16(16):1370–1374, 1997.

[119] A. Misra and I. Finnie. An experimental study of three-body abrasive wear. *Wear*, 85(1):57–68, 1983.

[120] G. Pintaude, D.K. Tanaka, and A. Sinatora. The effects of abrasive particle size on the sliding friction coefficient of steel using a spiral pin-on-disk apparatus. *Wear*, 255(1-6):55–59, 2003.

[121] J.P. Sinha, B. Sahay, and G.K. Lal. Forces produced during cutting with single abrasive grains. *Wear*, 66(2):133–144, 1981.

[122] J. Goddard and H. Wilman. A theory of friction and wear during the abrasion of metals. *Wear*, 5(2):114–135, 1962.

[123] T.O. Mulhearn and L.E. Samuels. The abrasion of metals: A model of the process. *Wear*, 5(6):478–498, 1962.

[124] Y. Xie and J.A. Williams. The prediction of friction and wear when a soft surface slides against a harder rough surface. *Wear*, 196(1-2):21–34, 1996.

[125] A.A. Torrance. Modelling abrasive wear. *Wear*, 258(1-4 SPEC. ISS.):281–293, 2005.

[126] P. Kallas. Indentation energy and abrasive wear of metals. *Wear*, 198(1-2):77–85, 1996.

[127] G. Beckmann. A theory of abrasive wear based on shear effects in metal surfaces. *Wear*, 59(2):421–432, 1980.

[128] J. Larsen-Badse. Abrasion resistance of some s.a.p. -type alloys at room temperature. *Wear*, 12:357–368, 1968.

[129] J. Larsen-Badse and K. G. Mathew. Influence of structure on the abrasion resistance of a 1040 steel. *Wear*, 14:199–206, 1969.

[130] S. Malkin and N. Joseph. Minimum energy in abrasive processes. *Wear*, 32:15–23, 1975.

[131] G.J. Gore and J.D. Gates. Effect of hardness on three very different forms of wear. *Wear*, 203-204:544–563, 1997.

[132] N.B. Dube and I.M. Hutchings. Influence of particle fracture in the high-stress and low-stress abrasive wear of steel. *Wear*, 233-235:246–256, 1999.

[133] S. Ala-Kleme, P. Kivikytö-Reponen, J. Liimatainen, J. Hellman, and S.-P. Hannula. Abrasive wear properties of tool steel matrix composites in rubber wheel abrasion test and laboratory cone crusher experiments. *Wear*, 263(1-6 SPEC. ISS.):180–187, 2007.

[134] J.A. Hawk, R.D. Wilson, J.H. Tylczak, and Ö.N. Doğan. Laboratory abrasive wear tests: Investigation of test methods and alloy correlation. *Wear*, 225-229(PART II):1031–1042, 1999.

[135] J.H. Tylczak, J.A. Hawk, and R.D. Wilson. A comparison of laboratory abrasion and field wear results. *Wear*, 225-229(PART II):1059–1069, 1999.

[136] G. A. Roberts, J. C. Hamaker, and A. R. Johnson. *Tool steels, Third Edition*. ASME, Metals Park, Ohio, American society for metals, 1962.

[137] J. Hautalahti. *Laboratoriomenetelmät kiven murskattavuuden arvioimiseksi*. Tampere University of Technology, 1996.

[138] A. Refahi, J. Aghazadeh Mohandesi, and B. Rezai. Discrete element modeling for predicting breakage behavior and fracture energy of a single particle in a jaw crusher. *International Journal of Mineral Processing*, 94(12):83 – 91, 2010.

[139] J. Terva, T. Teeri, V.-T. Kuokkala, P. Siitonen, and J. Liimatainen. Abrasive wear of steel against gravel with different rocksteel combinations. *Wear*, 267(11):1821 – 1831, 2009. {ICAP} 2008.

[140] T. Atkins. Chapter 4 - types of chip: Load fluctuations, scaling and deformation transitions. In Tony Atkins, editor, *The Science and Engineering of Cutting*, pages 75 – 109. Butterworth-Heinemann, Oxford, 2009.

[141] H.S. Avery. The measurement of wear resistance. *Wear*, 4(6):427–449, 1961.

[142] R. C. Tucker and A. E. Miller. *Low stress abrasive and adhesive wear testing, Selection and use of wear tests for metals.* ASTM STP 615, R. G. Bayer, ed., American society for testing and materials, 1976, pp. 68-90.

[143] F. Borik. *Testing for Abrasive Wear, Selection and use of wear tests for metals.* ASTM STP 615, R. G. Bayer, ed., American society for testing and materials, 1976, pp. 30-44.

[144] D. Legendre and R. Zevenhoven. Assessing the energy efficiency of a jaw crusher. *Energy*, 74:119 – 130, 2014.

[145] S. Morrell. Predicting the overall specific energy requirement of crushing, high pressure grinding roll and tumbling mill circuits. *Minerals Engineering*, 22(6):544–549, 2009.

[146] P.W. Cleary and M.D. Sinnott. Simulation of particle flows and breakage in crushers using dem: Part 1 - compression crushers. *Minerals Engineering*, 74:178–197, 2015.

[147] R. Veinthal M. Saarna, P. Kulu and R. Tarbe. Study of surface fatigue of wear resistant powder metallurgical materials. *Proc. Estonian Acad. Sci. Eng.*, 12(4):377 – 387, 206.

[148] N. Diaz, E. Redelsheimer, and D. Dornfeld. *Energy Consumption Characterization and Reduction Strategies for Milling Machine Tool Use*, pages 263–267. Springer Berlin Heidelberg, Berlin, Heidelberg, 2011.

Tampereen teknillinen yliopisto
PL 527
33101 Tampere

Tampere University of Technology
P.O.B. 527
FI-33101 Tampere, Finland

ISBN 978-952-15-3910-7
ISSN 1459-2045